A study of the Film Growth Environment in Pulsed Laser Deposition of Gallium Nitride

Donagh O'Mahony

A thesis submitted for the degree of
Doctor of Philosophy
University of Dublin

Physics Department

Trinity College

August 2004

Declaration

This thesis has not been submitted as an exercise for a degree in any other university.

This thesis is entirely my own work, except for the advice and assistance mentioned in the acknowledgements.

I agree to allow the library of Trinity College Dublin copy or lend a section or this entire thesis on request.

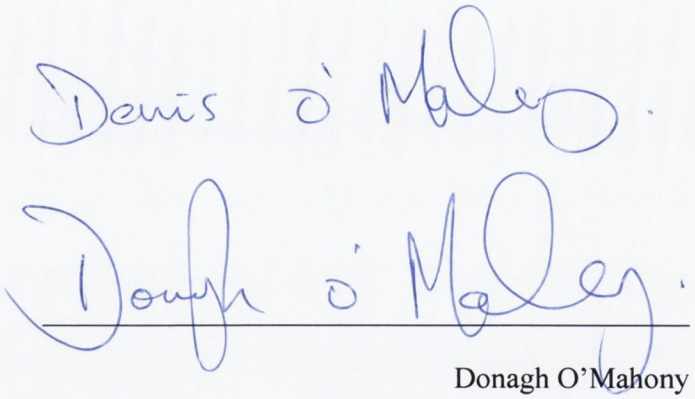

Donagh O'Mahony

August 2004.

Summary

This thesis describes a study of the deposition requirements for growth of stoichiometric GaN thin films using pulsed laser deposition. Growth has been carried out using either ceramic GaN or metal (solid and liquid) Ga targets in molecular nitrogen and nitrogen plasma discharge background gases. The potential advantages of using a liquid target for film growth were considered, as were the problems associated with incongruent material transfer from target to film in ns ablation of GaN. The effect of laser fluence and background gas pressure on the stoichiometry of the films was monitored using an optical reflectometry technique and a model to extract the free gallium fraction in the films. The expansion dynamics of the laser-produced plasma were studied using Langmuir ion probes, in the time-of-flight mode, which allowed the ion energy distribution in an inertial (high vacuum) expansion to be measured. This technique was also used to map the ion energy reduction with increasing distance from the target in a relatively high (~ 0.1 mbar) N_2 background gas pressure.

The suitability of three types of nitrogen plasma discharge for GaN thin film growth was also investigated. It was found that stoichiometric GaN film growth with the Ga target was possible at lower pressures than those used with molecular nitrogen when a pulsed discharge, synchronised with the arrival of the plume to the substrate, was used.

Finally, the possibility of using pulsed laser deposition for the growth of a novel diluted magnetic semiconductor, GaMnN, was investigated. This study identified the substrate temperature requirements for single phase growth and the solubility limits for Mn incorporation into the GaN lattice. The origin of room-temperature magnetism observed in some of these films and the correspondingly low moment per Mn atom is considered.

Acknowledgements

I would like to acknowledge the following people for their effort and friendship over the course of this work:

To my parents, for selflessly providing me with every opportunity in life, and to Barry, Aine and Eoghan for always staying in touch and rambling in to check on me anytime they could. Thanks also to Ann for keeping me on my toes with emails and pc queries (and maybe the odd prayer to St. Jude) from all time zones.

The staff of the physics department deserves particular mention for always being on hand to provide administrative and technical help (especially for rescuing pension-age lasers or turbo pumps), or in the case of John Kelly, a reminder of where I came from. Thanks to my supervisor, James Lunney, for giving me the opportunity to work at the department, and for his willingness to advice on many aspects of the project work.

A number of researchers in the department have helped me from time to time with sample preparation or characterisation, but Group D deserve special mention for always having a welcoming smile even though they must have known that we (and most of the department) were looking for their time or equipment. Thanks to those wise old men of ellipsometry, Lee and Chris, for carrying out measurements on short notice, and to Kevin Ryan for providing the microscope camera on equally short call. Thanks also to Enda McGlynn's group at the National Centre for Plasma Science and Technology, DCU for PL measurements and advice over the course of the work.

I've been lucky to have worked with some top notch people over the years in group L who have helped me find my feet in the world of vacuum and laser techniques. But in particular, to lab-mates Doggett and de Posada, *Ní bheidh bhur leitheid arís.*

Many people have made the years in Dublin fly past, and I would like to say thanks to all the lads (and more recently the lassies) of Jervis, the Manor and the Mews who I've crossed paths (and camáns) with in this time.

Finally, thanks Ca for keeping me smiling and focussed all these years. I would never have learned as much about life without you.

Table of contents

Glossary

Quantity	Symbol	Conventional units
Temperature	T	°C
Energy	E	Joule
Area	A	cm^2/mm^2
Fluence	F	J cm^{-2}
Background gas pressure	p	mbar
Gas density	n_g	cm^{-3}
Particle number	N	-
Time of flight	t_{TOF}	µs
Velocity	v	m s^{-1}
Incident angle	θ_i	degree
Wavelength	λ	nm
Complex refractive index	$\hat{n} = n - ik$	-
Extinction coefficient	k	-
Optical absorption depth	$d_{opt} = \lambda / 4\pi k$	nm
s-polarised reflectivity	R_s	-
Electron charge	e	C
Ion / deposition flux	j_{ion} / j_{dep}	cm^{-2} s^{-1}
Time-integrated flux	J	cm^{-2}
Film growth rate	δ_{Film}	nm/shot

1. Material properties

The following sections outline some of the properties of Ga and GaN which are relevant to target preparation and film growth. Some properties of nitrogen are also discussed, particularly its stability in the ground molecular state. For convenience, the properties of Ga and GaN are gathered under two headings; physical properties and optical properties, though the former heading is somewhat ambiguous since a range or properties will be referred to such as chemical and electrical quantities. Some of the quantities which will be referred to frequently through the thesis are listed in table 1.1.

1.1 Properties of Ga, GaN and N_2

1.1.1 Physical properties of Gallium

Gallium is a hugely important source material for the semiconductor industry, with GaAs and, more recently, GaN-based devices accounting for 98% of all gallium requirements in the last year[1]. It is one of only four elements which is liquid near room temperature, and has one of the longest liquid ranges amongst the elements (see table 1.1). Solid gallium is orthorhombic, and its rigid directional bonds lead to a rather inefficient packing structure which, unlike most metals, results in an increase in density on melting [Wittenberg and DeWitt, 1972]. Gallium is in fact classed as a semimetal, and has a comparatively low electrical (7.35×106 S m-1 [Lide, 1998]) and thermal conductivity (see figure 1.1), when compared with a good conductor like copper or aluminium (the electrical conductivity of Al and Cu is about an order of magnitude greater than that of Ga). Gallium has a number of other properties [Iida and Gutherie, 1988a] which have particular relevance to its preparation as a target in PLD of GaN. Liquid metals tend to have considerable surface curvature which makes the laser spot size and laser fluence difficult to determine accurately. While the surface tension can be reduced somewhat (~ 0.1 mN m^{-1} K^{-1} for Ga)

[1] US geological survey (http://minerals.usgs.gov/minerals/pubs/commodity/gallium/).

by heating the metal, the problem of a curved target surface is probably best tackled by use of a shallow, large diameter target holder.

	GaN	Ga	Units
Structural properties			
Crystal structure	Hexagonal/ Cubic	Orthorhombic	
[x] Lattice constants (a_0, b_0, c_0)	3.19, 3.19, 5.19/ 4.52	4.52, 4.49, 7.63 [e]	Å
Density	6.15 [f]	5.91 (6.1) [i]	g cm^{-3}
Thermal properties			
Melting point	~ 2800 [a]	303 [a]	K
Boiling point	_	2500 [b]	K
Heat capacity	[a] 41	26 [i]	J K^{-1} mol^{-1}
Thermal conductivity	[a] 1.3, 0.3*	0.436 (0.278) [c]	W cm^{-1} K^{-1}
Heat diffusion depth	500	590	nm
Optical properties			
Bandgap	[f] 3.45 (300 K)	--	eV
n, k (λ=248 nm)	[g] 2.55, [j] 0.394	(0.25, 2.7) [e]	
n, k (λ=635 nm)	[g] 2.35, [h] 0.0005	(1.4, 6.9) [e]	
Absorption depth (λ= 248 nm)	50	7	nm

Table 1.1 Some properties of GaN and Ga relevant to the PLD process. The values tabulated were measured using single crystal GaN thin films and bulk Ga, except for the values in parentheses, which were obtained using liquid gallium. *The conductivity estimate for ceramic targets was made noting the result in Krukowski et al. [Krukowski, 1998]. Where applicable, the values are room temperature quantities. *Sources:* [a] [Edgar, 1994]; [b] [Geiger et al., 1987]; [c] [Jiemin and Lamvik, 1998]; [d] [Kofman et al., 1977]; [e] [Schulz, 1955]; [f] [Chin et al., 1994]; [g] [Yu et al., 1997]; [h] [Ambacher et al., 1996]; [i] [Iida and Gutherie, 1988a] (300 K -500 K); [j] [Muth et al., 1997]; [x] [ICCD].

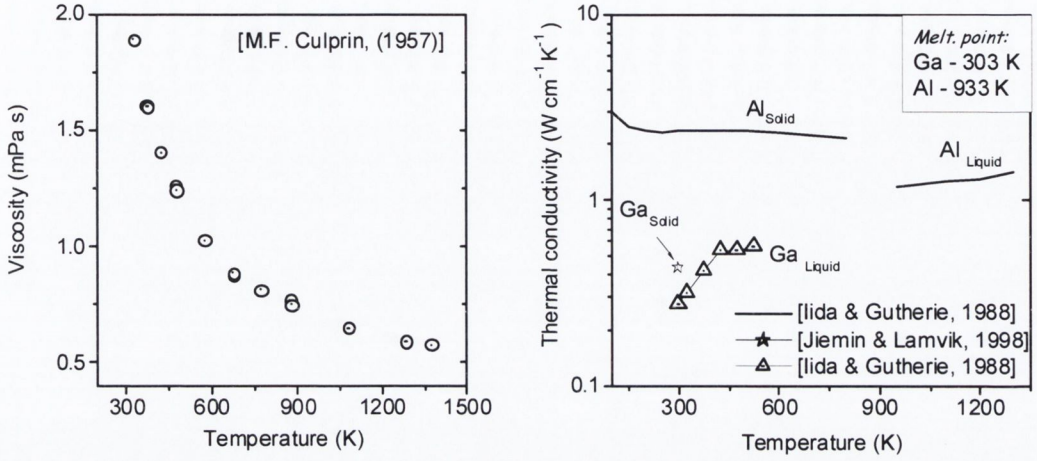

Fig. 1.1 Viscosity (left) and thermal conductivity (right) of gallium as a function of temperature. For comparison, the thermal conductivity of aluminium is also included. A detailed overview of the properties of liquid gallium is given in [Iida and Gutherie, 1988a]

Gallium will corrode aluminium [Bhadeshia, 2003] and the use of aluminium containers or target holders is best avoided. Of particular relevance to film growth purity is the fact that group III metals tend to oxidise quite easily, and an exposure of ~ 10-100 Langmuir (1Langmuir = 10^{-4} Pa s = 10^{-6} mbar s) of air is sufficient to form an oxide layer of a few nm thickness [Regan et al., 1997]. Finally, liquid gallium has a tendency to supercool, and, since its viscosity rises sharply below the melting temperature [Culprin, 1957], a subsequent rapid solidification will tend to freeze-in any surface structure. Care must therefore be taken to cool targets slowly to obtain smooth, flat surfaces [Kofman et al., 1977].

1.1.2 Optical properties of Gallium

Solid gallium is strongly anisotropic; therefore its reflectivity depends on the direction of the incident polarization vector relative to the crystal axes. At normal incidence, the reflectivity varies from 50%-80% over the visible range. On melting, the reflectivity of gallium increases significantly, remaining fairly constant at ~ 90% in the visible range (see figure 1.2b).

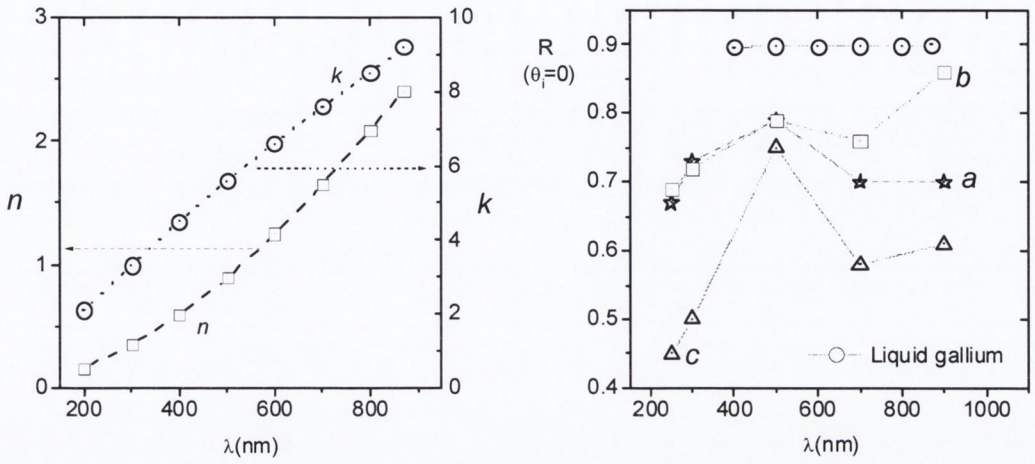

Fig. 1.2 (a) Optical constants for liquid gallium [Schulz, 1955] (left) . The data at λ<400 nm was determined using the Drude free electron model. (b) The normal incidence reflectance for solid gallium [Kofman et al., 1977] (right). The labels *a, b* and *c* correspond to the incident light being polarised parallel to the (100), (010) and (001) axes of the crystal, respectively. For curves *a* and *b*, the light was incident on the (001) surface, while curve *c* was taken with the beam incident on the (010) surface. The normal incidence reflectance for liquid gallium is also included for comparison (circles).

The optical properties of liquid gallium at 248 nm have not been measured experimentally, though the *n* and *k* values for liquid gallium in the (200 – 400) nm wavelength range have been predicted [Schulz, 1955], using the Drude free electron model [2]. Since this data compares quite well to experimentally determined values in the visible and near IR range (400 – 1000 nm), it was assumed that the model was suitable for obtaining values of *n* and *k* at λ = 248 nm. The optical constants[3] for liquid and solid gallium over the visible wavelength range are presented in figures 1.2(a) and 1.2 (b).

---

[2] For an overview of the Drude free-electron theory of metals, see for example Born and Wolf's "Principles of Optics", section 14.3, Born, M. and E. Wolf, *Principles of Optics,* Cambridge University Press, Cambridge, 1999.

[3] Metals with high reflectivity in the UV often satisfy the condition that $n\left(=c/v\right)<1$, which corresponds to a speed greater than *c*, the speed of light in vacuum. In this relation *v* is the phase velocity which is the speed at which cophasal surfaces of a wavefront advance. Since it is not possible to measure the speed of all points on the wavefront simultaneously, this phase velocity is not physically significant and the theory of relativity is not violated (for a rigorous analysis, see [Born and Wolf, 1999], section 1.3.3).

These values have been extrapolated from the data of Schulz [Schulz, 1955] and Kofman [Kofman et al., 1977], respectively.

1.1.3 Physical properties of GaN

GaN is of interest for a range of applications, primarily because of its wide direct bandgap, but also because it exhibits high mechanical strength and stability in demanding chemical and electronic environments. The nitride bond is comparatively strong with a bond energy of 2.24 eV per bond for GaN compared to 1.63 eV per bond in GaAs [Harrison, 1989]. Chemically, it is a very stable compound and can only be wet-etched with aggressive agents such as hot NaOH or H_2SO_4 [Strite and Morkoc, 1992]. The group III nitrides are characterised by high melting temperatures (> 2000 K) and require very high nitrogen pressures (> kbar) near their melting temperatures to prevent decomposition and promote crystal formation [Porowski and Grzegory, 1997]. This requirement renders standard crystallization techniques, such as Czochralski method, impractical for GaN growth. GaN normally crystallizes in the hexagonal wurtzite structure, however the cubic zinc-blende phase can be obtained by controlled film growth on cubic substrates [Wu et al., 2001] (the wurtzite and zincblende structures are illustrated in appendix A). GaN is classified as adamantine (or diamond-like) since it has a tetrahedral bonding co-ordination which, as in diamond, results in excellent hardness and high thermal conductivities of ≥ 1 W cm^{-1} K^{-1} [Slack, 1973]. The thermal expansion coefficient for GaN differs considerably from sapphire which is the most commonly used substrate in GaN thin film growth (see chapter 3, table 3.1).

1.1.4 Optical properties of GaN

In comparison with Si or GaAs, the optical properties of GaN have received little attention, and there is some variation between reports [Ambacher et al., 1996; Yu et al., 1997]. The data of Yu et al. [Yu et al., 1997], as illustrated in figure 1.3a, has been used in this thesis. Dingle et al. [Dingle et al., 1971] have shown that there is a significant degree of optical anisotropy in GaN crystals, particularly at shorter wavelengths ($\leq$350 nm), while Ejder [Ejder, 1971] has measured the temperature dependence of the refractive index to be $\sim 2\times10^{-5}$ K^{-1} near room temperature.

A number of groups have measured the absorption coefficient[4] of GaN single crystals [Dingle et al., 1971; Ambacher et al., 1996; Muth et al., 1997], which increases with carrier concentration. This is particularly noticeable below the bandgap i.e. at longer wavelengths, as illustrated in figure 1.3b [Ambacher et al., 1996], where the data was collected using samples of varying electron concentration.

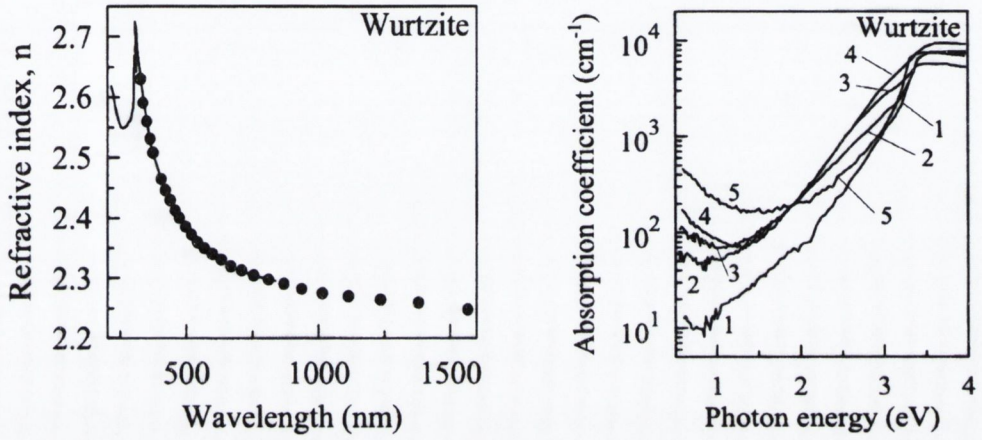

Fig. 1.3 Wavelength (photon energy) variation of (a) refractive index [Yu et al., 1997] and (b) absorption coefficient for various doping concentrations [Ambacher et al., 1996] of GaN single crystal on sapphire (curve labels: [1] 2×10^{16} cm^{-3}, [2] 2.8×10^{17} cm^{-3}, [3] 5×10^{17} cm^{-3}, [4] 2.3×10^{18} cm^{-3}, [5] 2×10^{19} cm^{-3}). The measurements were carried out at room temperature.

It is important to appreciate that the properties of polycrystalline nitride powder pellets used as laser ablation targets in PLD will differ considerably from those of single crystals. Nitride powders normally have a significant fraction (≥0.01 %) of impurities such as oxygen and silicon [Slack, 1973; Slack and McNelly, 1976]. Depending on the method of preparation, pressed powder pellets are also likely to have a lower density and significant void fraction compared with a single crystal. These factors tend to reduce both the mechanical strength and thermal conductivity of the material [Slack, 1973]. Accordingly, the conductivity of the GaN ceramic targets used in this work was assumed to be a factor of 4 less than the single crystal value, noting the result in Krukowski et al. [Krukowski et al., 1998] (see table 1.1). In addition, the surface roughness of polycrystalline targets is considerably greater than single crystals, which reduces its

[4] See appendix E for a overview of the relationships between refractive index and absorption coefficient

reflectivity. Furthermore, a high density of sub-bandedge defect states tends to broaden the optical absorption energy range of the powders compared to single crystals [Cazzanelli et al., 1998]. As a result, the reflectivity of the ceramic targets is likely to be considerably less than that of a single crystal.

1.1.5 Properties of nitrogen

Despite being the dominant constituent in the earth's atmosphere (at ~ 78%), the abundance of nitrides in the earth's crust is extremely low at less that 0.01 % [Battino, 1982]. This is due, primarily, to the fact that the most abundant and stable form of nitrogen, the N_2 molecule, is quite stable with bond energy of 9.8 eV (945 kJ mol^{-1}), which is almost twice the strength of the bond in O_2 (498 kJ mol-1) and 2.5 times greater than the other group V gas As_2 (382 kJ mol^{-1}) [Lide, 1998]. The cross-sectional area of an N_2 molecule is of particular relevance to plume-gas interactions in PLD using a background gas. The N-N bond length is quoted as being 1.098 Å [Lide, 1998], thus the cross-sectional area projected by an N_2 molecule is of the order of 10^{-16} cm^{-2}. It is worth noting that at high pressures (> kbar), N_2 behaves as non-ideally in the sense that the experimentally measured pressures do not vary exponentially with temperature. [Karpinski and Porowski, 1984]. Many nitride film growth systems employ active (see footnote # 2, this chapter) nitrogen sources to promote nitride formation. While 9.8 eV is required to dissociate the N_2 molecule, there are a number of excited molecular nitrogen states at lower energy (see figure 1.4). These levels can provide sufficient energy to overcome the nitride formation barrier in GaN growth, and is a point which is discussed further in section 1.3.

Finally, a quantity which is of considerable importance in film growth applications is the rate at which N_2 molecules interact with the surface of the substrate. The Hertz equation relates the flux (particles per second) per unit area with the pressure (p) and temperature (T) of an ideal gas:

$$j_{Hertz}(T) = \frac{p(T)}{\sqrt{2\pi m_{N_2} k_B T}} \qquad \text{(eq.1.1)}$$

Other than p and T, which are related through the ideal gas equation, this expression depends only on the mass of the N_2 molecule, m_{N_2} which is 28 a.m.u. (k_B is Boltzmann's constant).

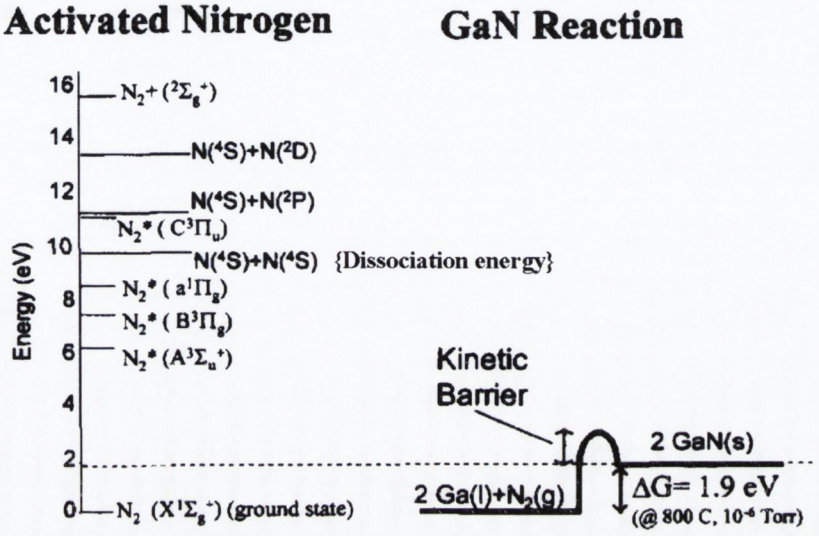

Fig. 1.4 Energy level diagram for active nitrogen. Also included is the Gibbs free energy of formation (ΔG) for two GaN molecules at 800 °C and 1.33×10^{-6} mbar [Newman, 1997].

1.2 High temperature behaviour

Since PLD involves intense heating of the surface of the target material, and in the case of GaN growth, the use of substrate temperatures in excess of 1000 K, an understanding of the behaviour of Ga and GaN at high temperature is desirable. Of particular relevance to PLD is the vapour pressure and evaporation rate, both at the target and film surfaces, which can be used to estimate the plume mass and in the case of film growth, the deposition flux requirements in order to achieve reasonable growth rates. Some of the important thermodynamic quantities introduced in this section are defined in appendix B.

1.2.1 Vapour pressure and evaporation rate

Evaporation from the surface of a liquid or solid[5] in equilibrium with a vapour is most generally described by substituting for the equilibrium rate constant K_a in the standard rate equation (see, for example, [Warn, 1985]):

$$\Delta G^0 = -RT_s \ln K_a \qquad \text{(eq. 1.2)}$$

Here, ΔG^0 is the standard Gibb's free energy of reaction, while R is the universal gas constant (T is absolute temperature). The reaction stoichiometry determines the equilibrium rate constant, K_a, which for a reaction of the form $aA+bB \rightarrow cC+dD$, can be expressed in terms of the molar concentrations (square brackets) as:

$$K_a = \frac{[C]^c[D]^d}{[A]^a[B]^b} \qquad \text{(eq.1.3)}$$

For an ideal gas, K_a can be expressed in terms of the partial pressures of the various evaporating species, with liquids or solids taking a value of unity if the pressures are expressed in bar. In the simple case where a solid or liquid evaporates as single atoms or molecules (as is the case for most metals), the vapour pressure above a surface at temperature T_s is more commonly expressed in terms of the latent heat of evaporation per particle, L_v, in the form of the Clausius-Clapeyron equation:

$$p/p_0 = \exp\left[\frac{L_v}{k_B}\left(\frac{1}{T_0} - \frac{1}{T_s}\right)\right] \qquad \text{(eq.1.4)}$$

Here, p_0 is the equilibrium vapour pressure at a specific temperature T_0, usually taken as the boiling point. For a compound such as GaN, which evaporates according to the equation $GaN \leftrightarrow Ga + \frac{1}{2}N$, the total vapour pressure is likely to be due to the partial

[5] The process whereby a solid vaporises without melting is known as sublimation. For convenience, the term "evaporation" is used to describe the evolution of a vapour above a liquid or solid.

pressures of the various evaporating species, in which case the standard rate equation[6] form must be maintained:

$$\Delta G^0 = -RT_s \ln\left[\frac{p_{Ga} p_{N_2}^{1/2}}{p_{GaN}}\right] \qquad \text{(eq.1.5)}$$

Once the vapour pressure is known, the evaporation rate per unit area (usually expressed in $cm^{-2}\ s^{-1}$) can be determined using the Hertz-Langmuir-Knudsen equation:

$$j_{evap}(T_s) = \alpha \times j_{Hertz}(T) \qquad \text{(eq.1.6)}$$

The evaporation coefficient (ratio of the measured evaporation flux and the thermodynamically predicted flux), α, accounts for processes, such as strong surface bonding, which limit the evaporation rate [Averyanova et al., 1997] (conversely, $\alpha > 1$ if polyatomic evaporation occurs).

1.2.2 Evaporation of Gallium

Gallium is reported to have a considerable fraction of dimers (diatomic molecules) in its vapour, particularly as the temperature is increased above 1000 °C, which introduces a significant degree of uncertainty into evaporation rate calculations [DeMaria, 1970]. It has been suggested that the evaporation coefficient for gallium lies in the range $1.2 \leq \alpha \leq 2.5$. Geiger et al. [Geiger et al., 1987] have reported the vapour pressure over gallium, and have determined a value for the heat of vaporisation for the system, though they have not commented on the species type in the vapour. Their data is plotted in figure 1.5, as well as a vapour pressure curve determined from their heat of vapourisation value (264 kJ mol^{-1}) over a wider range of temperatures.

[6] Strictly, the rate equation is expressed in terms of the activities of various components and a more rigorous form of the equation is given in appendix B. Note that the activity of a substance is a dimensionless quantity.

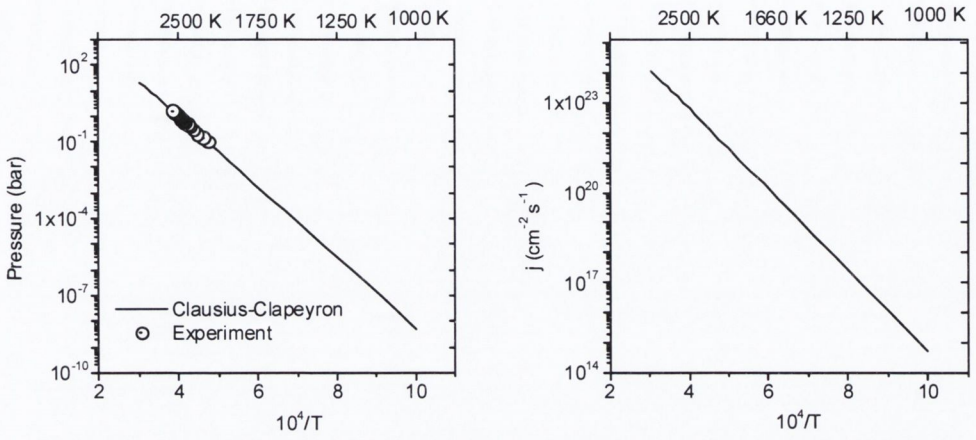

Fig. 1.5 (a) Experimental (circles) and calculated (line) vapour pressure over gallium (left) [Geiger et al., 1987]. (b) Evaporation rate of gallium as a function of temperature calculated using equation 1.6 and assuming an evaporation coefficient of unity. Note that the evaporation flux at typical film growth temperatures (~ 1000 K) is of the order of 10^{14} cm^{-2} s^{-1}.

1.2.3 Decomposition of GaN

The behaviour of GaN at high temperature has received much attention in the literature, indeed much of the earlier GaN publications were concerned with decomposition and the vapour pressure over GaN [Lorenz and Binkowski, 1962; Munir and Searcy, 1965; Schoonmaker et al., 1965; Groh et al., 1974]. It is unclear as to the nature of the evaporating species (whether Ga, N_2, or both), although experimental evidence suggests that GaN is not present in the vapour [Munir and Searcy, 1965; Groh et al., 1974]. Rather, GaN decomposes to Ga and N_2. In vacuum, it seems that the evaporation is non-stoichiometric, with excess gallium remaining on the surface after the heating process. In contrast, Munir and Searcy [Munir and Searcy, 1965] found that Ga and N_2 evaporated congruently from a GaN pellet in a Knudsen cell apparatus at temperatures up to 1200 °C, but only when the cell orifice to sample area ratio was maintained at a certain value. Newman [Newman, 1998b] has used Munir and Searcy's data to calculate the decomposition rate of GaN as a function of temperature (figure 1.6), using the Hertz-Langmuir-Knudsen equation (eq.1.6). For this work, a fit to Munir and Searcy's data

(figure 1.6), similar to Newman's approach, was used to model the evaporation flux (j_{GaN}) from laser ablated GaN targets is given by the following expression:

$$\log_{10} j_{GaN} = 27.4 - \frac{1.44 \times 10^4}{T_s} \text{ (cm}^{-2}\text{ s}^{-1}\text{)} \qquad \text{(eq. 1.7)}$$

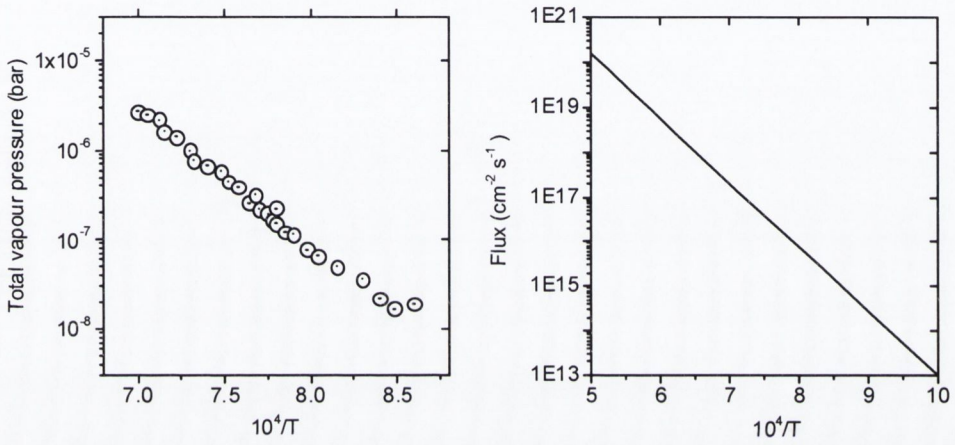

Fig.1.6 (a) Total vapour pressure over GaN [Munir and Searcy, 1965] (left) and (b) evaporation flux of GaN calculated using the vapour pressure data and equation 1.6.

1.3 GaN growth: N_2 pressure requirements

Can GaN be synthesised from Ga metal at these temperatures by choosing a suitable N_2 pressure? For an evaporation coefficient close to unity, one might expect this to be possible. However, measurements of the vapour pressure above heated GaN samples are orders of magnitude less than the N_2 pressures required to prevent decomposition, as illustrated in figure 1.7. Indeed, GaN synthesis from Ga metal and N_2 requires temperatures in excess of 1600 K and N_2 pressures of 15-20 kbar [Grzegory et al., 1993], and the growth rate quite slow (~0.1 mm per hour) even under these extreme conditions. These exceptionally high equilibrium N_2 pressure requirements indicate that the evaporation coefficient for GaN is quite low (compare with figure 1.6). The data in figure 1.7 will be referred to frequently in the thesis, since it has implications not only for film growth, but for temperatures at which nitride targets are prepared (section 3.2.1.1).

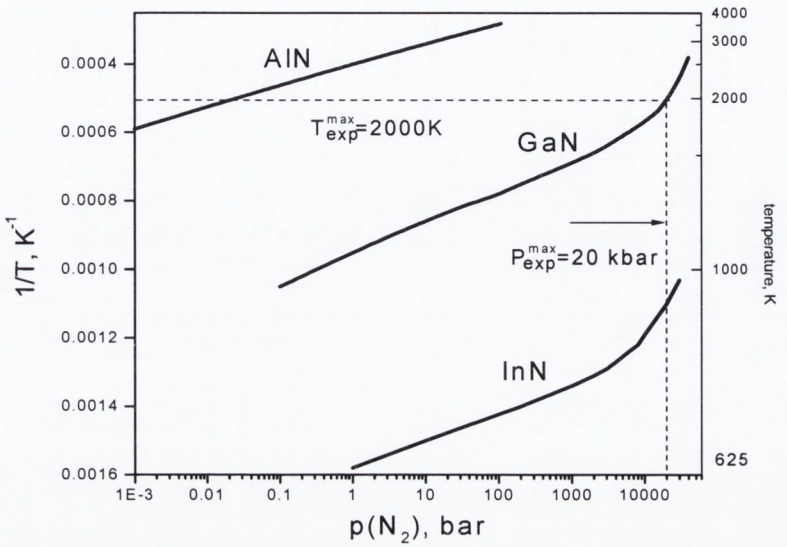

Fig. 1.7 Temperature variation of the equilibrium N_2 vapour pressure over AlN, GaN and InN. The dotted lines indicate the maximum temperature and pressures used in the measurements [Porowski and Grzegory, 1997].

1.4 Gases at high temperature/ plasma formation

1.4.1 High temperature gases

At room temperature, and at a typical PLD background gas pressure of 0.1 mbar (10 Pa), the density of an ideal gas is given by $n_g = N/V = p/k_B T$, which is approximately 2×10^{15} gas particles per cubic cm. Correspondingly, the Hertz equation (eq.1.1) shows that at this pressure and temperature, the flux of N_2 molecules striking a surface (e.g. of a film) is ~ 3×10^{19} cm^{-2} s^{-1}. Thus, one might expect the environment to promote GaN formation if the fraction of dissociated or excited N_2 molecules was only ~ 10^{-6}, since the GaN decomposition flux is ~ 10^{13} cm^{-2} s^{-1} at typical film growth temperatures (see figure 1.6). While the high velocity tail of the Maxwell-Boltzmann distribution allows for a small but non-zero probability of certain particles having speeds which are sufficient to dissociate or excite some of the molecules, the fraction is in fact insignificant[7] until a temperature of

[7] For example, the dissociation fraction for molecular nitrogen in air is only 0.0004 at 4000 K at atmospheric pressure. The fraction will be slightly greater at lower pressures since it depends inversely on the square-root of the gas density. For a detailed discussion, see [Zel'Dovich and Raizer, 1966].

several thousand Kelvin is reached (p.194, [Zel'dovich and Raizer, 1966]). This is because the fraction depends exponentially on $-U/k_BT$, where U is the energy of the excited or ionised state with respect to the ground state. Typical dissociation energies and first ionisation potentials of the common diatomic gases are greater than 5 eV, as is the lowest excited state for molecular nitrogen (6 eV), while k_BT is less than 0.1 eV. Thus, thermal plasmas, in which the ion, electron and gas temperatures (and densities) are comparable, are not practically sustainable, at least in the sense of maintaining a large volume of gas (i.e. the volume of a deposition chamber) at several thousand degrees Kelvin. Fortunately, the energetic laser ablation plasma plume can lead to excitation and ionisation of the background gas in PLD. Therefore, while N_2 is insufficiently reactive for GaN formation using other film growth techniques, it may still be a suitable gas in PLD of GaN. Such plume-gas interactions form the basis for the studies reported in chapters four and five.

1.4.2 Electrical discharge plasmas

An alternative means of establishing a plasma environment is to create non-thermal plasma, by means of an electrical discharge. In this case, electrons in a gas are accelerated through an electric field and, in doing so, excite and ionise gas particles if the electric field strength and electron mean free path in the gas are large enough to establish the required acceleration between collisions. The greater mass of the ions means that they experience considerably less acceleration in the electric field, and in any case, ions tend to thermalise quickly with the neutral gas atoms (which essentially have the same mass[8]) due to a high collisional cross-section with the neutrals. Therefore, the electron temperature is considerably greater than the ion temperature in electrical discharge plasmas (i.e. $T_{electron} >> T_{ion} \approx T_{gas}$).

[8] Ions differ in mass from neutral atoms only by an amount equal to Zm_e, where Z is the charge state of the ion and m_e is the electron mass which is ~ 5×10^{-4} times less than the proton mass.

1.4.3 Basic plasma properties

While plasma, by definition, is charge neutral (at least on a macroscopic scale) with equal numbers of ions and electrons, it maintains a positive (plasma) potential with respect to its confining boundaries (e.g. the chamber walls). This is due to the higher mobility of electrons compared to ions, and the tendency of ions to remain in a given region of space for a longer time. Similarly, if an electrode is inserted into the plasma, the electron flux[9] (charge per unit area per second) at the electrode surface will greatly exceed that of the ions, and as a result, quickly build up a region or sheath ("Debye" sheath) of negative charge. If the electrode is negatively biased so as to repel electrons, it will act as a positive ion collector. This is the basis of the Langmuir ion probe technique [Mott-Smith and Langmuir, 1926], which is used in this work and is discussed in greater detail in the following chapters.

Plasmas, unlike solid conductors and liquids, do not exhibit a simple linear voltage-current relationship between the two electrodes as in Ohm's law. This is because both electrons and ions can contribute to current transport, which is unlike the case of a solid or quasi-static liquid conductor where ions are essentially fixed in a flow (or "sea") of conduction electrons. Furthermore, while only electron scattering with fixed ions needs to be considered in solid conductors, collisions in plasmas can take place between any number of different particles such as electrons, atoms and diatomic species, of which atoms or molecules can be in neutral, excited or ionised states. To compound computational difficulties, collisions can be elastic or inelastic, with the latter encompassing a whole range of processes such as ionisation, excitation, relaxation and recombination, usually involving a third particle (see for example [Chapman, 1980c]). While the various scattering cross-sections in glow discharges are reasonably well known, particularly in the common gas discharges including N_2 (see, e.g. figure 1.8), the cross-sections for laser ablation plumes in a background gas are not. It follows that the dominant collisional processes in PLD in a background gas are not well understood. This

[9] Assuming charges (i.e. ions or electrons) within the plasma are described by an ideal gas speed $\bar{u}$, then the corresponding current flux at a surface in contact with the plasma, , $j=ne\bar{u}/4$ is simply related to the speed alone where n is the gas density. The factor of ¼ arises when considering the velocity components directed towards the surface and integrating over a solid angle of π (see for example, [Chapman, 1980]).

of course has a critical effect on setting the parameters for film growth, since it is unclear as to what energies (fluence) or background gas pressure (i.e. gas density) are required to achieve sufficient excitation or ionisation. The following chapter considers some of the characteristics of laser produced plasmas.

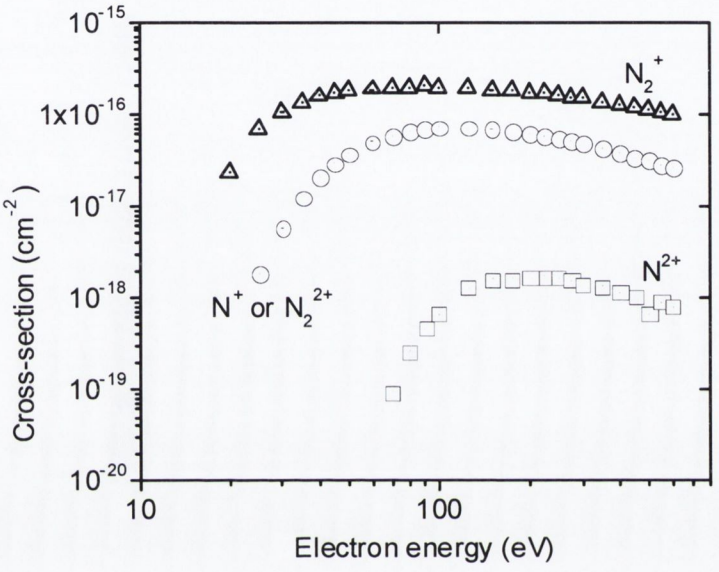

Fig. 1.8 Ionisation cross-section for N_2^+, N_2^{2+}, N^+ and N^{2+} production by electrons in N_2 . N^+ and N_2^{2+} have the same charge to mass ratio, and are thus indistinguishable in charge to mass studies (from [Tian and Vidal, 1998]).

2. Theory and modelling

PLD can generally be described as the removal (ablation) of a thin layer of material from a solid or liquid target using a high power, pulsed laser (~ 10 MW, pulse FWHM~10 ns), followed by a projection of the ablated material away from the target, and finally deposition of some of this material on a suitable substrate (for in-depth discussion on laser ablation and PLD see, for example, [Singh and Narayan, 1990; Chrisey and Hubler, 1994; Haglund and Miller, 1998]). The following sections summarise the theory used to develop a number of models describing each of these features.

2.1 Absorption and heating near the target surface

The surface temperature (T_s) rise and ablation rate in high intensity laser irradiation of a surface will depend greatly on the surface reflectivity and the electronic structure of the material. Since this work involves laser ablation of two materials which differ considerably under these headings, i.e. Ga (a metal) and GaN (a wide bandgap semiconductor), it is useful to consider the optical absorption and heating mechanisms for both. Much of the terminology introduced in the following sections is detailed further in appendix C.

2.1.1 Laser heating of a metal

In metals, both the surface reflectivity and the extinction coefficient (k, the imaginary component of the refractive index) are relatively high at visible and UV wavelengths, and coupling of the incident photon energy to the solid takes place predominantly through absorption of the incident radiation by conduction electrons. Although energy coupling in electron-phonon collisions is comparatively inefficient due to momentum mismatch, thermalisation times in metals are reported to be of the order of a few picoseconds [Wang et al., 1994; Haglund, 1998b]. For UV laser pulses, the optical absorption depth

$\left(d_{opt} = \frac{\lambda}{4\pi k} \sim \frac{\lambda}{20}\right)$ is typically[10] only ~10 nm, since the extinction coefficient is in the range (1-5) in the UV for most metals. On the other hand, the heat diffusion depth, $d_{diff} = \sqrt{Dt_{pulse}}$ (D = thermal diffusivity), for ns pulses is often up to 1 micron. The temperature rise can be suitably described by a one dimensional heat conduction model if the following conditions are valid [Ready, 1971; Von Allmen, 1987a]:

i. The timescale over which the laser energy is coupled to the target material (i.e. thermalisation time) is much shorter than the laser pulse duration.
ii. The laser pulse energy is absorbed in a depth near the target surface which is much less than the heat diffusion depth over the timescale of the laser pulse.
iii. The absorption depth is considerably less than the spot dimensions

The model is likely to yield reasonably accurate comparisons with experiment at low laser fluence ($\leq$1 J cm^{-2}), particularly for laser ablation of metals near the ablation threshold. However, it does not account for material removal by exfoliational sputtering which may be significant, particularly in the case of ceramic target ablation [Kelly et al., 1998] (reduced surface reflectivity and strong absorption of the incident laser at grain boundaries and defect sites will often lead to preferential ablation of these regions [Gunster et al., 2001]). Furthermore, ablation is not accurately described by the Hertz-Langmuir equation if the surface temperature is close to, or exceeds, the critical temperature of the target material (i.e. when $T_s \geq 0.8\ T_{cr}$)[11] [Fucke and Seydel, 1980; Von Allmen, 1980].

2.1.2 Laser heating of a wide bandgap semiconductor

For laser irradiation of high purity single crystal wide bandgap ($E_g \geq 1$ eV) semiconductors with photon energy $h\nu > E_g$, one might expect the absorption process to

[10] Assuming this order of ablation depth, a quick estimate of the mass loss (density of Ga = 5.9 g cm^{-3}) for a laser spot size of ~ 1 mm diameter, yields a value of approximately 0.1 μg per shot (~ 10^{15} Ga atoms).
[11] At the critical temperature, a substance can no longer remain in a liquid state, regardless of pressure. When a liquid is superheated ($T > T_{cr}$), vapour nuclei are formed and grow rapidly within the liquid leading to an explosion of the vapour-liquid mixture. This is often termed "phase explosion". There are a number of anomalous features associated with materials whose temperature exceeds the critical point including large fluctuations in density and a sudden drop in electrical conductivity.

be dominated by interband absorption, where each incident photon creates an electron-hole (e-h) pair, eventually resulting in an e-h plasma [Von Allmen, 1987b]. However, as indicated in section 1.1.4, polycrystalline pressed powder pellets have a high concentration of defects, and nitride powders in particular have high background (electron) carrier concentrations [Slack, 1973]. Thus electron-electron collisions are likely to dominate[12] [Von Allmen, 1987b]. Metallisation (i.e. preferential evaporation of the gaseous element, e.g. N in GaN) of the target surface seems to be a common phenomenon in ns laser irradiation of wide bandgap semiconductors [Haglund, 1998a; Gyorgy et al., 2001]. The threshold for the onset of metallisation has been linked to the ionicity[13] of the bond [Ichige et al., 1988], which in turn is related to the bond strength [Phillips, 1970]. For the purpose of this work, where the laser fluence used is well above the ablation threshold (< 100 mJ cm^{-2}), extensive decomposition and metallisation is to be expected. The use of a one dimensional heat conduction model to describe laser heating of GaN is not unreasonable since the condition of $d_{diff} >> d_{opt}$ is approached as the laser photon energy exceeds the bandgap energy (see figure 1.3b). At 248 nm (5 eV), the ratio of the diffusion depth to the absorption depth is 10 (table 1.1), and the gallium rich nature of ns laser ablated GaN targets is likely to further increase the effective absorption coefficient (and thus the ratio). Interestingly, a number of groups have demonstrated that decomposition of laser ablated nitride targets can be avoided when using ps or fs pulses suggesting that thermalisation times are indeed of the order of ps [Gyorgy et al., 2001; Hirayama et al., 2001].

2.1.3 Plasma absorption

While ionisation in the vapour over the target is likely to become significant as the temperature reaches several thousand Kelvin via the Saha equation (p.194, [Zel'dovich and Raizer, 1966]), absorption of laser photons by electrons via inverse bremsstrallung leads to further heating and ionisation of the gas, particularly in the infra-red. For UV wavelengths, photoionisation is believed to be the dominant ionisation process, and the

[12] In any case, electron-hole thermalisation times, although greater than those associated with electron-electron or electron-lattice (phonon) collisions, are reported to be no longer than ns duration

[13] Bond strengths in compound semiconductors are often scaled according to its likeness to a truly covalent or ionic bond. For a detailed discussion on ionicity scaling in crystals, see for example [Phillips, 1970] and references therein.

degree of photoabsorption can be characterised by a cross-section which is of the order of 10^{-17} cm^2 (pp.264-277, [Zel'dovich and Raizer, 1966]). This is the threshold value of the hydrogen-like photoionisation cross-section given in [Zel'dovich and Raizer, 1966] and has been used previously in modelling ns ablation of Fe and Mn targets [Lunney and Jordan, 1998].

2.1.4 Model for laser heating of the target

Using Duhamel's theorem [Carslaw and Jaeger, 1986], the solution to the one-dimensional heat conduction equation for a time-varying heat source at the surface yields the following expression for the surface temperature, T_s [Ready, 1971]:

$$T_S(t) = \frac{1}{\sqrt{\kappa\rho\pi C}} \int_0^t \frac{I(t-\tau)}{\sqrt{\tau}} d\tau \qquad \text{(eq. 2.1)}$$

Here, κ, ρ and C are the thermal conductivity, mass density and specific heat capacity of the target, respectively. The irradiance at the target surface contains a term which accounts for plasma absorption by the evaporated particles, ρ_{vap} (i.e. the total number of vapour particles accumulated up to a time t) as follows [Lunney and Jordan, 1998]:

$$I(t) = (1-R) I_l(t) \exp\left[\frac{\sigma_{vap}\rho_{vap}}{\cos\theta_0}\right]$$
$$\rho_{vap}(t) = \int_0^t j_{vap} d\tau \qquad \text{(eq.2.2)}$$

θ_i is the angle of incidence of the laser beam with respect to the target normal, and σ_P is the photo-absorption cross-section at the incident laser wavelength which, was taken as 10^{-17} cm^2 (section 2.1.3).The number of particles vaporised per unit area per unit time, j_{vap}, can be determined using a suitable vapour pressure relation (e.g. eq. 1.3 or eq. 1.6). I_l is the input laser intensity (W cm^{-2}) at the target, before accounting for the reflectivity of the target surface, R. An analytical expression for the laser intensity was obtained by using a fit to the pulse profile measured using a fast photodiode (see Appendix D). The

calculation was evaluated numerically using the *Mathematica* software and the code for the routine is contained in appendix (appendix E).

Figure 2.1 shows the temperature rise calculated using the model for gallium ($R = 0.8$) ablated at a fluence of 2.5 J cm^{-2} using the n and k values listed in table 2.1. The corresponding vapour pressure over a Ga target predicted by the ablation model is also plotted (right), as is the variation in the peak vapour pressure with fluence (inset). Although thermal conduction regulates heat dissipation as $1/\sqrt{\tau}$ (eq. 2.1), the exponential photo-absorption term dominates at higher fluence when the high evaporation flux effectively shields the target from incoming radiation. In agreement with the experimental results of Dyer et al., [Dyer et al., 1992], the peak vapour pressure is of the order of MPa when using a fluence of a few J cm^{-2}, which must be accounted for when using liquid (Ga) targets.

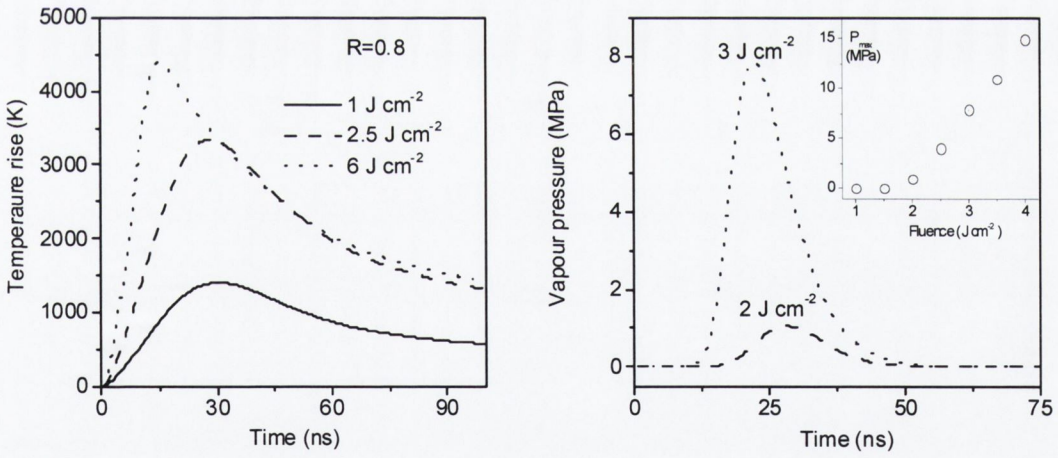

Fig. 2.1 Surface temperature rise for laser (26 ns, 248 nm) heating of gallium targets, for different fluences using a surface reflectivity of 0.8 (the calculation includes the photo-absorption term). The panel on the right shows the vapour pressure profiles corresponding to the surface temperature rise calculated when using a fluence 2 J cm^{-2} and 3 J cm^{-2}, with the peak pressure plotted vs fluence in the inset.

2.2 Expansion of the laser ablation plume

While the initial stages (near the target) of the laser produced plasma expansion in either high vacuum or a low pressure gas are quite similar[14] [Kelly and Dreyfus, 1988; Anisimov et al., 1993], the expansion characteristics can vary considerably at typical target-substrate distances of a few cm, depending on the background gas pressure. The following sections summarise the behaviour of the expansion in a number of these regimes.

2.2.1 Expansion in high vacuum

At low background gas pressures ($< 10^{-3}$ mbar), the expansion of the plasma plume is essentially self-similar once an acceleration region of the first few mm or so above the target is traversed, after which the plume front velocity remains almost constant. The angular distribution of an expansion can be described using the solution to the hydrodynamic equations of Anisimov et al. [Anisimov et al., 1993; Hansen et al., 1999]:

$$N(\theta) = N_0 \left(\frac{1}{1 + (\kappa^2 - 1)\sin^2(\theta)} \right)^{3/2} \qquad \text{(eq. 2.3a)}$$

Here, N_0 is the integrated flux at the normal (substrate) position ($\theta = 0$) and the "κ" value is the asymptotic ratio of the plasma expansion boundaries along and perpendicular to the target normal (see figure 2.2). Although this parameter depends on the ratio of the heat capacities γ and the initial plasma dimensions [Hansen et al., 1999], which are not easily measured, it can be obtained experimentally by fitting ion flux data (the variation in the angular distribution with κ is illustrated in figure 2.2). The time-integrated ion flux per pulse can be calculated by integrating this function over the solid angle subtended by the plume (approximately 2π), yielding:

[14] The mean free path between collisions in the Knudsen layer is much shorter than the corresponding MFP in the background gas

$$N_{total} = N_0 \frac{2\pi d^2}{\kappa^2} \qquad \text{(eq.2.3b)}$$

Here, the distance from the target at which N_0 is measured is given by d. For non circular laser spots, the plume profile will differ depending on the axis about which the expansion takes place. If the laser spot is approximated as an ellipse, the κ^2_{term} in equation 2.3b is replaced by $\kappa_A \kappa_B$, where κ_A and κ_B are the κ values corresponding to both directions (see figure 2.2, right).

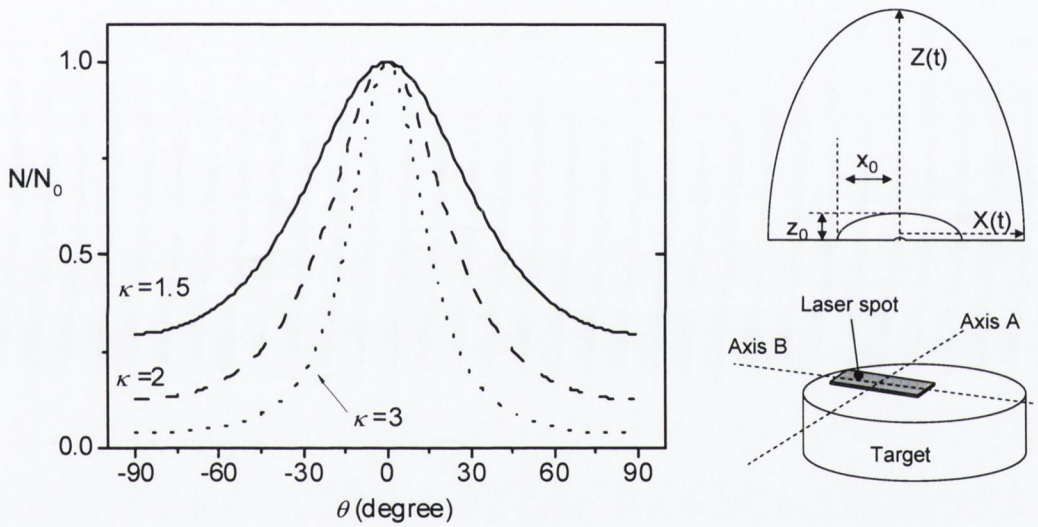

Fig. 2.2 Angular distribution of total integrated flux given by the Anisimov model for different κ values. The "κ" value is represented by the ratio of the semi-minor and semi-major radii of the ellipsoid (=X(t)/Z(t)) in top right schematic. The probe can be rotated about the two axes of the laser spot (labelled "A" and "B" in the bottom right schematic) to obtain a κ value for each axis.

2.2.2 Expansion in a background gas

2.2.2.1 Scattering at low pressure

At low background pressures, scattering will cause some broadening of the angular distribution of the plume and a reduction of the number of ablated particles reaching a

substrate placed directly in front of the target [Wood et al., 1998]. If it is assumed that this behaviour can be described by a simple Beer's law model [15] (see, for example, p.219 [Born and Wolf, 1999]), then the number reaching a given point will reduce exponentially with increasing gas density $n_g \left(= {}^{p}/_{k_B T} \right)$ as:

$$N(n_g) = N_0 \exp\left(-n_g \sigma_g d\right) \qquad \text{(eq.2.4)}$$

Here d is the target-probe distance and σ_g the scattering cross-section [Chapman, 1980b; Wood et al., 1998]. The mean free path of the particles in the gas is simply given by ${}^{1}/_{n_g \sigma_g}$. This model is later used to determine the scattering cross-section for ions in N_2 (chapters 4 & 5).

2.2.2.2 Shock front formation

When the gas pressure is increased such that the mean free path of the plume particles in the background gas is reduced[16] to ~ 1 cm, the collision of the ablation plume with the gas launches a shock-wave. In a regime where the shock wave is fully developed at an early stage of the expansion (i.e. near the target), the plume can be thought of as a piston driving out against the background gas and accumulating gas particles on its way. The description of this process is somewhat simplified if it is treated as a point explosion, and the radius of propagation can be written as (p.97,[Zel'dovich and Raizer, 1966]):

$$R(t) = \xi_0 \left(\frac{E}{\rho_0} \right)^{1/5} t^{\eta} = B t^{\eta} \qquad \text{(eq. 2.5)}$$

[15] This law assumes hard-sphere, elastic scattering from fixed targets. The requirement that the background gas behave as fixed particles can be approximated since, at room temperature, the mean velocity of an ideal gas of molecular weight = 28 g mol^{-1} (molar mass of an N_2 molecule) is ~ 400 m/s, which is significantly less than typical ion velocities for these laser ablation plasmas (> 10^4 m/s). The approximation is especially valid if the background gas particles are much heavier than the projectiles (i.e. the plume species).

[16] Plume diagnostics are typically carried out at a few cm from the target. Therefore, formation of a shockwave formation must take place within this range in order for the phenomena to be observed. In addition, a shockfront is maintained as long as the outward plume pressure is much greater than the backgound gas pressure; a condition which will only hold within a limited distance (~1 cm) from the target.

ξ and E are constants for a particular expansion and are primarily determined by the specific heat ratio γ and the mass density of the layer ρ_0. In the case where the expansion can be approximated as being spherical, the exponent η is equal to 2/5. The radial propagation velocity can be written as:

$$\frac{dR(t)}{dt} = \eta B t^{\eta-1} \qquad \text{(eq. 2.6a)}$$

By measuring the TOF at various distances from the target and fitting the data, η and B can be determined, and thus the expansion velocity can also be calculated. Otherwise, substituting for t in terms of R, allows the velocity (v) and kinetic energy to be written in terms of the radial distance[17]:

$$v = \frac{dR}{dt} = \eta B \left(\frac{R}{B}\right)^{1-1/\eta} \qquad \text{(eq. 2.6b)}$$

$$K.E. = \frac{1}{2} m_{ion} v^2 = \frac{1}{2} m_{ion} (\eta B)^2 \left(\frac{R}{B}\right)^{2\left(1-1/\eta\right)} \qquad \text{(eq. 2.6c)}$$

A simple model can be used to estimate the total number of background gas particles accumulated in this manner, assuming that the expanding plume accumulates all background gas particles in its path (see figure 2.4). The number of particles in a volume V_θ described by a solid angle $d\theta$ and radius r is:

$$N_\theta = n_g V_\theta = n_g \times \frac{1}{3} \pi (r d\theta)^2 \qquad \text{(eq. 2.7)}$$

[17] In the case of a spherical approximation (η=2/5). Therefore, the velocity and the kinetic energy are simply related to the propagation distance as: $v \propto R^{-3/2}$ and $K.E. \propto R^{-3}$.

The number of particles accumulated per unit surface area of the expanding plume:

$$N_\theta / Area = n_g \times \frac{1}{3}\pi(rd\theta)^2 \times 1/\pi(rd\theta)^2 = \frac{r}{3} n_g \qquad \text{(eq. 2.8)}$$

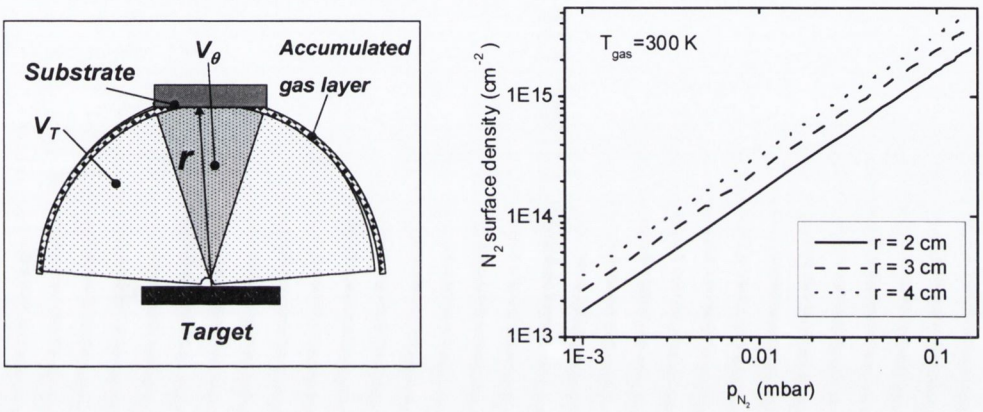

Fig. 2.3 Schematic of background gas accumulation model (left). The total volume swept out by the plume is represented by the lightly shaded region (VT), while the volume swept out towards the substrate (V_θ) is darkly shaded. Also included (right) is the density of particles accumulated on the surface of the expansion at various distances from the target (plotted vs gas pressure).

Although this is a very much simplified argument which ignores any complex gas dynamics, it serves as a useful guide to the number of N_2 molecules which can be activated by the energetic expanding plume (the surface density as a function of gas pressure is plotted in figure 2.4).

2.2.3 Probe theory

The expansion dynamics of laser ablation plumes can be monitored quite sensitively with an electrostatic ion probe placed a few cm in front of the target surface [Hansen et al., 1999; Toftmann et al., 2000]. The probe consists of a few mm of a thin metal wire exposed beyond an insulating casing, or an exposed area of a metal electrode. In ion detection mode, the probe is negatively biased to repel electrons and thus detects a pulse

of ion current due to the flow of the ablation plasma past the probe position. It can be used to determine the ion density, ion flux and the energy distribution of the ions arriving at the substrate. The ion current measured by the probe when sufficiently negatively biased (usually $V_{bias} \leq 25$ V is adequate), can be described by a flow of particles through an exposed area A_n normal to the probe with a characteristic velocity v. The ion current can be written in terms of the current density n_j and charge on the ions eZ as follows [Mott-Smith and Langmuir, 1926; Koopman, 1971, 1972]:

$$I_{ion} = (1 + \varepsilon_{se}) A_n \left(\sum_j n_j e Z_j \right) v \sqrt{1 + \frac{2e(V_{bias} - V_p)}{m_i v^2}} \qquad \text{(eq. 2.9a)}$$

Here, V_p is the plasma potential (section 1.5.3) while m_i is the ionic mass. The subscript j facilitates the description of ions with different charge state, but since a number of groups [Pronko et al., 1999; McKiernan and Mosnier, 2002] have reported that, at low to medium laser fluence (1-5 J cm^{-2}), the plasma plumes of laser ablated Ga and GaN targets were predominantly singly charged (Ga^+) at target-probe distances of ≥ 1 cm, Z is assumed to be +1. ε_{se} is a factor which accounts for secondary electron emission (see section 6.2.1) due to ion bombardment of the probe which is generally less than 0.5 [Koopman, 1972]. The term under the square root is very close to unity, since mv^2 is typically of the order of several hundred eV (particularly at the maximum ion flux), while $|V_{bias}|$ is typically maintained at -25 V. The expression for the ion current can then be approximated in terms of the ion density (n_i) by:

$$I_i(t) \cong n_i(t) e A_n v_{TOF} \qquad \text{(eq 2.9b)}$$

The flow velocity of the ions can be determined from the time of flight (TOF) measured by the probe (see figure 2.5): $v_{TOF} = d/t_{TOF}$. The kinetic energy associated with a particular time-of-flight is simply:

$$\frac{1}{2} m_{ion} v_{TOF}^2 \qquad \text{(eq.2.10)}$$

If the identity and charge state of the ions are known, then the ion flux per pulse (i.e. number of ions per unit sampling area of the probe) can be determined by integrating the area under the TOF curve. For a voltage drop, $V(t)$, across the series resistor, R, in the probe circuit (figure 3.6a) the time integrated ion flux (J_{ion}) [18] is given by:

$$J_{ion} = \frac{1}{RA_n e} \int^{t} V(t)dt \qquad \text{(eq. 2.11)}$$

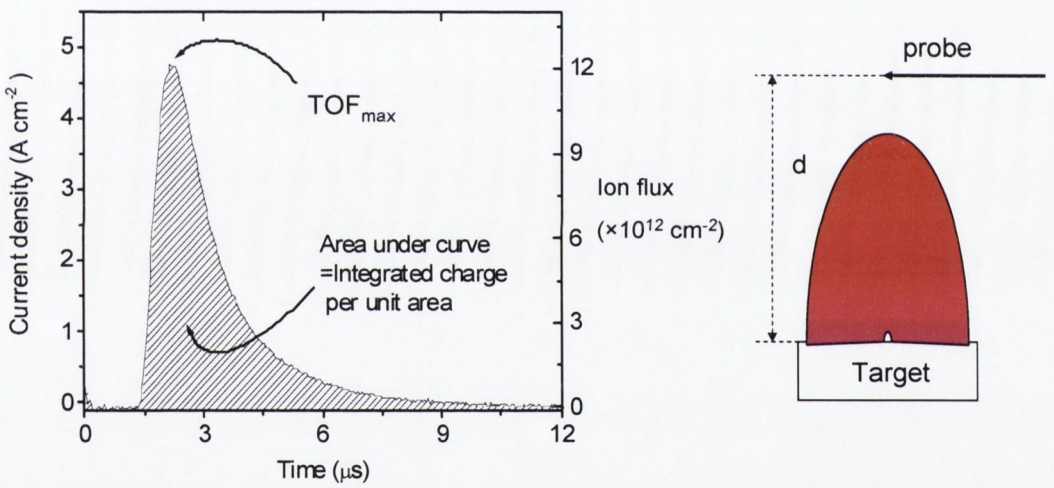

Fig. 2.4 Typical ion probe signal displayed in units of current per cm^2 (left axis). The raw data is a voltage signal corresponding to the voltage drop across the resistor in series with the discharge capacitor in the Koopman circuit (figure 3.5). The right-hand scale shows the corresponding instantaneous flux (per 0.05 μs time acquisition step) assuming $Z = +1$. The total integrated ion flux per pulse is obtained by integrating over the time duration of the pulse (i.e. the area under the curve). A schematic of the target-probe configuration is on the right (see section 3.3.1 for setup).

The ion energy distribution within the plasma can also be determined from TOF probe measurements using the following relationship:

[18] This is the total number of ions per unit area (usually expressed per square cm) collected by the probe, after one laser shot. Hereafter, it will be referred to as the "integrated ion flux".

$$\frac{1}{A_n}\frac{dN(t)}{dE} = \frac{1}{A_n}\frac{dN(t)}{dt}\frac{dt}{dE} = \frac{1}{A_n}\frac{V(t)}{eR_{load}}\frac{t^3}{m_{ion}d_{probe}^2} \qquad \text{(eq. 2.12)}$$

2.3 Deposition and film growth

2.3.1 Characteristics of film growth in PLD

The preceding sections suggest a number of aspects of pulsed laser ablation which are potentially advantageous for thin film deposition. These include a high instantaneous flux which can be easily controlled by varying the laser fluence or pulse repetition rate and a plume whose kinetic energy can be harnessed to drive chemical reactions with a background gas or contribute to mobility on the film (or substrate) surface. Conversely, these properties can be detrimental to the film growth process. For example, if the flux and cluster concentration is too high, 3D (Volmer-Weber) nucleation and growth might be expected [Horwitz and Sprague, 1994], while particulate expulsion from the target usually leads to particulate accumulation in the film. Furthermore, ions with energies of the order of several hundred eV are likely to cause sputtering of the film or substrate surface [van de Riet et al., 1993]. Zalm [Zalm, 1984] has developed an expression which can be used to estimate the sputtering yield (Y_F) for atoms (atomic weight = Z_F) in the film due to projectile ions (kinetic energy in keV = E_p, atomic weight = Z_p) impinging on the surface, which depends on the cohesive energy per atom (U_0, in eV) of the film atoms[19]:

$$Y_F(E_p) = \frac{1.9}{U_0}\left(\frac{Z_F}{f}\right)^{1/2}\left(E_p - 0.09\sqrt{U_0}\right)$$
$$f = \frac{1}{2}\left[\left(\frac{Z_F}{Z_p}\right)^{2/3} + \left(\frac{Z_p}{Z_F}\right)^{2/3}\right] \qquad \text{(eq. 2.13)}$$

[19] This expression is in fact the low energy approximation of a model developed for sputtering of elemental amorphous targets by atomic ion bombardment (i.e. as is sputtering guns), where the energy is typically in the keV range. The approximation is outlined in [Zalm, 1984].

Noting that the cohesive energy of Ga is 2.81 eV (p.57, [Kittel, 1996]), the yield becomes significant ($\geq$ 1%) once the ion energy exceeds ~ 25 eV for Ga ions incident on a Ga film. For the purpose of GaN film growth, it is important to establish a number of guidelines with regard to setting the substrate temperature and limiting the kinetic energy of the plume. In accordance with well-established sintering practice [German, 1996], substrate temperatures in thin film growth are typically chosen to be (0.5-0.66) of the melting temperature [Newman, 1998a], in order to promote crystallisation. This approach would be impractical for GaN film growth, both from a temperature (1250 °C-1650 °C) and N_2 pressure (i.e. to prevent decomposition, see fig.1.7) point of view. Since deposition rates in PLD at moderate fluence are of the order of 10^{15} cm^2s^{-1} at a repetition rate of 10 Hz, the maximum substrate temperature should be limited to ~ 800 °C, to avoid significant decomposition of the film (figure 1.6). Finally, because surface mobility is limited by these temperature restrictions, the plume energy is likely to play an important role in film nucleation and crystallisation. Newman [Newman, 1998b] has suggested that moderate ion energies (5-10 eV) may produce a substantial enhancement in surface diffusion in GaN film growth, but also indicated that the kinetic energies of the reacting species should not exceed 27 eV. This upper limit on the kinetic energy is related to the energy required to cause bulk displacements in (or sputtering of) the GaN lattice.

2.3.2 Theory of optical reflectometry

Optical reflectometry is an in-situ, non-destructive, monitoring tool which can provide valuable information regarding the optical properties and thickness of a film during growth [Aspnes, 1982; Dodd et al., 1994]. It is particularly suitable for analysing the growth of dielectrics or wide bandgap semiconductor thin films, which exhibit weak absorption at the monitoring laser wavelength. For these materials, the amplitude of the reflected intensity oscillates periodically, with little damping of the amplitude, as the thickness of the film increases. The film growth rate can be determined from the oscillation period which corresponds to a thickness of $\frac{\lambda}{2n}\cos\theta_0$ where λ is the laser wavelength, n is the refractive index of the film and θ_0 is the angle of incidence (p.67 [Born and Wolf, 1999]). The theory of thin film reflectivity on a bulk substrate has been

discussed by a number of authors [Heavens, 1965; Born and Wolf, 1999] and for this brief overview, the notation of Heavens is used where the positive and negative superscripts denote the direction of the incident and reflected electric vectors, respectively.

2.3.2.1 Fresnel equations (Bulk reflectivity[20])

The Fresnel equations describing the ratio of the incident and reflected electromagnetic wave amplitudes at an interface can be obtained by applying Gauss' theorem to the solutions of Maxwell's equations over the volume of an infinitely small cylinder (with its axis of symmetric rotation normal to the surface) at the interface (see chapter 1 [Born and Wolf, 1999]). Using the solutions to Maxwell's equations for a sinusoidal wave propagating from a medium of complex refractive index $\hat{n}_0$ to another of index $\hat{n}_1$, and Snell's law (which relates the angles of incidence (θ_0) and refraction (θ_1) and the interface), the Fresnel coefficients can be written as:

$$r_{1p} = \frac{E_{0p}^{-}}{E_{0p}^{+}} = \frac{\hat{n}_0 \cos\theta_1 - \hat{n}_1 \cos\theta_0}{\hat{n}_0 \cos\theta_1 + \hat{n}_1 \cos\theta_0} \qquad \text{(eq. 2.14a)}$$

$$r_{1s} = \frac{E_{0s}^{-}}{E_{0s}^{+}} = \frac{\hat{n}_0 \cos\theta_0 - \hat{n}_1 \cos\theta_1}{\hat{n}_0 \cos\theta_0 + \hat{n}_1 \cos\theta_1} \qquad \text{(eq. 2.14b)}$$

In these coefficients expressions, the subscripts p and s denote the components of the electric vector (amplitude $=E_0$) paralell and perpendicular to the plane of incidence[21], respectively. In experiment, the ratio of the incident and reflected intensities is more easily measured, with the intensity being proportional to the square of the electric field amplitude. Thus, the reflectivity is simply defined as the square of the absolute value of the Fresnel coefficients. The s- and p-polarized reflectivity for bulk Ga and GaN surfaces, calculated using the optical constants listed in table 1, are plotted in figure 2.5 below.

---

[20] Reflectivity is expressed as the reflected light intensity as a fraction of the incident intensity. More recently, the term "reflectance" has replaced reflectivity. The quantities are identical.

[21] With the exception of X-ray optics, the plane of incidence is usually defined such that it contains the incident ray, the reflected ray and the reflecting surface normal.

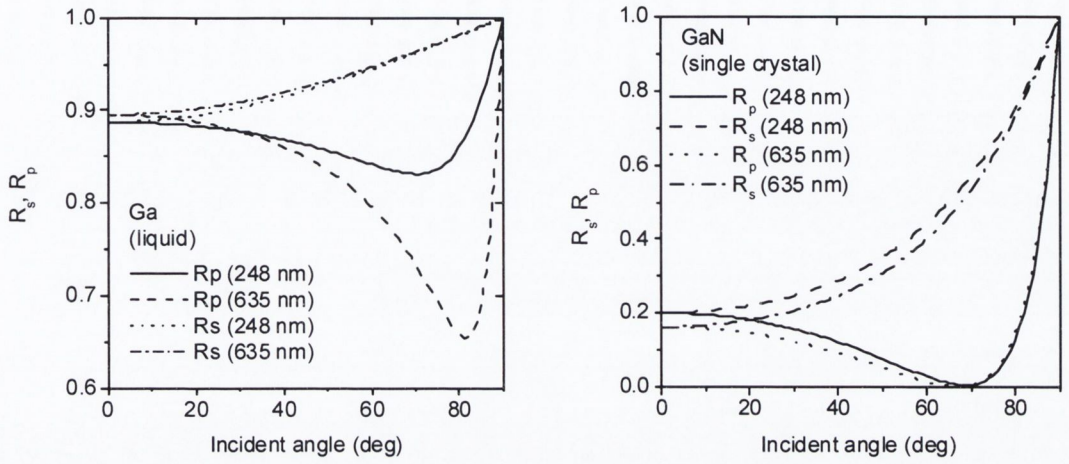

Fig. 2.5 s- and p-polarized reflectivity for GaN (left) and Ga (right) at the excimer (248nm) and optical reflectometry (635 nm) laser wavelengths (see table 1.1 for the n and k values used).

2.3.2.2 Effective medium approximation

To account for non-stoichiometry or the incorporation of other materials which can lead to a change in the effective dielectric constant of a material, an effective medium approximation can be made using one of a number of models, depending on the nature of the mixing of materials [Rossow, 1995]. These models are derived from the Clausius-Mossotti expression, which relates the polarizabilities, α_j, of different components in a medium, with the effective permittivity of the medium [Aspnes, 1982]:

$$\frac{\varepsilon - 1}{\varepsilon + 2} = \frac{1}{3\varepsilon_0} \sum_j N_j \alpha_j \qquad \text{(eq. 2.15)}$$

Here, the volumetric dipole density of the j^{th} component is given by N_j and ε_0 is the permittivity of free space. A number of conditions should be met for this relation to be valid; in particular, the material should be macroscopically homogeneous in order that diffraction from surface or bulk structures can be neglected. Furthermore, in the above expression, the polarisability is a scalar, which strictly only applies in the case of an isotropic structure. In general, the polarisability may be anisotropic and described by a

higher order tensor (more usually, the susceptibility tensor is used to describe the dielectric properties of a material). However, the measured birefringence of GaN wurtzite crystals is quite small at visible wavelengths[Dingle et al., 1971][22], and its polarizability is treated as a scalar in the following calculations. For a two-component medium, where the mixing concentrations are comparable [Aspnes, 1982], the effective permittivity is best described by the Bruggemann relation [Bruggemann, 1935; Rossow, 1995]:

$$f\frac{\varepsilon_p - \varepsilon_{eff}}{\varepsilon_p + 2\varepsilon_{eff}} = (1-f)\frac{\varepsilon_h - \varepsilon_{eff}}{\varepsilon_h + 2\varepsilon_{eff}} \qquad \text{(eq. 2.16)}$$

This expression relates the permittivity of the constituents (ε_h, ε_p) to that of the medium (ε_{eff}) in a random-mixture microstructure where f is the volume fraction of the particles with permittivity ε_p embedded in the matrix of a host material with permittivity ε_h. An expression for the effective permittivity can be obtained by solving the Bruggemann relation (eq. 2.17):

$$\varepsilon_{eff} = \frac{1}{4}\left(2\varepsilon_h - 3f\varepsilon_h - \varepsilon_p + 3f\varepsilon_p \pm \sqrt{8\varepsilon_h\varepsilon_p + \left(2\varepsilon_h - 3f\varepsilon_h - \varepsilon_p + 3f\varepsilon_p\right)^2}\right) = \varepsilon_1 + i\varepsilon_2$$

This expression can be used to determine the effective optical constants of a GaN-Ga mixture, since n and k are related to the real and imaginary components of the permittivity by $\hat{n} = n - ik = \sqrt{\hat{\varepsilon}}$ [Heavens, 1965] (the relationship between the dielectric permittivity and the refractive index is outlined in greater detail in appendix C).

[22] This data showed a relatively small reflectivity difference (~0.01) for light polarised parallel and perpendicular to the c-axis from (290-380) nm which only became significant at UV wavelengths.

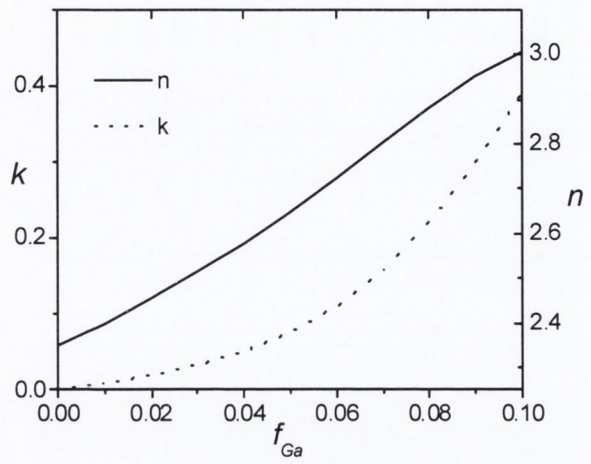

Fig. 2.6
Optical constants of a GaN-Ga mixture determined using the Bruggemann relation for a Ga fraction of 0 - 0.1. The curves were calculated using the optical constants for liquid gallium and single crystal GaN as listed in table 1.1.

2.3.2.3 Reflection from a single layer film

An electromagnetic wave incident on a layer which has been deposited on a substrate will undergo numerous reflections between the ambient-film and film-substrate interfaces (figure 2.7).

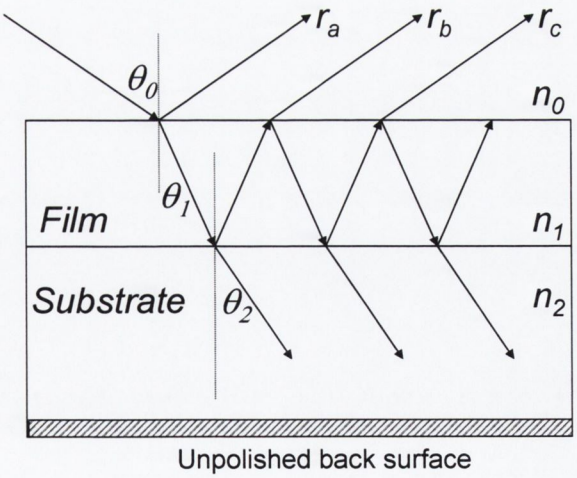

Fig. 2.7
Illustration of beam propagation in a single layer film as it undergoes numerous reflections at the ambient-film and film-substrate interfaces. Reflections from the unpolished backside of the substrate are assumed to be negligible.

The total amplitude of the reflected wave is given by the summation of the individual reflections which from figure 2.7 can be expressed as the infinite series $r_{total} = r_a + r_b + r_c + \ldots$. Here, r_b, r_c and higher order terms contain a phase factor, β, associated with the path travelled by the beam, of wavelength λ, in a film of thickness d:

$$\beta = \frac{2\pi}{\lambda} n_1 d \cos\theta_1 \qquad \text{(eq. 2.18)}$$

Fortunately, this infinite series can be expressed solely in terms of the Fresnel coefficients at the ambient-film (r_1) and film-substrate (r_2) interfaces and the phase factor with the reflected intensity given by:

$$R = \left(Abs\left(\frac{r_1 + r_2 e^{-2i\beta}}{1 + r_1 r_2 e^{-2i\beta}} \right) \right)^2 \qquad \text{(eq. 2.19)}$$

The *s*-polarized reflectivity of pure GaN on sapphire at 635 nm, predicted by the model, is plotted *vs* film thickness in figure 2.8 (top panel). Also included is the reflectivity for films containing 0.05 and 0.1 volume fraction of Ga as predicted by the Bruggemann model. The values of n (1.4) and k (6.9) for gallium at 635 nm were taken from table 1.1, as were the optical constants for GaN. The reflectivity *vs* thickness curves presented in figure 2.8 were calculated using values of $n = 2.35$[Yu et al., 1997] and $k = 0.0005$ [Ambacher et al., 1996] which were determined from MOCVD-grown wurtzite GaN thin films (see figure 1.3). Previous reflectivity measurements at 670 nm using GaN films grown by PLD revealed that the index was given by $\hat{n}_{film}$ =2.23 - *i* 0.027 [Cole, 1998].

To conclude the discussion on the reflectivity model, it is worth noting that a simple expression can be included to account for the increase in surface roughness $\sigma_{SR}(x)$ with thickness, x [Hensler, 1972; Cole, 1998]:

$$R_{adj} = R_0 \exp\left(-\frac{4\pi\sigma_{SR}(x)\cos\theta_i}{\lambda} \right) \qquad \text{(eq. 2.20a)}$$

Here, the adjusted reflectivity, R_{adj}, is expressed in terms of the reflectivity for a perfectly smooth film, R_0, and the surface roughness of the film is given by:

$$\sigma_{SR}(x) = \sigma_{final} \times \left(\frac{x}{x_{final}} \right)^{a} \tag{2.20b}$$

σ_{final} is the surface roughness after the film has grown to a thickness given by x_{final}. The exponent, a, has been measured previously[23] as 1/3 for similar growth conditions [Cole, 1998]. In the expression for the adjusted reflectivity, λ is the wavelength of the incident laser and the angle of incidence is given by θ_0.

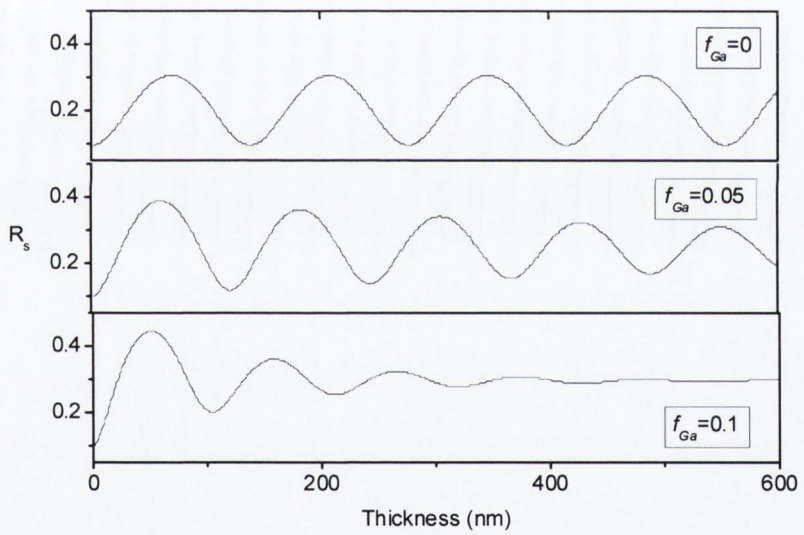

Fig. 2.8 Reflectivity at 635 nm for GaN on sapphire ($\theta_0 = 25°$) with various fractions of gallium as predicted by the Bruggemann model. From top to bottom, $f = 0$, 0.05, 0.1.

[23] The value of 1/3 was determined by fitting the reflectivity with a surface roughness value which was independently measured using atomic force microscopy. In this case, the roughness is in fact the average root-mean-square value of the amplitude of the surface structures.

3. Equipment and characterisation techniques

The basic equipment requirements for PLD have been discussed by a several [Greene et al., 1994], and this chapter serves only to summarise the relevant features of the deposition setup used for this work. The chapter is divided into three main sections; that of basic deposition equipment specifications, material preparation for ablation and film growth, and finally the specifications of the plasma and film characterisation techniques.

3.1 Basic PLD experimental setup

3.1.1 Deposition chamber and vacuum equipment

Laser ablation and film growth experiments were carried out in a high vacuum stainless steel chamber of approximately 15 litres volume. The chamber was pumped by a Pfeiffer TPH170 turbo molecular pump which was backed by a Leybold-Hereaus Trivac D8-BC rotary pump (the effective pumping speed was estimated[24] to be ~ 2/3 of the maximum rated value). The ultimate vacuum which could be obtained in the deposition chamber was 2×10-6 mbar after ~ 8 hours pumping (without baking). Two pressure gauges were used to determine the background gas pressure during deposition; a Hastings HPM-2002-OBE wide range gauge measured pressures in the range 103 to 10-4 mbar (this is a dual sensor unit containing a piezoresistive direct force sensor and a thin film Pirani type sensor), whilst a Balzers cold-cathode "Penning" gauge was used to measures pressures below 10-3 mbar. The gas flow to the chamber was controlled by a Whitey needle-valve and the gate valve to the turbo pump was used to regulate the effective pumping speed of the system. Since it is almost impossible to exactly match the input and output gas throughput manually, there was a drift in the chamber pressure which was corrected regularly. This introduced an uncertainty of ~ 10 % in the pressure readings, and the

[24] This value was calculated by noting the rate at which the chamber pressure reduced from 0.1 to 0.001 mbar. In this range, the gas flow regime is molecular and H_2O desorption from the inner chamber walls has not yet become significant. In this regime, the pressure varies with time (t) as $exp(-Qt/V)$. Thus, if the volume (V) can be approximated, the flow rate, Q, can be estimated (from the Pfeiffer turbopump instruction manual).

specifications of the OBE dual sensor device quoted an accuracy ± 15 % for pressures in the range 10-3- 1 mbar.

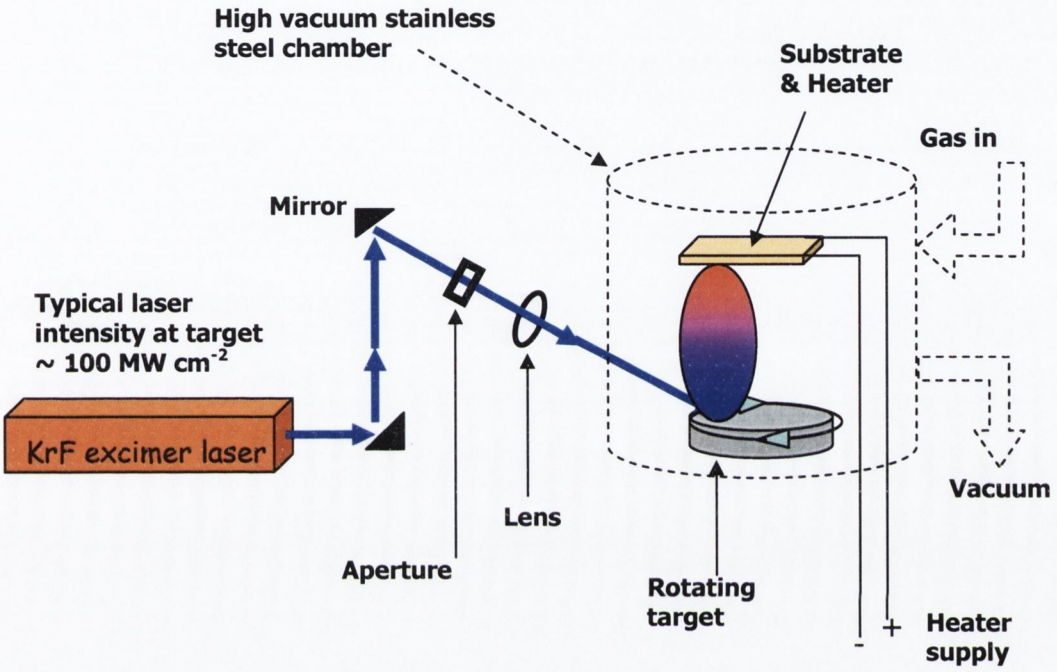

Fig. 3.1 Schematic of the basic PLD experimental setup (see text for details).

3.1.2 Laser specifications and beam delivery

A Lambda Physik MSC ENG102 KrF excimer laser emitting a UV laser pulse (λ=248 nm) with a full width at half maximum (FWHM) of 26 ns was used throughout the work. The delivery of the laser beam to the target was facilitated by two dielectric mirrors, a convex lens (f=30 cm) and view port (all fused silica, Suprasil II). The apparatus was reconfigured to prevent spillage of molten Ga by delivering the laser beam from above the chamber, at an angle of 45 ° to the normal of the horizontal target surface. The average energy per pulse was measured using a Scientech thermopile Joulemeter, which was calibrated against a known electrical power input yielding a sensitivity of 96 mV/W (the thermopile absorber disc absorbance was ~ 0.96). Taking into account the losses at the various optical components and at an aperture which was used to select a homogeneous portion of the laser beam, the maximum energy per pulse which could be

obtained at the target was 140 mJ. There are a number of aspects of the fluence measurement which contribute to a relatively high associated error, including spot size resolution (~0.2 mm in each dimension), and shot-to-shot variation in pulse energy. The total error in fluence measurement was typically 30 % and conservatively set at 40 % when using liquid targets due to the variation in the molten metal meniscus height.

3.1.3 Substrate heaters and temperature measurement

The heating elements used for all deposition experiments were SiN coated resistive heating plates, supplied by Kyocera. Substrates were attached to the heaters using conducting silver composite and the temperature measured using an Ultimax UX-20 optical pyrometer (see figure 3.2).

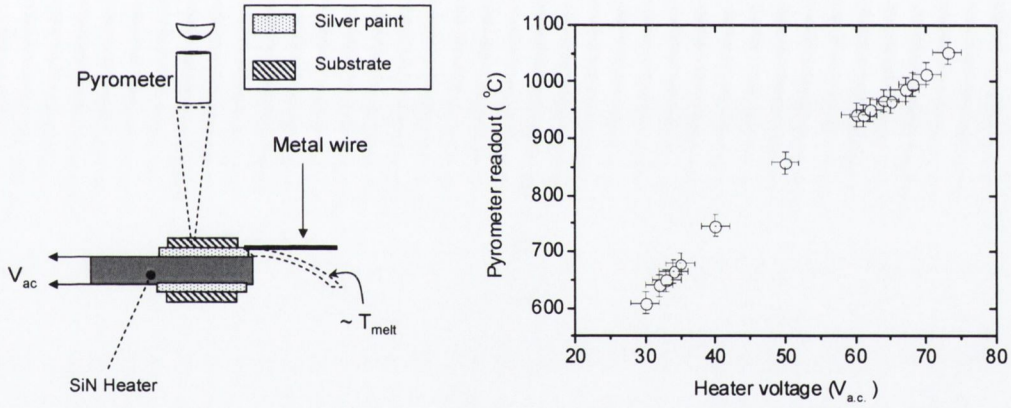

Fig. 3.2 Temperature calibration for SiN heaters. The schematic on the left illustrates the configuration of the heaters and Si substrates indicating how the high purity metal drops once the melting temperature (T_{melt}) is reached. The the calibration curve (temperature vs heater voltage) is plotted on the right.

This device incorporates a Si detector sampling at a wavelength of 1 μm and is rated for measuring surface temperatures in the range 600 °C to 3000 °C. Since sapphire is transparent at the sampling wavelength[25], Si substrates were employed for substrate

[25] An uncertainty exists regarding the object position when using a substrate which is transparent to the sampling wavelength, since it is unclear as to whether it is the substrate or heater surface which is being imaged.

temperature calibration (the calibration was carried out at temperatures in excess of ~ 700 °C, in which case it was assumed that any native oxide layer had been removed [Watanabe et al., 1997]). The temperature readout was compared with the melting points of high purity Al, Ag and Cu wires which were fixed horizontally to the heater edge with thermal conductive paint (the wires subsequently dropped upon melting). The accuracy of temperature control was about ±10 °C; the variation primarily due to the heater voltage step size (~ 1V). Taking into account the non-uniformities of the temperature distribution over the heater area surface, it is likely that the substrate temperature measurement accuracy may be as poor as ± 20 °C.

3.2 Deposition requirements: targets, background gas and substrates

3.2.1 Target choice and preparation

3.2.1.1 GaN target preparation

Before pressing into pellet form and sintering to improve mechanical strength, GaN powder (99.99 % purity) was ground manually for 1 hour in a small quantity of isopropyl alcohol, to reduce the powder mesh (grain) size[26] [Hampshire, 1986]. The targets were then hydraulically pressed at 250 bar before sintering for 12 hours at 700 °C in 1 bar of N_2 (which was the maximum gas pressure tolerance of the sintering facility) to promote densification. Ideally, the powders should be calcinated to remove volatile impurities (H_2O, oxides), but temperatures in excess of 1000 °C are required to remove oxides from group III nitride powders [Slack and McNelly, 1976], which would require a N_2 pressure in the sintering tube of ~ 10 bar to prevent decomposition (see fig. 1.7). It was noted that sintering at 800 °C and higher temperatures in 1 bar N_2 resulted in gallium droplets on the surface of the target. After the final sinter, the target volume was measured using callipers rather than via liquid displacement measurement (which would be unsuitable because of the porous nature of the target). The density of the GaN target was calculated to be 3.3 g cm^{-3}, which is just over 50% of the theoretical value (6.15 g cm^{-3}).

[26] Grinding (or "milling") has been shown to increase target density upon pressing, though the maximum achievable density by hydraulic pressing is in any case limited to ~ 60 % of the single crystal theoretical value [Hampshire, 1986].

3.2.1.2 Gallium target preparation

Gallium metal (99.99999 % purity) was supplied in shot form (pellets with a diameter of a few mm), and was melted in a polycrystalline fused silica cup. The cup of gallium was then solidified on a water-cooled metal plate before being placed on a target holder (316Ti stainless steel), in the deposition chamber. Care was taken to cool the targets slowly to obtain a flat surface (recall the problems associated with supercooling of Ga, section 1.1.1). Before the main film deposition run, the rotating targets were ablated with ~ 500 shots to remove any surface oxide layers. During this pre-growth stage, the substrate was moved out of the deposition plume to avoid film contamination.

3.2.2 N_2 as a background gas

The bulk of the work described in this thesis relates to deposition in molecular nitrogen. The use of N_2 as a background gas has a number of advantages over other environments; it is relatively inexpensive, non-toxic and commercially available to 99.9999% purity. While oxygen-free nitrogen (99.999% purity) was used for deposition in an N_2 background, a higher grade (99.9999%) was used in conjunction with the HCPEE plasma source (section 3.3). Although the gas pressure was kept constant to within the 15 % variation outlined in section 3.1.1, a small N_2 flow was maintained throughout the deposition run.

3.2.3 Substrates

The most widely used substrate in GaN thin film growth is sapphire (Al_2O_3) because it has a hexagonal structure (like GaN), is stable well above GaN film growth temperatures and in aggressive environments, and is of relatively low cost compared with better lattice-matched substrates such as SiC. The lattice and thermal parameters of sapphire (Al_2O_3), as well as the lattice mismatch with GaN, are listed in table 3.1. (000*l*) or *c*-axis sapphire (5 mm ×5 mm ×0.5 mm, ± 0.02 mm tolerance), was used for most of the growth runs with Si and GaAs used occasionally. For reflectivity measurements, 1-side polished sapphire was used to avoid reflections from the backside of the substrate.

	Al_2O_3	Units
Lattice parameter (*a, c*)	4.77, 13.04	Å
Thermal expansion (*a, c*)	7.5, 8.5	$\times 10^{-6}$ K^{-1}
GaN lattice mismatch	16[a]	%

Table 3.1 Lattice parameters and thermal expansion for sapphire (Al_2O_3). Also included is the lattice mismatch with GaN in the basal plane (from [Strite and Morkoc, 1992]. The mismatch with Al_2O_3 is for a 30° in-plane rotation of the film with respect to the substrate and was determined using the approach outlined in [Nakamura and Fasol, 1997][a].

Before being fixed to the heater with a conductive silver paste, the substrates were degreased in acetone and ethanol before being dried under a N_2 flow. For high temperature film growth, the substrates were out-gassed at ~ 500 °C for 20 minutes before each deposition run.

3.3 Plasma sources

A number of discharge devices were implemented in the deposition setup to test their suitability for plasma-assisted PLD of GaN. In this section, the device dimensions and material specifications are given, with a more in-depth discussion on the operational features and plasma characteristics of the sources presented in chapter 6.

3.3.1 "Small anode" glow discharge

This simple configuration is based on an original design by Miljevic [Miljevic, 1984], which consists of a glow discharge cell mounted onto one of the flanges of the main deposition chamber (see figure 3.3). A Spellman high voltage power supply, with an adjustable current in the 0-300 mA range, was used to maintain the voltage (0-1kV) across the electrodes (the anode was grounded). A ballast resistor (~1 kΩ) with a high power rating (50 W), was also used to limit the initial surge of current as the gas breaks down.

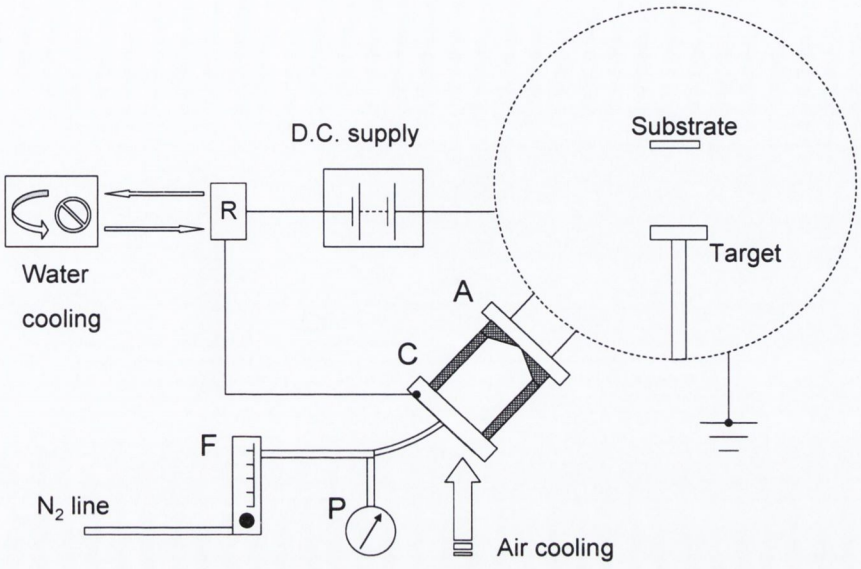

Fig. 3.3 Schematic of the final setup for the small anode discharge source. The blackened area represents the insulator used to separate the cathode (C) and anode (A). Although current supplied by the power source was internally limited, a ballast resistor (R) was also used to regulate the discharge current. The gas flow to the source was adjusted via a needle-valve flowmeter (F) and the pressure in the source was estimated using the readout from a pressure gauge (P).

The resistor was mounted on a water-cooled aluminium block using a thermally conductive paste to assist heat removal. Since the cathode becomes quite hot due to ion bombardment, it was also cooled but using a small electrical air fan.

3.3.2 Hollow cathode plasma electron emitter (HCPEE)

The hollow cathode plasma electron emitter (HCPEE, supplied by Electron Propulsion Laboratory, Inc[27]) operates by accelerating electrons (which have been produced by thermionic emission) through a gas-filled pipe to a positively biased collector positioned just in front of the exit of the pipe. The source and all electrical feed-throughs were attached horizontally to the chamber via a single DN40 (CF) flange.

[27] Electron Propulsion Laboratory, Inc., 1040 Synthes Ave., Monument, Co 80132, USA.

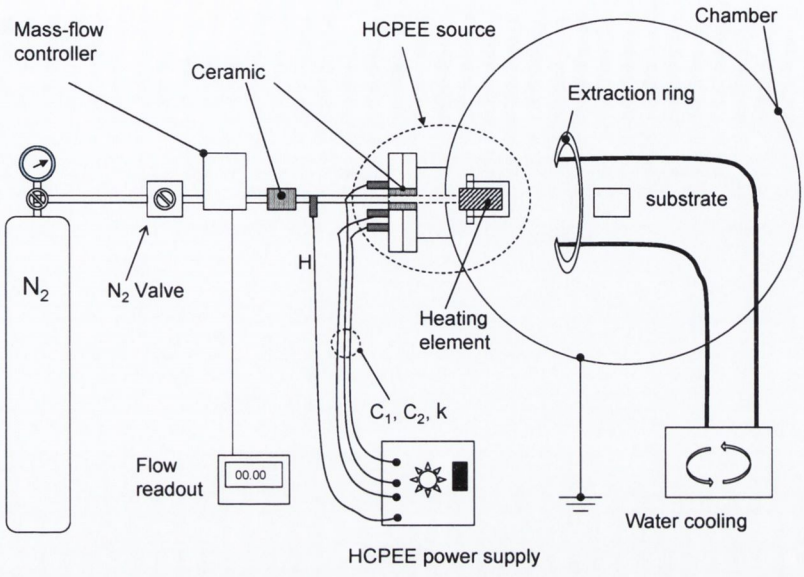

Fig. 3.4 Schematic of the HCPEE setup. The electrical connections to the source are supplied through 3 high voltage copper feed-through electrical plug connectors (labelled C_1,C_2,K), with a separate connection to the gas pipe leading to the heating element (labelled H). Further details are given in chapter 6 (section 6.4).

The voltage and current requirements for this device are automatically controlled by an external power supply which has two operational settings; a pre-ignition "outgas" mode (to remove water vapour which might corrode the heating element) and the main high current "run" mode. The ion-electron emission characteristics can be modified by varying the gas flow rate (measured using a STEC SEC 4400 digital mass-flow controller) to the source or alternatively, by implementing a second biased extraction electrode (in this case, a grounded water cooled stainless steel circular pipe) down stream from the plasma jet (figure 3.4).

3.3.3 Pulsed discharge

A pulsed discharge, synchronised with the laser produced plasma was established by incorporating a charged ring electrode (diameter ~ 7 cm), placed between the target and substrate, in the deposition setup (figure 3.5). The ring was connected in parallel with a 0.47 μF capacitor, with one terminal grounded, which discharged through the deposition

environment as the resistance to ground was reduced by the laser produced plasma. The discharge pulse was monitored noting the voltage drop across a small resistance (0.3 Ω) in series with the capacitor. The circuit was completely encased in a grounded shielding and the ring was charged using a Spellman high voltage, current-limited electrical power source.

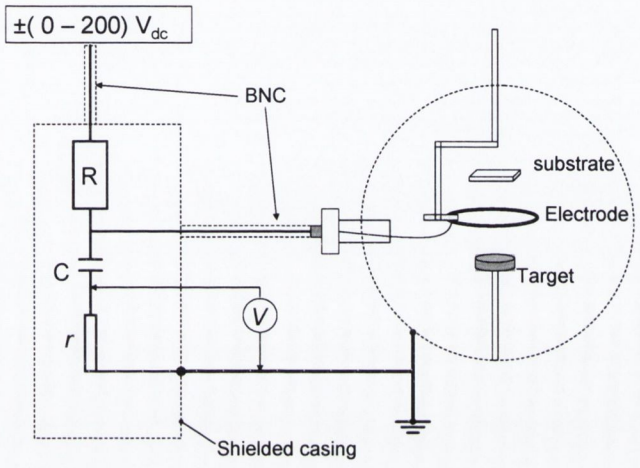

Fig. 3.5 Pulsed discharge setup. The limiting resistor, *R*, was 10 kΩ, while a capacitor, C=0.47 μF, was used to maintain the charge on the ring. A low value resistor, *r* (0.3 Ω), was used to determine the discharge current.

3.4 Plasma and film growth characterisation techniques

3.4.1 Langmuir ion probe

3.4.1.1 Pulsed (Koopman) circuit

A simple RC "Koopman" [Koopman, 1971] circuit was used to monitor the pulsed current characteristics of the laser produced plasma (figure 3.6a). Two types of probe were used; a wire probe which was typically 4 mm long and 0.2 mm in diameter, and a "flat" probe i.e. the exposed face of an electrode, typically 1 mm in diameter. The probe was connected to the response circuit using coaxial cable with a grounded outer cladding, and a double-ended BNC connector feed through. The load resistor was varied according to the amount of charge collected by the probe; for high currents, the resistor was

decreased to satisfy the condition $V_{max} << V_{bias}$, where V_{max} was the peak voltage dropped across the load resistor and V_{bias} was the bias voltage on the probe. The acquisition was triggered by the laser pre-trigger output, which is generated 1.56 μs before laser emission for the EMG MSC 102 excimer (see appendix IIIa).

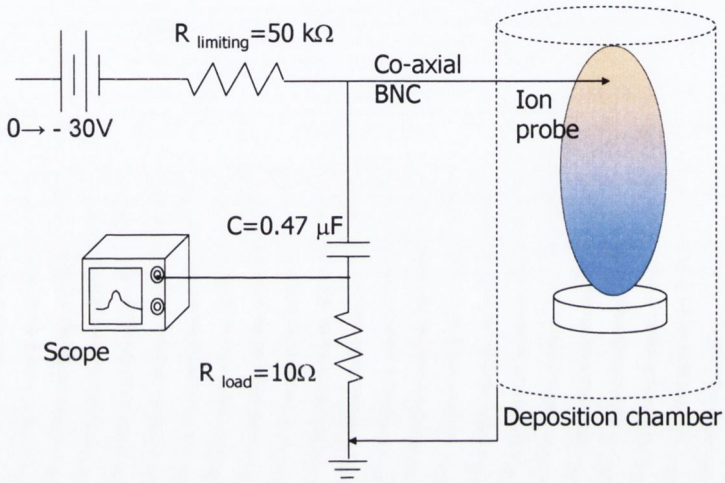

Fig. 3.6 Schematic of pulsed response circuit used in conjunction with the ion probe.

3.4.1.2 Smartprobe system

For characterisation of the small anode and HCPEE plasma sources, a device known as Smartprobe was used in conjunction with software supplied by *Scientific Systems*. This device acquires current voltage (I-V) characteristics for the plasma by automatically sweeping the voltage over a user defined range. Ion and electron densities as well as ion temperatures are easily and quickly determined using this system, though it is at a test stage as regards use with laser produced plasmas.

3.4.2 Reflectivity setup

A simple reflectivity technique was employed to monitor the film growth rate during the deposition process and was also used to calculate the refractive index of the film at the wavelength of the probe laser (see section 2.3.2 for theory details).

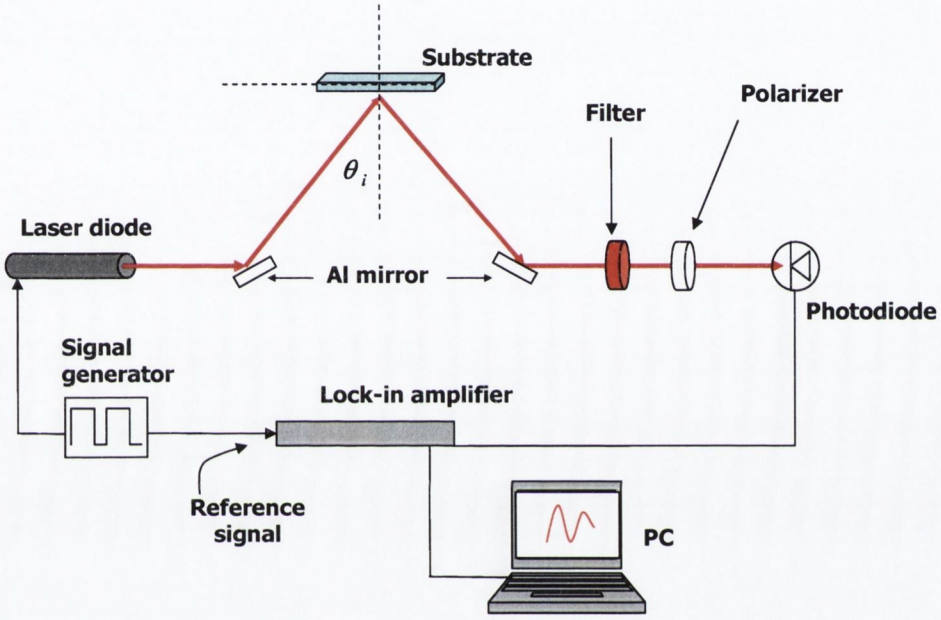

Fig. 3.7 Schematic of reflectivity setup for monitoring thin film growth. The angle of incidence was 25°. To avoid absorption by vapour deposits, the chamber view ports were protected by glass slides which were changed after each deposition.

The probe laser diode (λ_0=635 nm, FWHM~ 10 nm), supplied by Coherent, was modulated at 12 kHz using an external TTL signal (V_{peak} ~3V) generated using a simple 555 timer circuit. A reference signal was also sent to an EG&G 5101 lock-in amplifier (see figure 3.7). The laser spot size on the substrate/film had a diameter of about 0.5 mm and the average light intensity at the substrate surface was ~ 0.2 mW. A large area (100 mm^2) Si photodiode, covered with a narrow band-pass filter (λ_0=635 nm) to limit the detection of ambient light, was used to detect the reflected beam. The signal was sampled

at the modulation frequency of the probe laser by the lock-in amplifier and acquired by a pc via an ADC card.

Care was taken to ensure that the substrate was fixed in the horizontal plane, and the angle of incidence was determined to be 26° ± 3°. The incident laser beam was polarized perpendicular to the plane of incidence (i.e. s-polarised) using dichroic sheets mounted on fine control rotating component holders (the polarisation axis of the sheets was checked using a calcite "Glan-Air" polarizer). Finally, the optical losses of the system due to reflection and absorption at the various optical components were measured, and the reflectivity calibrated with silicon and sapphire samples whose optical constants are well characterised at this wavelength [Lide, 1998].

3.5 Post growth film characterisation

3.5.1 X-ray diffraction (XRD)

3.5.1.1 Diffractometer specifications

The primary post-growth film characterisation technique used in this work was XRD, with the diffraction measurements being carried out using a Siemens Diffrac 500 diffractometer. This device can operate in the θ-2θ and *w* (rocking-curve) modes, and the minimum goniometer step size is 0.002° and 0.001° for each of these two modes, respectively. The accelerating tube in the diffractometer was a Kristalloflex 710 model, which generated Cu $K_{\alpha 1}$ and $K_{\alpha 2}$ radiation (the effective wavelength of the X-ray source was 1.541845 Å [ICDD]). Low intensity Cu K_{β} radiation is also generated as are W (L series) lines, over time, as sputtered material from the tungsten filament (cathode) builds up on the anode. Both the Cu K_{β} and W L lines can be absorbed by a Ni filter (λ_{cutoff} =1.488 Å), placed in front of the detector, but this tends to reduce the count rate considerably. The angular resolution of the diffractometer in the standard slit configuration, (recommended for powder or polycrystalline thin film samples), was 0.15°.

3.4.1.2 Diffraction analysis

The majority of XRD measurements were carried out in the θ-2θ mode, over the 2θ range (30° to 45°). Diffraction peaks corresponding to the GaN (0002), $(10\bar{1}0)$ and $(11\bar{2}0)$ plane faces can be observed in this range (table 3.2), which indicates whether the lattice planes are aligned parallel, perpendicular or diagonally (or in a combination of directions) with respect to the c-axis sapphire substrate (a peak corresponding to the sapphire {000*l*} family of planes is also found in this range). Note that these planes are given in 4-coordinate Miller index notation (*h*, *k*, -(*h*+*k*), *l*), corresponding to the hexagonal crystal structure. The plane spacing d_{hkl}, and diffraction angle[28], θ_B, are related through the Bragg condition for constructive interference of X-rays by planes of atoms:

$$2d_{hkl}\sin\theta_B = n\lambda_X \qquad \text{(eq. 3.1)}$$

Here, λ_X is the wavelength of the incident X-radiation and n (=1,2,..) denotes the diffraction order. The plane spacing, d_{hex} and d_{orth}, for hexagonal (e.g. GaN, sapphire) and orthorhombic (e.g. Ga) crystal structures, respectively, are given by:

$$\frac{1}{d_{hex}^2} = \frac{4}{3}\frac{\left(h^2+hk+k^2\right)}{a^2} + \frac{l^2}{c^2} \qquad \frac{1}{d_{orth}^2} = \frac{h^2}{a^2} + \frac{k^2}{b^2} + \frac{l^2}{c^2} \qquad \text{(eq. 3.2)}$$

In the above expressions, *a, b* and *c* are the lattice parameters along the three orthogonal axes with the *c* axis conventionally assigned as being perpendicular to the sample plane. The expected 2θ positions of a number of relevant peaks for Cu K_α diffraction of GaN, Ga and sapphire (Al_2O_3) as listed by the [ICDD], are given in table 3.2. Incidentally, while the relative diffraction intensities[29] for randomly distributed powder diffractions of these materials are widely available [ICDD], similar relations for preferential growth (e.g. in thin film growth on a suitable substrate) are not. Such intensity distributions require

[28] By convention, the incident angle θ is defined as the angle in the plane of incidence between the incident beam and the surface plane, rather than the surface normal (as in visible optics).

[29] The diffraction intensity is described by assigning an atomic scattering factor and crystalline structure factor to the material under inspection. The former quantity accounts for scattering by electrons in individual atoms, while the latter accounts for intensity contributions due to the symmetry of the lattice. For a detailed discussion, see chapter 2 [Kittel, 1996].

extensive computation (p.30, [Kittel, 1996]), and were not undertaken for this work. Therefore, no quantitative analysis of the concentration of the various crystalline components will be inferred from XRD measurements.

Material	h	k	l	2□
GaN	1	0	0	32.45
GaN	0	0	2	34.65
GaN	1	0	1	36.92
Ga	1	1	1	30.24
Ga	1	1	3	45.34
Ga	2	0	0	39.89
Al_2O_3	0	0	6	41.68

Table 3.2 Relevant first order 2θ peak positions for GaN, Ga and sapphire (Al_2O_3).

The crystalline quality of the film can be related to the full-width at half-maximum of the diffraction peaks (Δ_{film}), measured in the θ-2θ mode, using the Scherrer relation ([Cullity and Stock, 2001],pp167-170):

$$\tau = \frac{\lambda_X}{\Delta_{film} \times \cos\theta_B} \qquad \text{(eq. 3.3)}$$

Here, τ is the crystalline grain size corresponding to a particular set of lattice planes with associated Bragg angle = θ_B. It is important to note that measured FWHM of peaks associated with film diffraction must be corrected for noting the resolution of the diffractometer. A consistent method of obtaining accurate grain sizes is to note the FWHM of the single crystal substrate peak (Δ_{sapp}) in each measurement and the corrected FWHM of any GaN peaks (Δ_X) is then determined by the de-convolution of the two Gaussian peak profiles [Thorne et al., 1999]:

$$\Delta^2_{film} = \Delta^2_X - \Delta^2_{sapp} \qquad \text{(eq. 3.4)}$$

The uncertainty[30] associated with a thin film XRD measurement is primarily linked to the substrate alignment with respect to the goniometer axis. Therefore, a short range scan to confirm the position of the substrate peak (as a guide to the accuracy of the alignment) was carried out before proceeding with main measurement.

3.4.2 Surface characterisation

A number of characterisation techniques were used to characterise the surface properties of the films after deposition. Initially, the films were studied under an optical microscope, which provided a simple method of identifying the macroscopic surface quality of films on a sub mm scale and was particularly useful for comparing the droplet or particulate concentrations between samples.

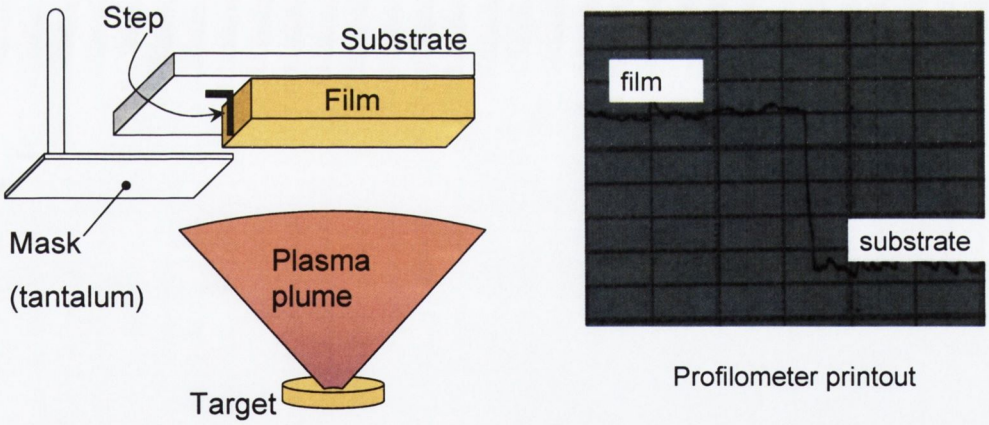

Figure 3.9 Schematic of masking setup for film thickness measurements (left). The height difference between the film and substrate was measured using a surface profilometer. The profile on the right shows a scanned image of a profilometer readout. For this particular measurement, the vertical setting on the profilometer was 0.2 μm per division which yielded a step height of (0.90±0.05) μm (the thickness measured by reflectivity for this film was 1.02 μm).

[30] The error varies with angle as $\cos^2\theta/\sin\theta$ ([Cullity and Stock, 2001]p.366).

The second technique employed to characterise the surface structure of films was surface profilometry. This technique was primarily used to determine the thickness of films deposited using a mask to prevent deposition on part of the substrate. The mask consisted of a high purity tantalum[31] strip which was attached to the substrate heater and positioned such that it lay just above the surface of one end of the substrate. The profilometer measured the height of the step created by this masking process, and the measurements were compared with thickness values determined by optical reflectivity.

Finally, some of the film and target surfaces were imaged using a Hitachi S-3500N scanning electron microscope (SEM) at the Centre for Microscopy Analysis, TCD. The SEM was operated in variable pressure (VP) mode, which allows analysis of non-conducting samples without having to apply a conducting coating (the resolution in this mode was ~ 10 nm).

3.4.3 Compositional analysis: EDAX

The high energy electron beam produced by the Hitachi S-3500N apparatus used in SEM imaging allowed Energy dispersive Analysis by X-rays (EDAX) to be carried out on some of the targets and films. The sampling depth for EDAX depends on the composition of the material under investigation (and of course the electron acceleration voltage). Generally speaking, the X-ray penetration depth (and thus sampling depth) is less for heavier (high Z) elements. In any case, the depth is no more than a few microns, so the technique is essentially one of surface characterisation when characterising with PLD targets. However, the relatively high nitrogen background pressure associated with VP mode and low X-ray yield for lighter elements renders the technique unsuitable for quantitative analysis of the nitrogen component in nitride films. Accurate quantitative EDAX analysis of thin films is limited by a certain substrate contribution, since the sampling volume is typically a few μm^3 (the X-ray absorption depth is greater than 1 μm for most crystalline solids; see for example appendix 8 [Cullity and Stock, 2001]).

[31] To limit contamination of the film with material sputtered from the mask by the energetic plume, a stable metal or ceramic mask should be used. Tantalum is suited to this environment as it has a comparatively high ionisation threshold, is chemically very stable and has a melting temperature > 3000 °C.

The high energy electron beam produced by the Hitachi S-3500N apparatus used in SEM imaging allowed Energy dispersive Analysis by X-rays (EDAX) to be carried out on some of the targets and films. The sampling depth for EDAX depends on the composition of the material under investigation (and of course the electron acceleration voltage). Generally speaking, the X-ray penetration depth (and thus sampling depth) is less for heavier (high Z) elements. In any case, the depth is no more than a few microns, so the technique is essentially one of surface characterisation when characterising with PLD targets. However, the relatively high nitrogen background pressure associated with VP mode and low X-ray yield for lighter elements renders the technique unsuitable for quantitative analysis of the nitrogen component in nitride films. Accurate quantitative EDAX analysis of thin films is limited by a certain substrate contribution, since the sampling volume is typically a few μm^3 (the X-ray absorption depth is greater than 1 μm for most crystalline solids; see for example appendix 8 [Cullity and Stock, 2001]).

4. PLD of GaN using a ceramic GaN target

4.1 Introduction

In recent years, PLD has emerged as a suitable film growth technique for the preparation of wide direct bandgap semiconductors such as GaN and AlN [Feiler et al., 1997; Vispute et al., 1999], which have become extremely important materials for display lighting and high frequency electronic applications [Jain et al., 2000]. An attractive feature of the PLD technique is the apparently high degree of stoichiometric transfer form target to film, thus making it potentially suitable for group-III nitride growth, where the high melting temperature has limited the use of other crystallisation techniques which grow from the melt [Porowski and Grzegory, 1997]. However, decomposition and metallization of the target surface has been reported in ablation of AlN [Hirayama et al., 2001; Ristoscu et al., 2003] and GaN [Kelly et al., 1996; Chu et al., 2001] samples using ns laser pulses. While a number of groups have studied the plume composition in AlN target ablation using spectroscopy [di Palma et al., 1995; McKiernan and Mosnier, 2002], the extent of the decomposition or target stoichiometry after ablation has not been reported (though the nitrogen fraction in ns laser ablation plumes of AlN targets is estimated to be as high as 0.8 [di Palma et al., 1995]). The effect of such non-stoichiometric ablation on film properties been not been reported either, although it seems clear that high quality GaN growth by PLD requires a nitriding background (films grown in high vacuum or UHV have low growth rates, are heavily n-doped and are of comparatively poor structural quality [Cole and Lunney, 1997; Feiler et al., 1997]).

Since control of the film stoichiometry is essential in order to obtain single crystal growth and for electrical doping, there is a need i) to establish a means of quantifying the film stoichiometry during growth and ii) to identify the deposition conditions leading to full stoichiometric growth. This work is concerned with identifying such deposition requirements using an electrical probe to map the dynamics of the ionic component of the plume and optical reflectometry to monitor the growth rate and optical properties of the thin films during growth.

4.2 Experimental approach

As indicated in the thesis introduction, the range of background gas pressure and fluence under investigation is based on previous observations and reports of PLD of GaN using GaN targets. In general, the fluence used for GaN film growth with the nitride (GaN) target has been considerably less than that used with the metal (Ga) target (next chapter). However, there seems to be a minimum fluence requirement of ~ 2 J cm^{-2} [Cole and Lunney, 1997; Feiler et al., 1997; Vispute et al., 1999], which is well above the previously reported ablation (and metallization) threshold for GaN of ~ 400 mJ cm^{-2} [Kelly et al., 1996; Tavernier and Clarke, 2001]. Therefore, the ablation characteristics at 1 J cm^{-2} and 2.5 cm^{-2} were investigated, to deduce whether there is a considerable change with fluence in the ablation yield or plume energy. With regard to the background gas pressure, a survey of the literature reveals that growth with the ceramic target in N_2 is typically carried out at 0.01-0.1 mbar (the pressure is in general an order or two of magnitude lower when using more reactive environments such as NH_3, see for example [Cole and Lunney, 1997; Feiler et al., 1997; Huang et al., 1999; Vispute et al., 1999]).

Ablation and deposition experiments were performed using a sintered, pressed GaN powder (99.99%) pellet which was ablated with 248 nm, 26 ns laser pulses (the target preparation method is discussed in section 3.2.1). The laser spot size at the target surface was (4×1) mm^2 and the targets were ablated with approximately 6000 shots while being rotated at ~ 50 rpm. Experiments were carried out in three N_2 background gas pressures; 10^{-4} mbar (high vacuum), 0.05 mbar and 0.1 mbar, and at a fixed target-substrate distance of 4 cm. Mass loss was measured using an AX26 Metler Toledo microbalance, which had a measurement accuracy of 2 μg. A negatively biased (-30 V) flat (exposed probe area = 4 mm^2) Langmuir ion probe was used to monitor the ion characteristics of the ablation plume along the target normal, while the reflectivity of the films was measured at 635 nm ($\theta_i = 25°$) using the reflectivity setup outlined in section 3.3.2.

4.3 Mass loss measurements and model comparison

Before discussing the mass loss data, it is worth considering some observations relating to the target properties after ablation. It was noted that the ablated region of the surface had a metallic-greyish appearance, which is presumably a gallium-rich layer. The scanning electron microscope (SEM) images of the target surface before and after ablation presented in figure 4.1 show quite an amount of surface structure and micron size particulates, which invariably leads to particulate accumulation in the films. The shape of the particulates in the ablated target is noticeably different to those of the fresh target, in that they appear spherical, rather like those observed in hydrodynamic sputtering of metal targets [Kelly and Miotello, 1994].

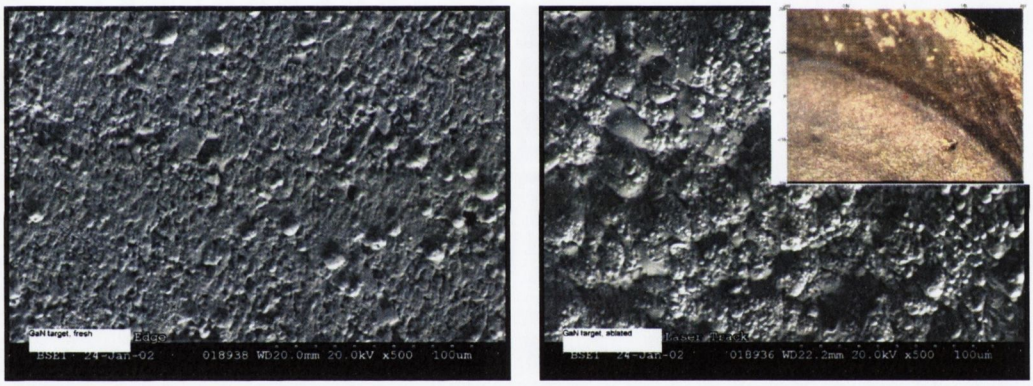

Fig. 4.1 SEM images of a pressed, sintered GaN target (left) and a target ablated with ~ 10000 shots (right). The imaged area in both scans was approximately (200 μm × 250 μm). Also included (inset, right) is an image of the edge of the laser track on the target showing the ablated (grey/ metallic region).

Figure 4.2 shows the mass loss *vs* fluence for GaN target ablation indicating an ablation threshold of less than 100 mJ cm^{-2}. Also included is the mass loss predicted by the model, using a surface reflectivity of 0 (dashed line) and 0.3 (dotted line), the latter being the maximum value of reflectivity for single crystal GaN at 45° incidence (see figure 2.5). There is significant discrepancy between the measured data and the model even when a value of zero is assigned to the surface reflectivity. Although the photoabsorption term drastically affects the predicted mass loss once the threshold is significantly exceeded

(compare solid line with dashed/dotted lines), it has little effect on the value of the threshold itself (this is because the vapour density is still comparatively low).

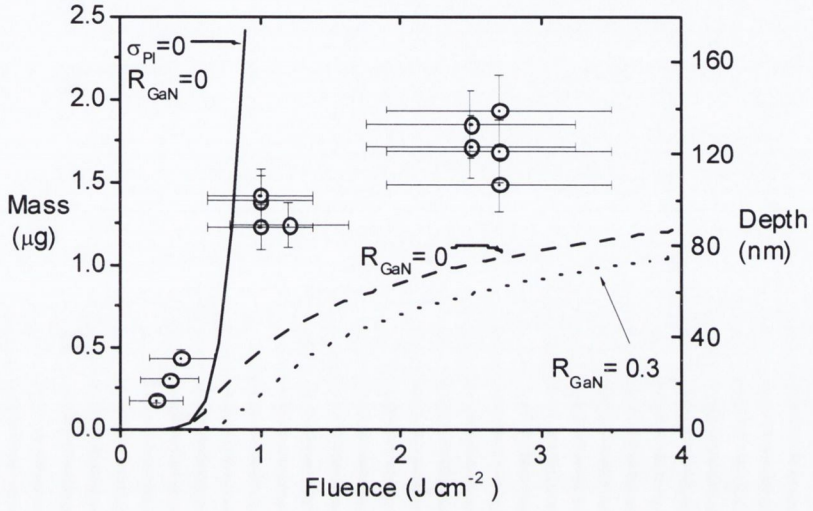

Fig.4.2 Mass loss (scatter points, left axis) for ns ablation of a GaN target (spot size = (4×1) mm^2). Also included is the mass loss predicted by the model for reflectivity of 0.3 (dotted line) and zero (dashed line) using a value of 10^{-17} cm^2 for the photo-absorption cross-section. The mass loss predicted by the model ignoring plasma absorption and using a reflectivity of zero is represented by the solid line. The corresponding ablation depth determined from the measured mass loss and using a density of 3.3 g cm^{-3} (section 3.2.1.1) is given by the right-hand axis.

Other sources of error might include the thermal conductivity of the target (a value of 0.3 W cm K^{-1} was used noting the results for pressed InN powder pellets [Krukowski et al., 1998]) or the target density (3.3 g cm^{-3} was used), but both of these terms are under the square-root in the surface temperature expression (eq. 2.1) and, as such, should not account for such a considerable disagreement. It is likely that the discrepancy lies in the description of the ablation process itself. Either the evaporation rate is underestimated by Munir and Searcy's flux data (figure 1.6), or ablation is dominated by material removal processes other than thermal evaporation (e.g. exfoliational sputtering, see section 2.2.1). The latter is to be expected, especially since the targets were not sintered at temperatures high enough to reduce the void content or the defect density significantly (section 3.2.1.1). The total number of particles ablated per shot can be estimated from figure 4.2.

At 2.5 J cm^{-2}, the mass loss (1.5-2 μg) corresponds to a total of ~10^{16} GaN molecules[32] removed per shot (or ~10^{17} cm^{-2} per shot) assuming that the ablation is almost congruent. Since the surface appears Ga rich after ablation, a more likely scenario is that laser heating leads to preferential ablation of nitrogen, in which case the number of ablated particles may be several times greater than this estimate (the molar mass of Ga is ~ 2.5 times that of N_2).

4.4 Ion probe measurements

4.4.1 Vacuum expansion

The decrease in ion flux with distance is illustrated in figure 4.3. One might expect that for an expansion from a point source, the flux should fall off as $(1/d)^2$ where d is the distance to the source.

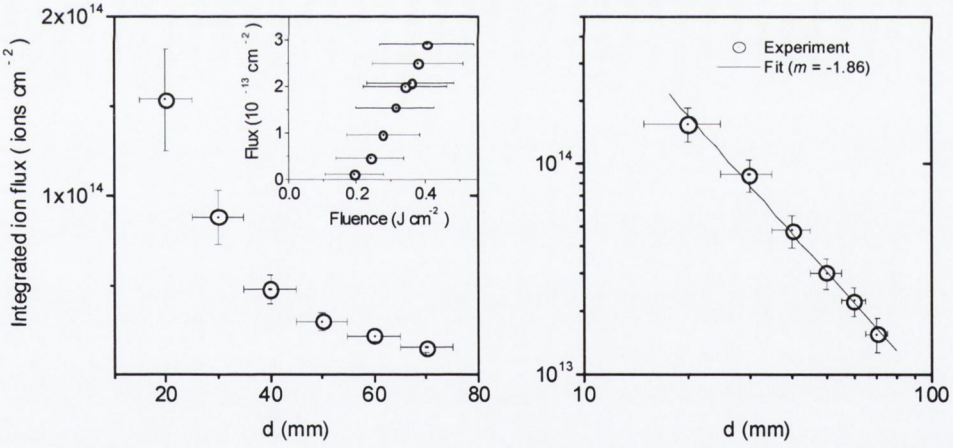

Fig. 4.3 Ion flux vs distance from the target (along the target normal) for GaN target ablation at 2.5 J cm^{-2} in vacuum (~ 10^{-5} mbar). This is the total integrated ion flux per shot, passing the probe (a log-log plot of the data is presented on the right). The integrated ion flux as a function of laser fluence is also plotted (inset, left) indicating an ionisation threshold of ~ 0.2 J cm^{-2}.

[32] The molar mass of Ga and N is 69.7 g mol^{-1} and 14.0 g mol^{-1}, respectively.

However, approximating the expansion to that of a point source is perhaps only reasonable when $d >> x_{max}$, where x_{max} is the maximum spot dimension (4 mm). In any case, a log-log plot of this data reveals that the exponent is slightly less at 1.86. Most importantly from a film growth point of view is that the integrated ion flux at the substrate position (4 cm) at is ~ 5×10^{13} cm^{-2} per shot for a fluence of 2.5 J cm^{-2}. The threshold for detection of an ion current by the probe in laser ablation of GaN targets is included as an inset in figure 4.3, indicating an ionisation threshold of less than 0.2 J cm^{-2}. The angular distribution of the integrated ion flux about both laser spot axes is presented in figure 4.4. The measured data was fitted with the Anisimov model (eq.2.3a) which yielded values of 1.8 and 2.3 for κ_A and κ_B, respectively (recall that the "κ" values are the asymptotic ratios of the orthogonal axes of the plume, see section 2.3.1 for details). The "flip-over" effect (where the plume expands more quickly about the shorter spot dimension), associated with non-circular laser spots [Anisimov et al., 1993], is evident from this plot (i.e. $\kappa_B > \kappa_A$).

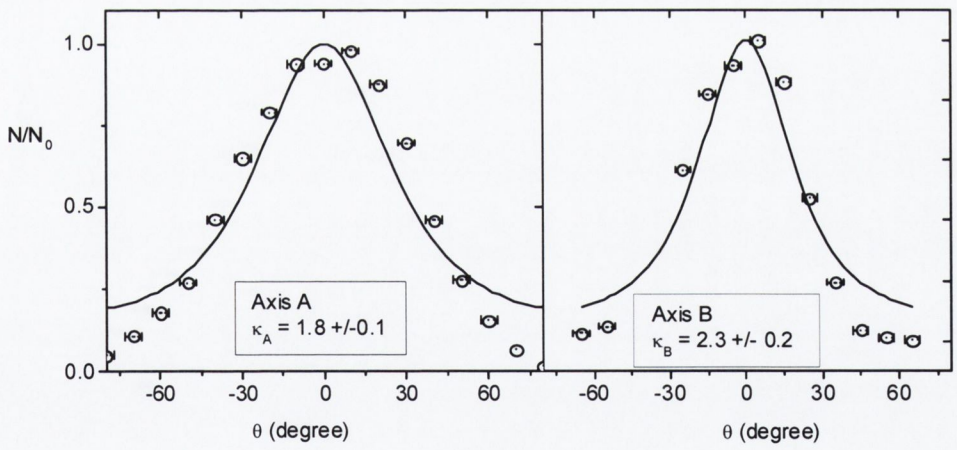

Fig. 4.4 Angular distribution of the ion flux measured 4 cm from a GaN target ablated in high vacuum at 2.5 J cm^{-2}. The data is normalised to the flux value at the normal (θ=0) position. The lines represent the fit to the measured values using equation 2.3b.

Assuming only singly charged ions were detected by the probe, the total number of ions in the plume was determined (using equation 2.3b) to be $(2 \pm 0.8) \times10^{15}$ which is

approximately (10-20) % of the total number of ablated atoms calculated in section 4.3 (though the actual value may be somewhat lower, depending on how accurate the total ablation number calculation of section 4.3 is). The variation of the ion kinetic energy for the maximum ion flux with laser fluence is presented in figure 4.5. As the fluence is increased above a few J cm^{-2}, the ion energy appears to saturate, indicating that the increased energy input maybe channelled into higher order ionisation processes, as reported previously in spectroscopic studies on laser ablation of Ga and GaN targets [McKiernan and Mosnier, 2002]. Also included is the ion energy distribution calculated from the probe signals using equation 2.12, indicating a mean energy of 10 eV and 20 eV for a fluence of 1 J cm^{-2} and 2.5 J cm^{-2}, respectively (see section 2.2.3 for details of the distribution function).

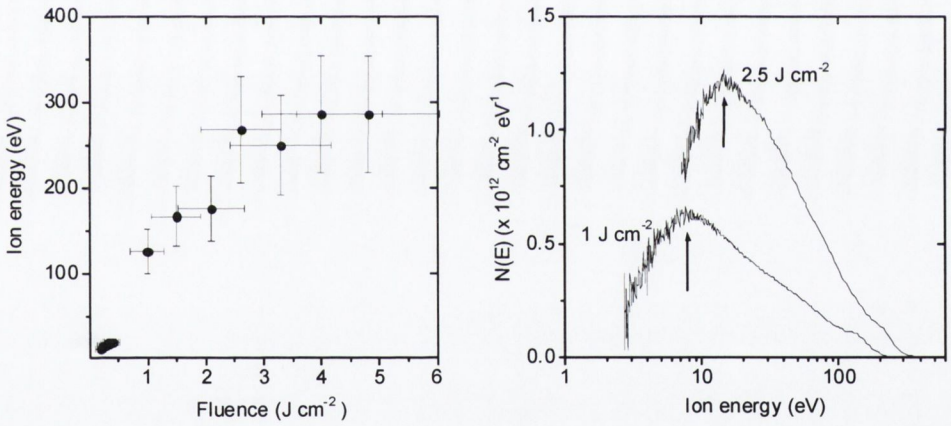

Fig. 4.5 (a) Variation of the Ga^+ ion energy (maximum ion flux) with laser fluence, for GaN target ablation in high vacuum (left). (b) Ion energy distribution, *N(E)*, calculated from TOF spectra for two of the fluences (1 and 2.5 J cm^{-2}) with arrows indicating the mean energy for the distributions.

The kinetic energy associated with the neutral component of the plasma plume has not been measured, and while a number of groups have used visible [Pronko et al., 1999] and vacuum ultra-violet [McKiernan and Mosnier, 2002] emission spectroscopy to characterise GaN laser ablation plumes, little data is available with regard to the plume dynamics associated with laser ablated GaN targets. However, in ns ablation of AlN targets [Santagata et al., 2003], the TOF of the maximum neutral flux was found to be

approximately 2.3 times greater than that of the ion flux, which corresponds to reduction in the kinetic energy by about a factor of 5.

4.4.2 Background gas measurements

Figure 4.6 illustrates the variation of the ion TOF signal with background gas (N_2) at 4 cm from the target using a fluence of 2.5 J cm^{-2}. Following the discussion in section 2.2.2.2, one expects that as the gas pressure is increased some or all of the ablated material collides with the gas resulting in an increase in the arrival time of some of the ions to the probe. This generally occurs when the mean-free path of the ablated particles in the gas is reduced to less than the target probe separation (~ cm) [Wood et al., 1998]. A "splitting" of the ion signal would also be expected corresponding to these two groups of ions. However, in figure 4.6, splitting of the ion signal is somewhat unclear and at no stage are the peaks clearly resolved. Similar behaviour has been reported for Si ablation in He, and was attributed to the low mass of the background gas particles (i.e. since m_{He}=4 a.m.u., the assumption of fixed scattering sites is somewhat unjustified).

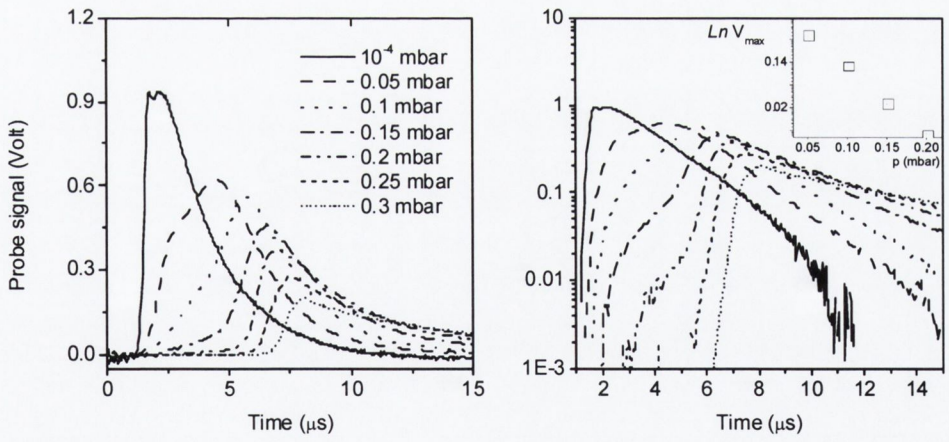

Fig. 4.6 Ion TOF signals at 4 cm for GaN target ablation in high vacuum and various background gas pressures of N_2 for a laser fluence of 2.5 J cm^{-2}. The data is also plotted on a log scale (right) to allow easier identification of the "first" peak, with the inset showing the peak reduction with pressure on a natural log scale.

Despite the uncertainty associated with the position of the first peak, the value of V_{max} at the various pressures for a fixed time (indicated by the arrow in figure 4.6) was estimated and plotted on a natural log scale (inset in figure 4.6). The slope of the plot was used to determine the scattering cross-section (section 2.2.2.1), which was calculated as 3×10^{-16} cm^2 (this is of the same order as the value estimated for the cross-sectional area of an N_2 molecule in section 1.1.5). At 0.1 mbar, this corresponds to a mean-free path for Ga ions in the background gas of:

$$\lambda_g = {}^{1}\!/_{n_g\sigma_g} = \left[2.4\times10^{15}cm^{-3}\times3\times10^{-16}cm^2\right]^{-1} \cong 1.4mm$$

The TOF signals for ablation in 0.1 mbar N_2 were then acquired at increasing distances from the target, and the distance vs TOF of the second peak in these signals is plotted in figure 4.7(a).

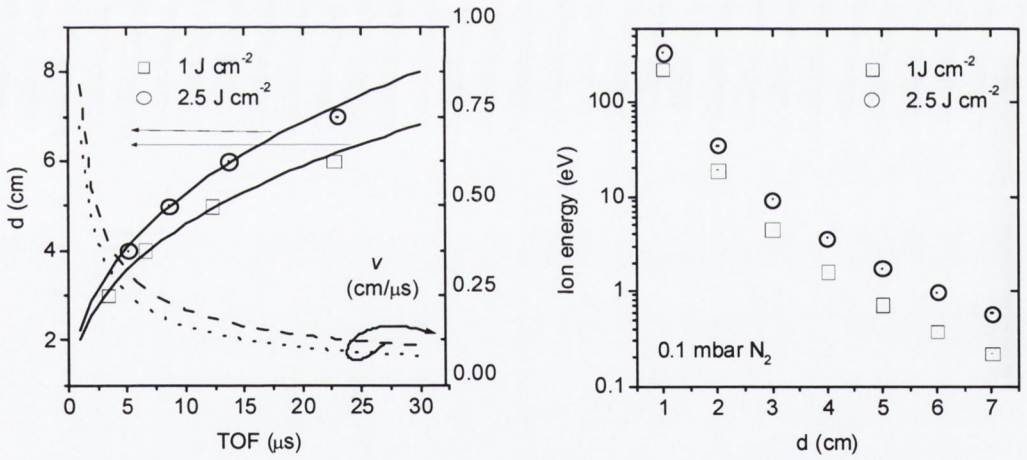

Fig. 4.7 (a) Distance *vs* time of flight (scatter points) and velocities of Ga^+ ions (maximum ion flux) in 0.1 mbar N_2 (left). The dotted and dashed lines are fits to the distance *vs* TOF data for ablation at 1 Jcm^{-2} and 2.5 J cm^{-2}, respectively. (b) Variation of the ion energy associated with the maximum ion flux with distance from the target in 0.1 mbar N_2.

From this data, the velocity profiles (dashed and dotted lines) were determined by fitting the distance vs TOF of the second peak with equation 2.6b $\left(v = \frac{dR(t)}{dt} = \eta B t^{\eta-1} \right)$. The variation in the ion kinetic energy with distance from the target, simply calculated as $\frac{1}{2} m_{ion} v^2$ (assuming only singly charged Ga ions were detected), is shown in figure 4.7(b). While the reduction in ion energy indicates that the plume has been slowed by the background gas, the extent to which this interaction has resulted in activation (i.e. excitation or dissociation) of the background gas is not immediately evident. However, it may be possible to identify the minimum energy requirements for activation by considering the nitrogen energy level diagram presented in figure 1.4 [Newman, 1997]. Although the dissociation of molecular nitrogen into ground state atomic nitrogen {N (^{4}S) + N (^{2}D)} requires 9.8 eV per molecule to break the strong triple N:N bond, there are also a number of excited states of molecular nitrogen with lower potential energies with respect to the ground state, the lowest of which is about 6 eV. In the absence of other chemical or electronic activation mechanisms, this value can be set as an absolute minimum energy requirement for activation of the background gas. Taking into consideration the data presented in this section, the region for activation would be greatly limited to within 3 cm of the target.

4.5 Film growth on unheated substrates

GaN growth on heated substrates facilitates crystallisation and promotes preferential growth along a particular direction with respect to the crystal axes of the substrate. However, the increased temperature gives rise to evaporation and reactions leading to the formation or decomposition of compounds at the substrate with the result that information regarding the type and amount of material initially deposited on the substrate can be lost. For this reason, the properties of films deposited on unheated or room temperature (RT) substrates were first studied with the aim of relating the material properties with the deposition conditions prior to any substrate heating effects

4.5.1 Overview of reflectivity data

Figures 4.8 and 4.9 show the s-polarised reflectivity for films deposited on sapphire substrates using a GaN target at 1 J cm^{-2} and 2.5 J cm^{-2}, respectively. The variation is plotted against shot number (i.e. the number of laser shots fired at the target), and in all cases the repetition rate was 5 Hz, while the target-substrate distance was maintained at 4 cm. It is interesting to note that films grown in high vacuum (10^{-5} mbar N_2) show significant damping of the reflected amplitude with increasing thickness, while for the films grown in 0.05-0.1 mbar N_2, the damping effect is barely noticeable. The high vacuum trace is typical of a poor metal or absorbing dielectric (p.757, [Born and Wolf, 1999])[33], indicating that some free metal (presumably gallium) is present in the films. The traces for growth in 0.05 mbar and 0.1 mbar N_2 show significant changes in comparison with the high vacuum case in that the oscillation amplitude remains fairly constant with thickness (except for growth at 1 J cm^{-2} in 0.05 mbar N_2). They no longer appear to be strongly absorbing at the probe laser wavelength (635 nm) indicating that the free gallium fraction in the films has been reduced significantly by using an N_2 gas pressure of ~ 0.1 mbar. The behaviour of the reflectivity trace at 1 J cm^{-2} in 0.1 mbar N_2 is somewhat puzzling, but it seems to indicate that the growth mode has changed considerably after the first 3000 or so shots. At this lower fluence and relatively high background gas pressure, the energy of the plume reaching the substrate is greatly reduced, and the film may have a considerable void fraction due to the formation of clusters and poor surface mobility in the absence of substrate heating.

[33] The imaginary component of the electrical permittivity, and thus the extinction coefficient, is strongly dependent on the electrical conductivity of the material. See for example, chapter XIV in [Born and Wolf, 1999].

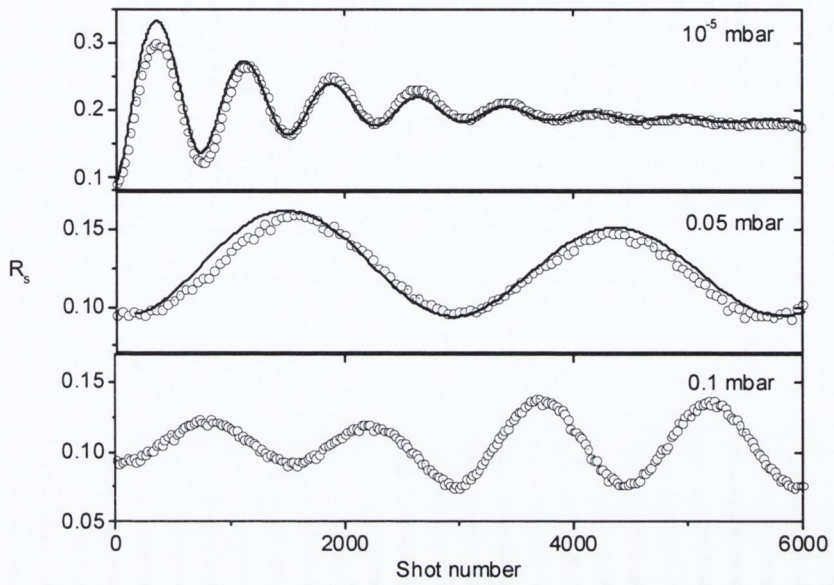

Fig. 4.8 In-situ reflectivity traces for film growth using a GaN target with a laser fluence of 1 J cm^{-2}. The measured reflectivity (circles) was fitted with the model (solid line) outlined in chapter 2. Note that the y-axis (R_s) scaling is different for each panel. The trace for 0.1 mbar (bottom) was not fitted as the growth rate appears to change dramatically after the first 3000 or so shots.

It is important to note that while films grown in N_2 show little absorption at 635 nm, as would be expected for single crystal GaN (k<0.001, table 1.1), the amplitude of oscillation suggests that the refractive index differs considerably from the values listed in table 1.1 (alternatively, see figure 1.3). The reflectivity trace for single crystal GaN would be expected to oscillate between ~ 0.1 and 0.3 (figure 2.8), whereas for these films deposited in N_2, the trace maxima are considerably less.

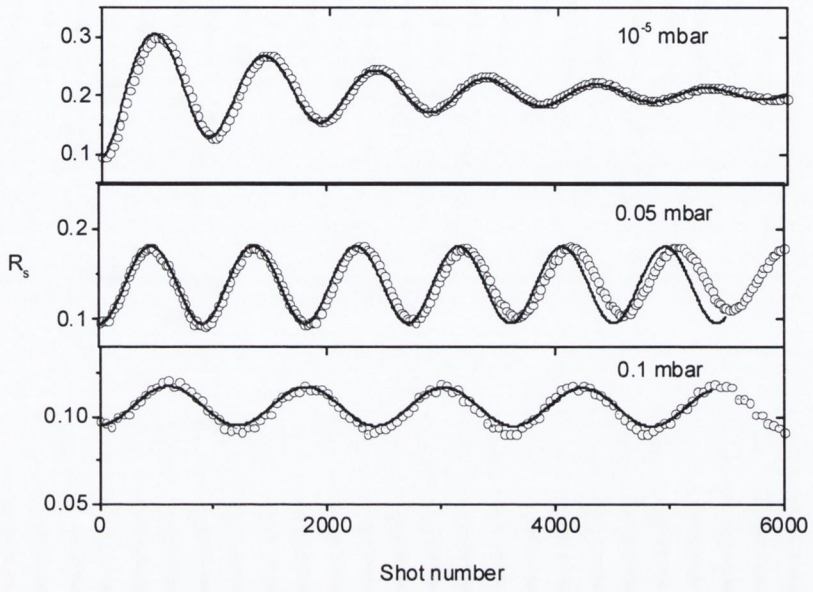

Fig. 4.9 Reflectivity signals for film growth using a GaN target with a fluence of 2.5 J cm^{-2}. As in figure 4.8, the y-axis has been varied for clarity and the range is different for each panel. Unlike growth at 1 J cm^{-2}, the gas pressure does not appear to have such a drastic effect on the oscillation period (i.e. the growth rate).

With regard to the surface roughness of the films it seems the introduction of a background gas does not appear to greatly alter the roughness values deduced from the fit to the reflectivity traces. At 1 J cm^{-2}, the reduction in roughness associated with an increase in gas pressure of 10^{-5} to 0.05 mbar was comparatively small (25 nm to 21 nm), indicating that the particulates contributing to the observed roughness are much more massive than the gas molecules and are little affected at these pressures (as seems to be the case from the SEM images in figure 4.10). Rather surprisingly, the films grown at 2.5 J cm^{-2}, with roughness values of 15 nm or less, appear to be smoother than those grown at 1 J cm^{-2}.

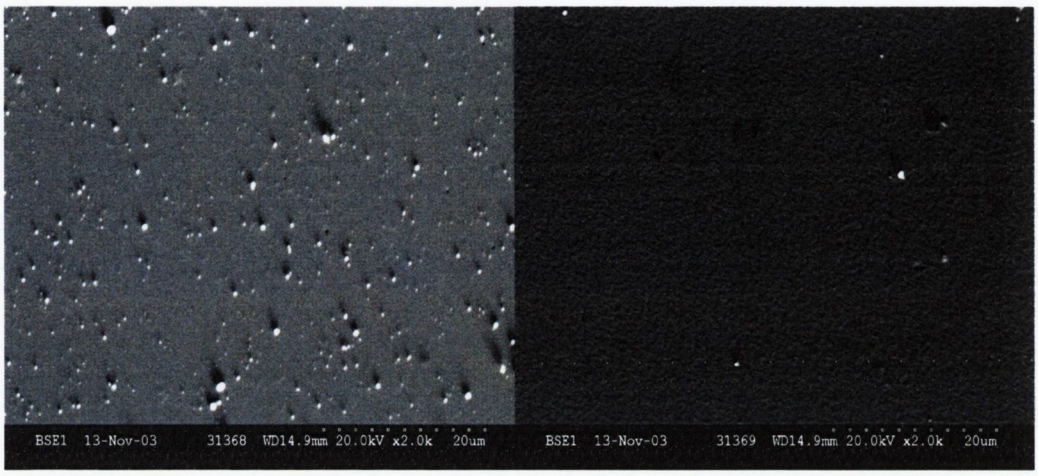

Fig. 4.10 SEM images of films grown from GaN targets in 0.05 mbar N_2 at 2.5 J cm^{-2}. The image on the left is for a film grown on an unheated substrate, while the film on the right was deposited at a substrate temperature of 750 °C. The imaged area is approximately (60×50) μm^2 (note: the darker appearance of the right hand image is purely due to the contrast setting during image acquisition).

4.5.2 Fitting the reflectivity data

The reflectivity traces in figures 4.8 and 4.9 were fitted with the model outlined in section 2.3.2.3, which allowed the *n* and *k* values for the film to be determined. It was also used to estimate the free gallium fraction in the films, using the Bruggemann analysis (2.3.2.2), assuming the permittivity of the components in the films is known. However, considering the qualitative observations of the previous section, it appears that the optical properties of the films differ considerably from single crystal GaN, indicating that the *n* and *k* values listed in table 1.1 are unsuitable input parameters for the reflectivity model. To simplify the problem somewhat, a number of assumptions will be made at this point:

i) The films comprise a mixture of two components: amorphous GaN and Ga metal. The permittivity is then determined using the Bruggemann relation for two component mixing.

ii) During deposition, any Ga in the films is in a liquid state. Correspondingly, the permittivity can be determined using the values of *n* and *k* listed in table 1.1

iii) The extinction coefficient (k) for any GaN in the film is low (≤ 0.01) at this wavelength (635 nm). This assumption simplifies the fitting procedure, as the effective value of k is then primarily determined by the Ga fraction[34].

The first assumption is not unreasonable, since it appears from X-ray diffraction analysis that the films are amorphous (figure 4.11). During deposition, any Ga is likely to be in a liquid state once the laser produced vapour condenses on the substrate (recall that the melting point is 29.8 °C). Finally, the extinction coefficient at 635 nm for any GaN in the mixture is likely to be quite low, since the bandgap for amorphous GaN is reported to be 3.9 eV [Nonomura et al., 1996] which is well above the probe laser energy of 1.95 eV (the bandgap of hexagonal (3.5 eV) and cubic (3.3 eV) GaN [Strite and Morkoc, 1992] are also well above this energy).

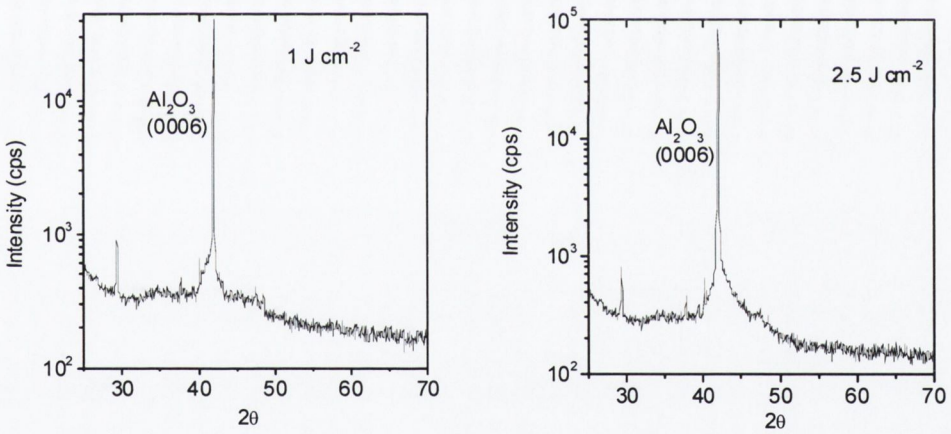

Figure 4.11 XRD scan of films grown on sapphire at room temperature. The intense peak at $2\theta = 41.65°$ is due to the sapphire substrate while the low intensity peak, observed at 29.3°, is as yet unidentified but it does not correspond to any of the known GaN or Ga phases (see table 3.2).

Table 4.1 contains the parameters determined from the fit (solid lines) to the reflectivity data in figures 4.8 and 4.9 for the various laser fluences and background gas pressures

[34] The approximation that the effective k value is primarily determined by the Ga concentration breaks down as the Ga fraction reduces to ~ 0.01 and below. In this case, the effective k value will be of the same order as the GaN k value (recall figure 2.7). Therefore, while this approximation is required, a value for the Ga concentration can only be inferred when the fraction is of the order of 0.1 or more.

investigated. For films which were not easily scratched, the thickness (and thus growth rate per shot) was confirmed by measuring the film step height with a surface profilometer (see section 3.4.2 for experimental method). In all cases, the thickness measured by the profilometer was within 15% of the value determined from reflectivity measurements. The results in table 4.1 emphasise the role played by N_2 background gas in determining both the growth rate and stoichiometry of the films. However, while a background gas pressure of ~ 0.05 N_2 is adequate to reduce the free gallium content considerably, the growth rate is greatly limited by the pressure increase when a fluence of 1 J cm^{-2} is used.

4.5.3 Deposition rates

In order to calculate the deposition rate at the substrate, the film density was required, and for these films, it was assumed that the mass density of these films, ρ_{Film}, was a weighted average of densities of Ga (ρ_{Ga}) and GaN (ρ_{GaN})[35], i.e. $\rho_{Film} = f_{Ga}\rho_{Ga} + (1 - f_{Ga})\rho_{GaN}$. The deposition flux, j_{dep}, can then be expressed in terms of the growth rate, $\delta_{film,}$, as:

$$j_{dep} = \frac{1}{1 - c_e} \times \frac{\delta_{film}\rho_{Film}N_{Av}}{M_{Film}}$$

Here, N_{Av} is Avogadro's constant and c_e is the evaporation coefficient for particles arriving at the substrate (i.e. ratio of number of particles which condense to number which are deposited). The molar mass of the film, M_{Film}, like the mass density, was assumed to be a weighted average of the molar masses of Ga and GaN using the calculated gallium fraction, f_{Ga}. The average deposition flux at 10 Hz for c_e=0 is listed in

[35] In any case, the densities of Ga and GaN are quite close, particularly if Ga is liquid (see table 1.1). Similarly, the effective molar mass of the film will only differ greatly from that of GaN when f_{Ga} is of the order of 0.1, in which case sputtering may play a significant role and the deposition flux calculation is limited by the uncertainty in the evaporation coefficient (i.e. in high vacuum).

table 4.1. (for comparison with the decomposition flux of GaN determined by Newman, see figure 1.6).

F (J cm^{-2})	p (mbar)	n_{eff}	k_{eff}	n_{GaN}	δ_{film} (nm/shot)	$j_{dep}\times10^{15}$ (cm^{-2} s^{-1})	f_{Ga}
1	10^{-5}	2.5±0.1	0.20±0.05	1.90±0.1	0.18±0.03	7.8 ± 2.3	0.1±0.03
1	0.05	1.95±0.05	0.04±0.02	1.95±0.0	0.06±0.01	2.4 ±0.8	~0.02
1	0.1	< 2	<0.01	< 2	-	--	
2.5	10^{-5}	2.40±0.05	0.164	1.95±0.0	0.14±0.02	5.6±1.7	0.1±0.03
2.5	0.05	2.00±0.05	< 0.01	2.00±0.0	0.18±0.03	7.8 ±2.3	<0.01
2.5	0.1	1.85±0.05	< 0.01	1.85±0.0	0.16±0.02	6.4±1.9	< 0.01

Table 4.1 Optical constants, film growth rates and deposition flux determined from the fit to the reflectivity data in figures 4.8 and 4.9. Included are the effective optical constants of the film (n_{eff}, k_{eff}) and the film growth rate, δ_{film}, as well as the refractive index of the GaN component in the mixture (n_{GaN}) and gallium fraction in the films, f_{Ga}. The deposition flux, j_{dep}, was estimated from the film growth rate (see section 4.5.3 for details).

These values illustrate that, while the introduction of a background gas leads to a significant reduction in the rate at 1 J cm^{-2}, the reduction at 2.5 J cm^{-2} is comparatively small. At this fluence, it appears that the growth rate is optimised when the gas pressure is maintained at 0.05 mbar, though the comparatively low growth rate measured in high vacuum may indicate that sputtering and evaporation are significant material removal process (thus $c_e \neq 0$), particularly since the mean ion energy (~20 eV) from figure 4.5 is near the threshold for sputtering due to Ga ions (25 eV) as calculated in section 2.3.1. Sputtering of Ga rich films in PLD is dealt with in greater detail in the following chapter on PLD of GaN using a Ga target.

4.5.4 High temperature growth guidelines

Over the range of the values listed in table 4.1 (~ 2×10^{15} to 8×10^{15} cm^{-2} s^{-1}), a quick comparison with the decomposition flux data of figure 1.6 suggest the substrate temperature should not be increased above 830 °C if decomposition is to be avoided. The

deposition flux can also be compared with the ion probe data of section 4.4, where the ion flux per shot at a fluence of 2.5 J cm^{-2} was found to be ~ 5×10^{13} cm^{-2}. This is approximately one order of magnitude less than the deposition flux per shot (note the values in table 4.1 are per second, where the repetition rate was chosen as 10 Hz), indicating that the ion fraction in the plume is about 10% at this position (the actual value may be lower since this estimate ignores sputtering which is likely to be significant in high vacuum).

4.6 High temperature film growth

4.6.1 Reflectivity results

Figure 4.12 illustrates the effect of laser fluence and shot repetition rate on the reflectivity *vs* shot number at a substrate temperature of 700 °C. The left-hand panel shows how, at a laser fluence of 1 J cm^{-2} and a repetition rate of 5 Hz, there is little or no change in the observed reflectivity (and thus the growth rate), even when the background gas (N_2) pressure is increased from 0.05 mbar to 0.1 mbar.

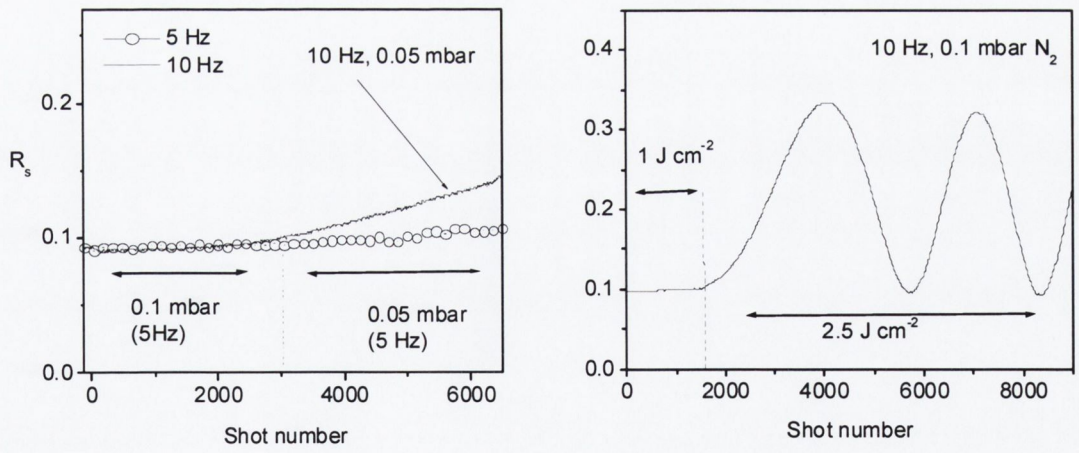

Figure 4.12 Reflectivity for GaN film growth on (0001) sapphire at 700 °C showing the effect of a change in the shot repetition rate (left) and laser fluence (right) on the growth rate.

On the other hand, when the repetition rate is increased to 10 Hz, the reflectivity does exhibit a measurable change over the growth period (10 mins). From table 4.1, the corresponding flux for these conditions (2.6×10^{15} cm^{-2} s^{-1}) serves as a lower limit for the film growth to become significant at this temperature (700 °C) and target-substrate distance (which is close to the temperature predicted in the previous section using the decomposition flux in figure 1.6). The effect of an increase in fluence from 1 J cm^{-2} to 2.5 J cm^{-2} is more dramatic as illustrated in the right-hand panel of figure 4.12; the immediate increase in reflectivity suggesting that the deposition rate is considerably greater than the decomposition rate. Interestingly, the film growth rate appears to increase with thickness (i.e. the oscillation period is decreasing). This behaviour can be expected in the absence of an intentionally grown buffer layer, since the initial nucleation stage is staggered by the large film-substrate mismatch. In this phase of the growth, an unintentionally grown AlGaN buffer layer is likely to form [Vispute et al., 1999] as the first few GaN islands nucleate at Al sites. Once these islands coalesce and growth becomes essentially quasi 2-dimensional [Nakamura and Fasol, 1997], the main GaN film growth stage takes place. From the fit to the reflectivity data, the growth rate was determined to be ~ 0.05 nm per shot for growth in 0.1 mbar N_2 at 2.5 J cm^{-2}, which is about three times less than the value calculated for growth on unheated substrates. The fit also yielded a refractive index for this film of $\check{n} = 2.4\text{-}0.003i$ and the surface roughness was determined to be 10 nm.

4.6.2 XRD results

X-ray diffraction was used to identify the crystalline phase and orientation of the films deposited on heated substrates, while the crystalline quality of the films was compared using the Debye-Scherrer relation (see section 3.4.1.2). Figure 4.13 shows the XRD scans of films grown using two different repetition rates and background gas pressures. Firstly, let us consider the effect of a pressure variation on the diffraction data (left-hand panel); the lower gas pressure appears to lead to a larger grain size (the grain sizes for the films grown in 0.05 mbar N2 and 0.1 mbar N2 are 32 nm and 11 nm, respectively) suggesting that the 0.05 mbar deposition environment is more favourable for crystallisation. This may be due to the effective contribution of the energetic plume species to surface mobility as higher pressures will reduce the kinetic energy of the plume.

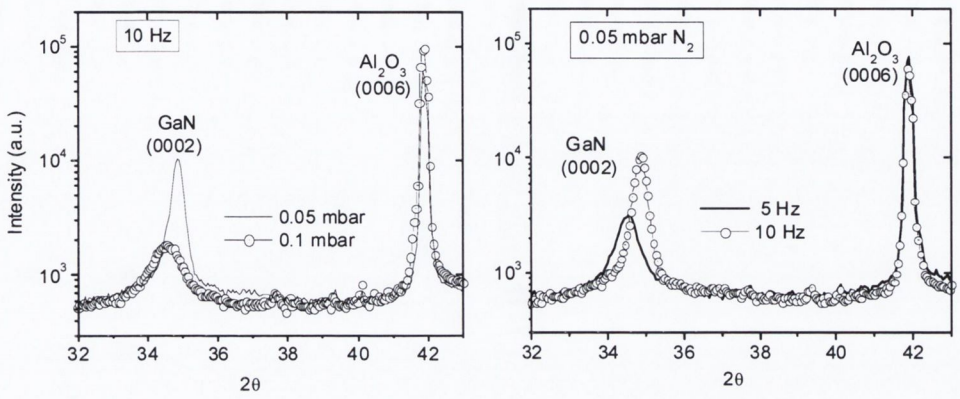

Figure 4.13 XRD θ-2θ scans of GaN films grown on (0001) sapphire at 750 °C illustrating the effect due to a variation of background gas pressure (left) and laser shot repetition rate (right). In all cases the laser fluence at the GaN target surface was 2.5 J cm^{-2}, and the target-substrate distance was 4 cm.

It is also interesting to note that, for the film grown in 0.05 mbar N_2, the peak is shifted to a slightly higher angle than that measured for bulk (fully relaxed) GaN as indicated by the dashed line (2θ=34.65). This would suggest that the lattice planes perpendicular to the plane of the substrate are in compression (the reduction in c parameter, Δc = 0.0075 Å), which again may be due to the energetic species impinging on the growing film. The XRD spectra for films grown at 5 Hz and 10 Hz show a similar variation in both the FWHM and the peak position (right-hand panel). As expected, the higher repetition rate will be accompanied by a higher deposition rate and this leads to stronger diffraction intensity. The narrower FWHM (which, in this case corresponds to an increase in grain size from 17 nm to 32 nm) is perhaps a little surprising considering the longer duration between shots. One might expect that this would result in a more favourable environment for atoms to find minimum potential sites on the film surface. However, it may be the case that the crystalline quality of films is improved as the thickness is increased, and the growth mode is described by the Frank-Van der Merwe, i.e. 2-D layer by layer, model (see, for example, [Horwitz and Sprague, 1994]).

Note: A photoluminescence study of a GaN film grown on sapphire from a GaN target in a N_2 background was carried out at the Centre for Laser Plasma Research at Dublin City

University; the results of this study are presented in the PhD thesis of Kelvin Mah [Mah et al., 2001].

4.7 Concluding remarks

The aim of this chapter has been to establish the minimum fluence and background gas pressure requirements for PLD of GaN using a GaN target. From the point of view of film growth analysis, the requirements were clearly identified from reflectivity data; at a repetition rate 10 Hz, a fluence of greater than 1 J cm^{-2} and a gas pressure of at least 0.05 mbar are required to obtain stoichiometric films and reasonable growth rates. These conditions appear to maintain a deposition flux which is significantly greater than the decomposition flux (i.e. at $T_s \geq 600$ °C), as well as limiting the possible effects of sputtering by reducing the plume ion energies.

Using the ion probe results to identify the reaction path leading to stoichiometric growth is perhaps not so obvious. The ablation process is clearly not congruent (i.e. the ablated target surface is Ga rich); correspondingly, reflectivity data suggests that the plume contains a significant fraction of free gallium, most of which is likely to be in an ionised state (recall that the calculated ion and Ga fractions in the plume were comparable). In a background gas pressure of 0.05-0.1 mbar, it appears that the plume is sufficiently energetic to excite N_2 molecules at least over the first 2-3 cm which, according to the expansion model data in figure 2.3, should provide an adequate number of activated nitrogen species to react with any free gallium at the plume front surface. However, there are many factors which have not been considered that may affect the probability of reaction, not least of which include the short interaction time during the expansion and deposition or the contribution of the electron component of the plume to background gas activation (or indeed recombination).

To gain a further understanding of the reaction kinetics, it would be worthwhile using absorption spectroscopy to gain some measure of the GaN concentration in the plume, either when ablating in high vacuum or at the gas pressures used in this study. This would confirm whether GaN target ablation involves complete dissociation of the GaN molecule, and subsequently, may also identify where GaN formation takes place when

using the higher N_2 gas pressures (i.e. at the plume (shock) front or at the substrate). Otherwise a spectroscopic time of flight study of non-ionic species, might prove useful in obtaining collisional cross-sections of ablated neutrals in the background gas, since in this work only ion-gas collisions have been considered.

5. PLD of GaN using a gallium target

5.1 Introduction

The use of multi-component pressed powder pellets or sintered ceramics, rather than elemental sources, as the target materials in PLD has facilitated its emergence as an effective film growth technique for obtaining novel or exotic materials. Similarly, pressed nitride powder pellets have most commonly been used as targets for PLD of group III nitrides. However, the powders from which such targets are prepared tend to oxidise easily and are of comparatively low purity [Slack, 1973][36] (~ 99.99 %), whereas the group III metals can be obtained in shot or bulk form with purity as high as 99.99999 %. Therefore, the use of a gallium target as a source material for high purity GaN thin film growth is preferable. Potentially, using liquid gallium should offer another advantage over the ceramic target in that hydrodynamic (due to cone formation) and exfoliational ("flaking") sputtering associated with solid target ablation [Kelly and Miotello, 1994] could be avoided. Despite these potential advantages, progress in GaN thin film growth with metal targets has been slow and only recently has material been obtained with structural and optical properties which compare with or surpass those grown using the ceramic target [Merel et al., 2001]. The difficulty lies with the fact that nitride growth from an elemental target in an N_2 background gas relies almost totally on the plume- gas reactions to drive the nitridation process. Otherwise, aggressive environments such as ammonia NH_3 [Nakamura and Fasol, 1997] or hydrazine (N_2H_4) [Nikishin et al., 1997] are required to promote formation of the nitride (alternatively activated plasma sources such as radio-frequency [Fernandez et al., 2000] or electron-cyclotron resonance [Yu et al., 1997] have been used).

[36] The difficulty with preventing oxidation of non-oxide powders is primarily due to the large surface area per grain and the low enthalpy of formation (and thus dissociation) for nitrides. In many cases, the enthalpy of formation for the nitride is only about half the value for the corresponding oxide. For a comparison of the stabilities of oxides and nitrides, see for example Searcy, A. in *Chemical and Mechanical Behaviour of materials,* Searcy, A., D. V. Ragone and U. Colombo, eds., Wiley-Interscience, New York, 1970, pp. 33-55.

The aim of this study is to establish whether N_2 is a viable background gas alternative for GaN growth with a Ga metal target. Similar to the previous chapter, the minimum background gas pressure and fluence requirements were identified by using a Langmuir ion probe to monitor the plume dynamics, and optical reflectometry to measure the film stoichiometry and growth rate. The experimental approach was similar to that taken in the previous chapter; except that a greater range of background gas pressure (10^{-4}-0.4 mbar) and laser fluence (1-10 J cm^{-2}) were investigated.

5.2 Ga target ablation characteristics

5.2.1 Difficulties associated with Ga target ablation

Characterisation of the laser ablation process for gallium is somewhat complicated by the possible existence of both phases (liquid and solid) near room temperature. Accordingly, properties such as the optical absorption, thermal conductivity and the density of the target can change abruptly upon melting (section 1.1) [Iida and Gutherie, 1988a] and vary the ablation characteristics from shot to shot. In addition, the surface profile of the target tends to change considerably during ablation; melting and re-solidification results in peaking of the target centre (see figure 5.1a). Eventually a tilt in the surface plane (and thus the surface normal) of the target takes place, and the direction along which the plume expands tends to vary. This problem is especially evident when the target has completely melted and forms an oblate spheroid[37], as is the case when using a heated substrate[38]. Following the suggestion by Watanabe et al. [Watanabe et al., 1996], a shallow target holder was used (depth ~ 3 mm), but the surface curvature was still significant. The results presented in the following section are taken from experiments with Ga targets which were cooled and solidified beforehand. This was done so as to limit the uncertainty associated with spotsize measurements on the surface of liquid targets, but while the bulk target remained solid during ablation, a thin liquid layer was

[37] For an oblate spheroid, the radius of the polar axis, i.e. the axis along the vertical, is less that the equatorial (horizontal) axis

[38] By embedding a thermocouple in the target holder, it was noted that the temperature of the holder and target could reach temperatures in excess of 100 °C over a 1 hour period when placed 4 cm from a substrate heater maintained at 750 °C.

noticeable on the surface after ablation, particularly for the experiments where a fluence of 2.5 J cm^{-2} or greater was used (after 6000 or so shots).

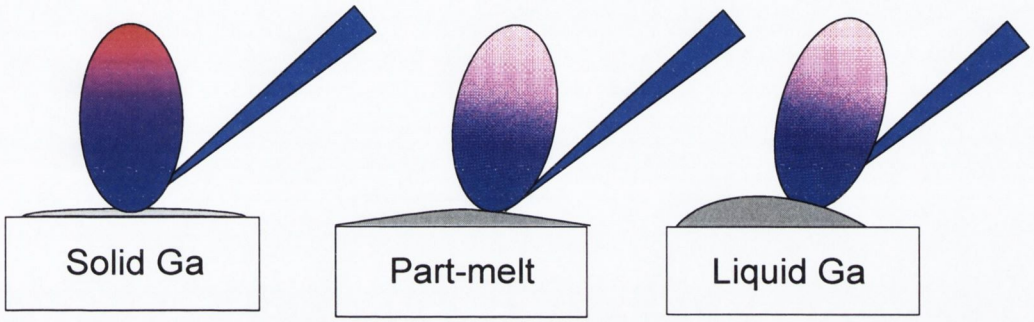

Fig. 5.1a Schematic illustrating how the plume projection can change depending on the degree of melting and surface shaping in laser ablation of Ga metal.

5.2.2 Mass loss for laser ablation of Ga

The average mass loss per laser shot was measured for pre-cooled Ga targets ablated in high vacuum for fluence ranging from near the threshold of ablation up to ~ 5 J cm^{-2}. The targets were ablated at 5 Hz for 20 minutes, accounting for a total shot number of ~ 6000.

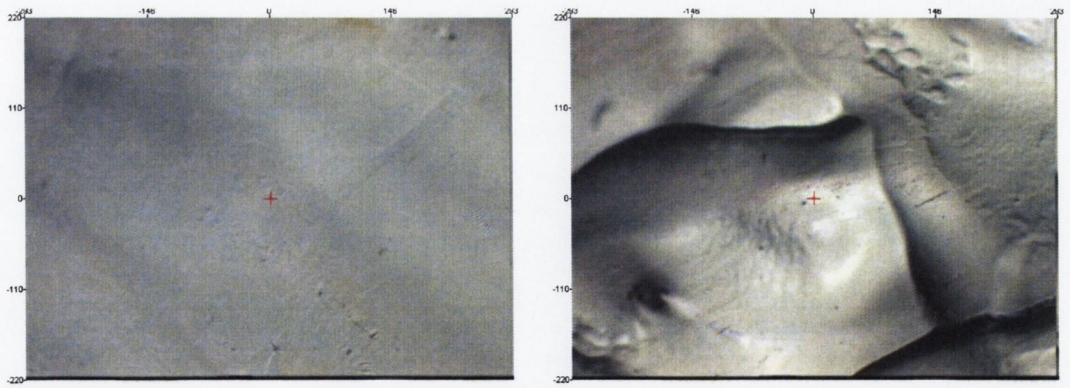

Fig. 5.1b Gallium target surface before (left) and after (right) ablation with ~ 6000 shots at 1 J cm^{-2} showing the rippled surface structure. The images were taken using an optical microscope under white light illumination, and the image dimensions are (0.44×0.58) mm^2.

A photograph of the surface of a gallium target after an ablation run at 1 J cm^{-2} is shown in figure 5.1. Although the targets were completely solid after ablation, there was a considerable amount of rippled surface structure, indicating that while the target may have melted, it had re-solidified. Figure 5.2 shows the mass loss for laser irradiated gallium targets as a function of laser fluence, indicating an ablation threshold of a few hundred mJ cm^{-2}, which is considerably lower than the fluence typically used in PLD of GaN thin films using gallium targets (> 5 J cm^{-2}).

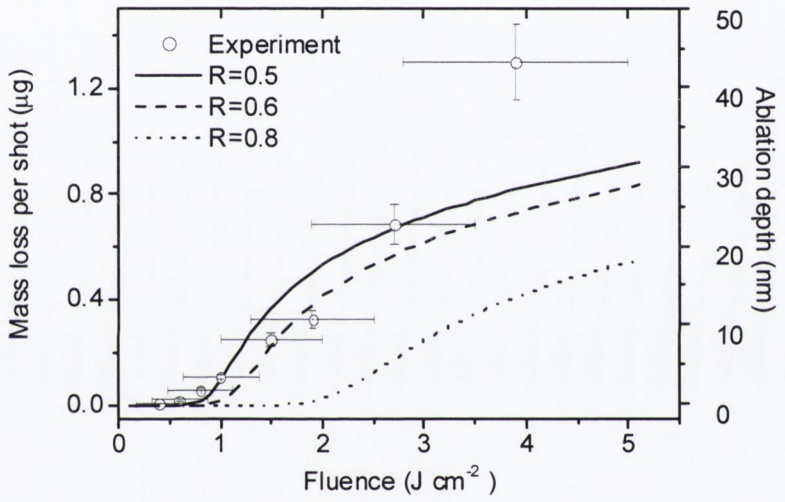

Fig. 5.2 Measured (scatter plot) and predicted (lines) mass loss for gallium target *vs* fluence. The values predicted by the model were determined using different values of surface reflectivity (R) and a photoabsorption cross-section of 10^{-17} cm^2. The ablation depth was calculated assuming a constant fluence over the spot size of 4×1 mm^2.

From this plot, the ablation is best described by a reflectivity of about 0.5, which is somewhat surprising considering the low melting temperature of Ga and the high reflectivity (section 1.1) of liquid Ga (presumably, the target is liquid for most of the laser pulse duration (figure 2.1a), and the reflectivity is closer to that of the liquid). However, previous studies have similarly found that the effective reflectivity for laser ablated metals is less than that measured using low intensity radiation [Jordan, 1998]. For a laser fluence of 2.5 J cm^{-2}, the mass loss (~ 0.6 μg) and corresponding ablation depth (25 nm) for Ga target ablation are significantly lower than for the GaN target (~1.7 μg

and 120 nm, respectively), though this is to be expected since the optical absorption depth for Ga is ~ 7 times less than that of GaN at 248 nm (table 1.1). It is worth noting that the mass loss at 2.5 J cm^{-2} corresponds to a ablation rate of ~5×10^{15} Ga atoms per shot. Interestingly, from figure 5.3, the ablation rate does not appear to be saturating as was observed with the GaN target which, from the outset, is somewhat surprising since one might expect the reflectivity-and thus the degree of target heating-to decrease as the surface liquefies completely. However, it is likely that at this fluence, splashing (due to the impulse imparted by the laser produced vapour; figure 2.1b) and droplet expulsion from the target are becoming significant material removal processes as has been observed in laser ablation of other liquid metals. Fast imaging experiments with molten Bi and Sn targets has shown that splashing in liquid target ablation depends on both the fluence and repetition rate used, and can be avoided provided both these parameters are limited [Toth et al., 1999]. In these experiments, the threshold for the onset of splashing for Sn was much considerably greater than that of Bi (5.5 J cm^{-2} vs 2.5 J cm^{-2}), which may have been related to the surface reflectivity of the liquid targets (the reflectivity of liquid Sn is 4 times greater than Bi at the laser wavelength used). Other factors which are likely to affect the splashing threshold are the surface tension and viscosity of the liquid metal [Manzello and Yang, 2003], and since the reflectivity (section 1.1) and surface tension (γ = 718 mN m^{-1}) of liquid Ga are closer to that of Sn ($R_{248\,nm}$ = 0.71, γ = 560 mN m^{-1}) than Bi ($R_{248\,nm}$ =0.17, γ = 378 mN m^{-1}) [Iida and Gutherie, 1988b; Kantor et al., 2000], it is likely that the splashing threshold for Ga is near 5 J cm^{-2} (the viscosities of all three are comparable).

5.3 Ion probe measurements

5.3.1 Ga ablation in vacuum

The variation with distance of the integrated flux in high vacuum is illustrated in figure 5.3. As in the case of the GaN target, the flux reduces slower than $1/d^2$ (slope of log-log plot = -1.77), but this again may be due to the choice of d (see section 4.4.1). At the substrate position (4 cm), integrated ion flux was comparable with the GaN target case (~

7×10^{13} cm^{-2}).

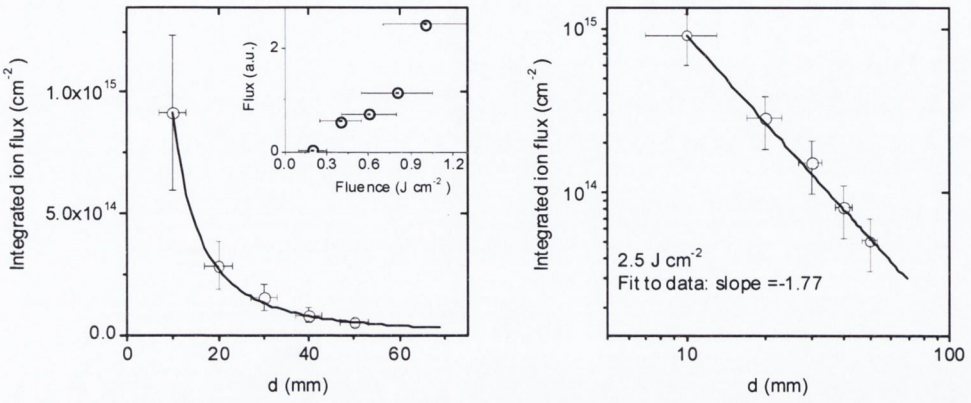

Fig 5.3 Integrated ion flux (scatter points) *vs* distance from a Ga target for ablation in high vacuum (10^{-5} mbar) at 2.5 J cm^{-2}. A log-log plot of the data is shown on the right. The integrated ion flux per shot near the threshold for ion detection (d = 4 cm) is also plotted (inset, left panel).

It is interesting to note that the threshold for ion detection using the probe (left panel, inset) is quite close to the mass loss threshold, suggesting that any vaporised material is easily ionised. Figure 5.4 shows the angular distribution of the integrated ion flux per pulse, normalised to the flux value at θ=0. The data was fitted with the Anisimov profile (equation 2.3a) which allowed the κ_A (1.4) and κ_B (2.0) values (section 2.2.1) to be extracted, and the total number of ions in the plume, using equation 2.3b was found to be $(1.8 \pm 0.7) \times10^{15}$. Considering that the total number of ablated atoms determined from mass loss measurements at this fluence was 5.3×10^{15}, the ionisation fraction appears to be of the order of 35 %, which is significantly higher than the ~10 % value measured with the GaN target. The ion energy associated with the maximum ion flux (section 2.2.3) is plotted for various fluences in figure 5.5a. The energies were measured over a larger fluence range than in the case of GaN target ablation, but even at low fluence the energies are noticeably higher than for the ceramic target (compare with figure 4.5a). Also included is the ion energy distribution generated using the TOF signal for ablation at 2.5 J cm^{-2} in figure 5.5b (right).

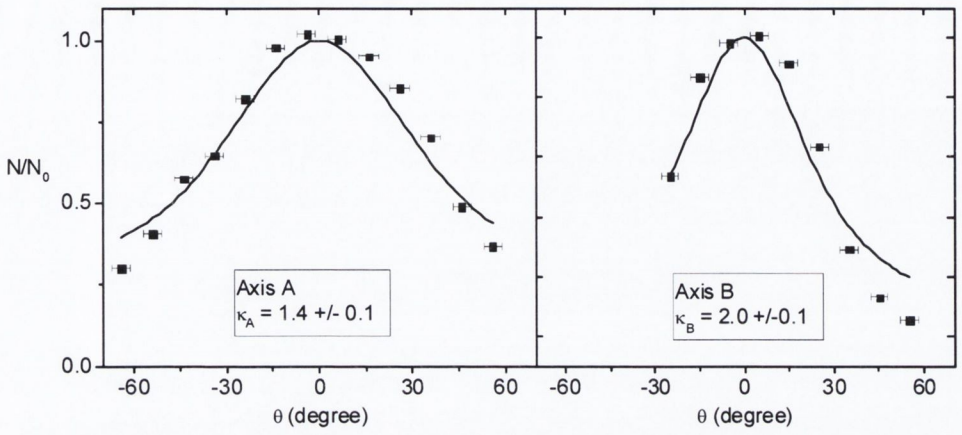

Fig. 5.4 Normalised angular distribution of the integrated ion flux per shot for ns ablation of a Ga target in high vacuum at 2.5 J cm^{-2}. The lines show the fit to the data using the Anisimov model (eq. 2.3a).

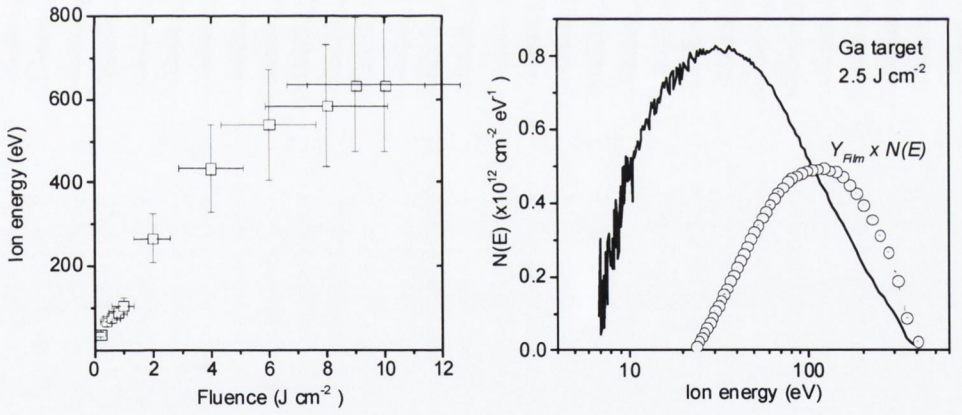

Fig. 5.5 (a) Ion energy, associated with the maximum ion flux, as a function of fluence for ablation of a Ga target in high vacuum (left). (b) Energy distribution for Ga ions calculated using the TOF spectrum for ablation at 2.5 J cm^{-2}, indicating the mean energy (~30 eV). The sputtering yield as a function of incident ion energy, given by equation 2.13, is also plotted (circles) and is used to determine the total yield due to Ga ions (see text).

The mean energy (~ 30 eV) is noticeably higher for the Ga target case (compare with figure 4.5b), which may be related to the surface absorption and evaporation mechanisms

governing both targets. Since the optical absorption (and ablation) depth is much less for Ga, it is likely that once vaporisation is achieved, energy is quickly channelled into ionisation processes. On the other hand, for the GaN target, much of the energy is likely to be expended in decomposition before ionisation takes place. The sputtering yield as a function of incident ion energy, calculated using equation 2.13, is also plotted in figure 5.5b. The total yield per shot, $\overline{Y}_{Film}$, can be calculated by integrating over the ion energy spectrum, as follows [van de Riet et al., 1993]:

$$\overline{Y}_{Film} = \frac{\int Y_{Film} N(E) dE}{\int N(E) dE} \qquad \text{(eq. 5.1)}$$

The yield for the data in figure 5.5b was determined to be 0.95, which indicates an effective sputtering yield of about 0.3 if the ionisation fraction of 0.35 calculated from the mass loss and angular ion distribution data is accurate. The total sputtering yield was calculated in a similar fashion to be between about 0.15 for ablation at 1 J cm^{-2}.

5.3.2 Ion probe measurements in a background gas

Figure 5.6 shows the ion signals at 4 cm for Ga target ablation in various background gas pressures of N_2. It is interesting to note that the peak splitting is more clearly identifiable than in the case of GaN target ablation (compare with figure 4.6). The slope of the natural log plot (inset) of the first peak intensity was used to determine a scattering cross-section of $(2\text{-}4)\times10^{-16}$ cm^2 . It was noticeable that the magnitude of the total integrated flux tended to vary quite a bit, presumably because of the surface structure of the target. Since there is also considerable uncertainty associated with the position of the first peak for the GaN target probe signals (figure 4.6), no conclusive comparisons can be made between the data for both targets at this point except that the degree of scattering is comparable. The distance *vs* time values for the second peak at 2.5 J cm^{-2} in 0.1 mbar N_2 are shown in figure 5.7 as is the fit to the data (solid line) which yielded a $t^{0.4}$ dependence as would be expected from the blast wave model (section 2.2.2.2, [Zel'dovich and Raizer, 1966]). The velocity and ion energy profiles were determined by differentiating the fit to the distance vs TOF data (equation 2.6).

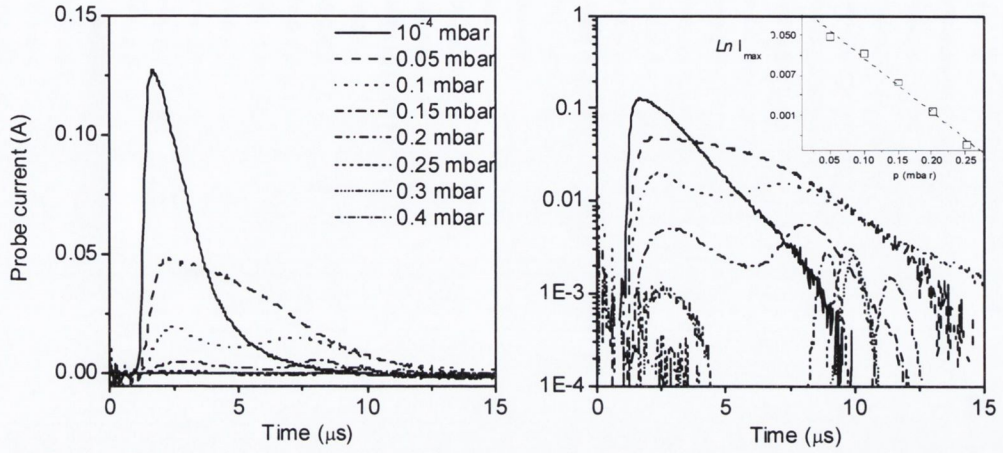

Fig. 5.6 (a) Probe signals for Ga target ablation at 2.5 J cm^{-2} in various N_2 background gas pressures taken 4 cm from the target. The data is also plotted on a log scale (right) to allow easy identification of the first peak intensity (I_{max}). The reduction in the intensity, plotted on a natural log scale, is shown in the inset.

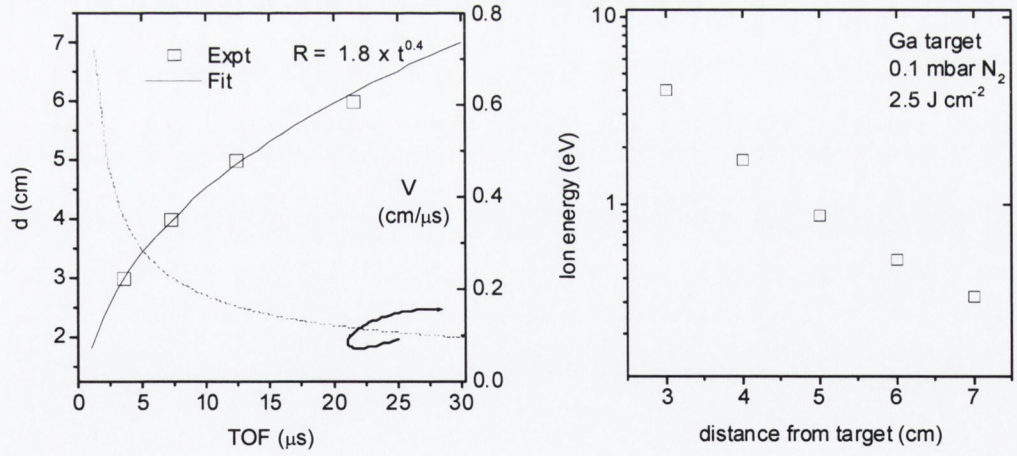

Fig. 5.7 Expansion dynamics for the shockfront (2nd ion signal peak) in 0.1 mbar N_2 at 2.5 J cm^{-2} using a gallium target: (a) Distance *vs* TOF (scatter plot) and velocity profile for Ga target ablation in 0.1 mbar N_2 (left) and (b) the corresponding ion kinetic energy calculated from the velocities (right).

From figure 5.7b, it is noticeable that the ion energies quickly reduce to a few eV within 3 cm from the target. The results are somewhat surprising, particularly since in vacuum, the Ga ion energies are higher when using the Ga target. It may be the case that the scattering cross-section is strongly dependent on the initial ion velocity in this kinetic energy range, particularly in the several hundred eV range where the energy distributions were noticeably different (compare figures 4.5b and 5.5b). It was found that higher background gas pressures were required to obtain reasonable film growth rates when using the Ga target. This is discussed in greater detail in the section on growth at high temperature; for the moment it is worth considering the corresponding probe signals at these pressures (see figure 5.8 below). In this pressure regime, only the second peak is detected, indicating that essentially all of the ions in the plume have interacted with the background gas and the plume is confined within the shockfront.

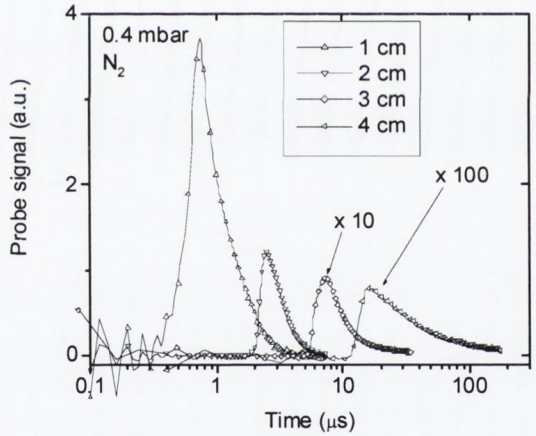

Fig. 5.8 Ion TOF signals for gallium target ablation at 2.5 J cm^{-2} at various distances from the target in 0.4 mbar N_2 (the data has been plotted on a semi-log scale for clarity).

Under these conditions, excitation of the background gas should be greatly limited to within a cm or two from the target, and the plume energy is thermalised rapidly as the distance increases. Taking, for example, the TOF of the maximum in the ion flux for the probe signals at 3 cm (7.5 μs) and 4 cm (15 μs), the instantaneous velocity can be calculated as 1.33 km s^{-1}, which corresponds to an ion energy of about 0.6 eV. At this point, it may seem that the requirement for higher background gas pressures to achieve

stoichiometric growth is purely due to the higher number of free Ga species in the Ga target plume compared to ablation with the GaN target (recall from chapter 4 that the free Ga fraction determined from reflectivity for growth with the GaN target was only ~ 0.1, which gives the total number of free Ga atoms in the GaN target plume as ~ 0.1×10^{16}). This may indeed be the case, as the surface density of activated N_2 particles should increase with pressure (from 0.1 to 0.4 mbar) by a factor of about 4 assuming the accumulation model of section 2.2.2 (figure 2.3) is applicable.

5.4 Deposition on unheated substrates

Thin film deposition on sapphire substrates in both high vacuum and in (0.05-0.1) mbar of N_2 using gallium targets was monitored in-situ using the reflectivity setup described in section 3.4.2. For a comparison with growth from the GaN target, films were deposited using fluences of 1 and 2.5 J cm^{-2}, with the reflectivity signals for growth at this fluence shown in figures 5.9 and 5.10, respectively. In general, the signals show quite erratic behaviour and are difficult to model; as a result only some of the traces show a fit given by the model (solid lines). The high vacuum traces (top panels) differ considerably from the traces for growth in 0.05-0.1 mbar N_2, and it is worth considering each of these cases individually. For the traces which were fitted with the reflectivity model, the optical constants and deposition rate (as well as the Ga fraction) extracted from the fit are listed in table 5.1.

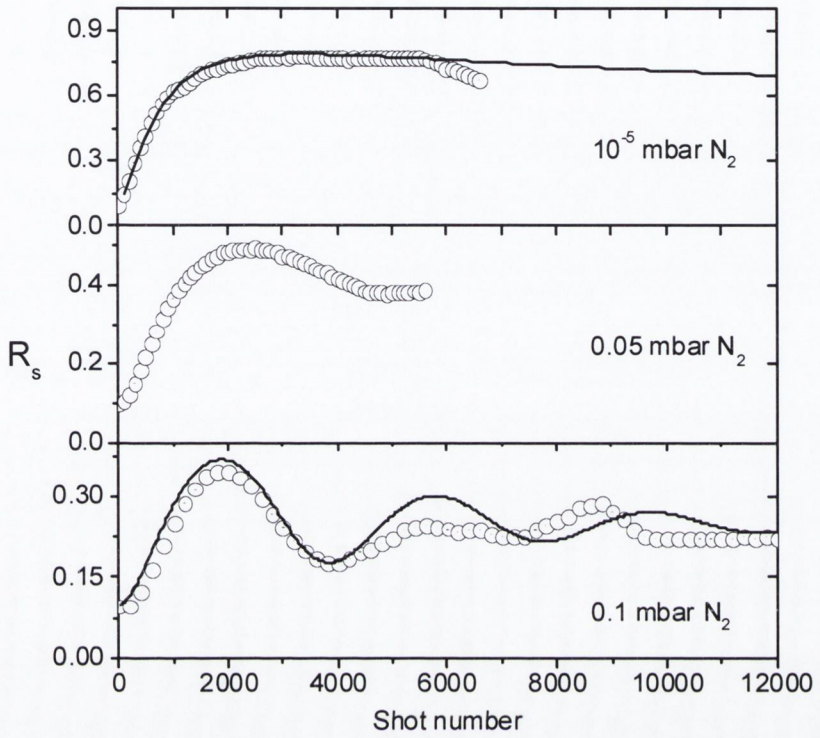

Fig. 5.9 Reflectivity trace for films deposited in 10^{-5} (top), 0.05 (middle) and 0.1 (bottom) mbar N_2 using a gallium target and a fluence of 1 J cm^{-2}. The data has been fitted with the reflectivity model (solid line), and in the high vacuum case a surface roughness value of 50 nm (for comparison with growth using the GaN target see figures 4.8 and 4.9).

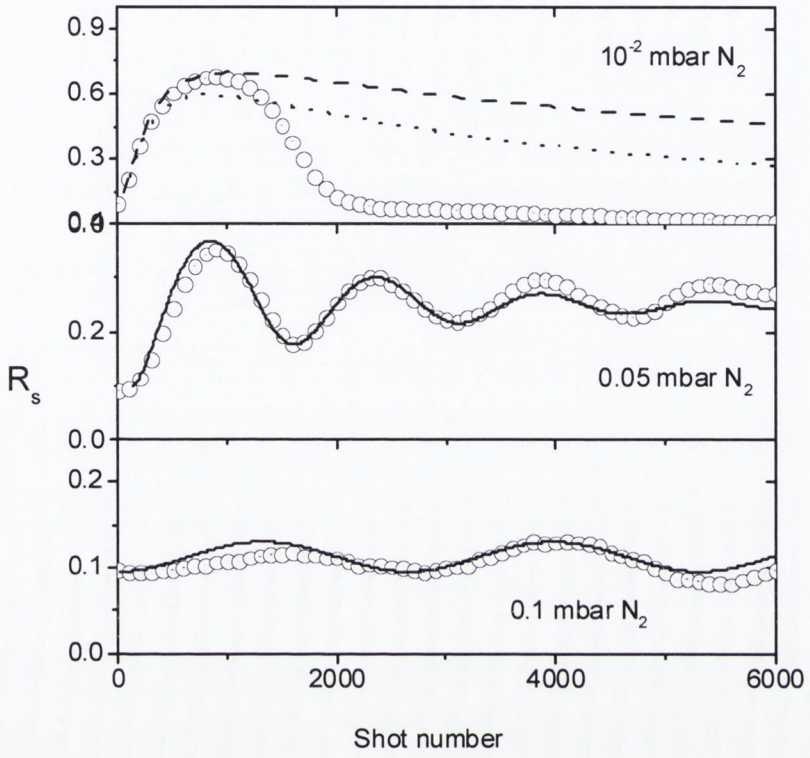

Fig. 5.10 Reflectivity traces for films deposited using a gallium target at 2.5 J cm^{-2} in (top to bottom) 10^{-5}, 0.05 and 0.1 mbar N_2. The trace in high vacuum was fitted using the *n* and *k* values for liquid Ga (table 2.1) and a surface roughness of 75 nm (dashed line) and 100 nm (solid line). The traces for 0.05 mbar and 0.1 mbar were fitted using the Bruggemann model (see table 5.1 for Ga fraction).

5.4.1 High vacuum growth

The high vacuum (top panel, figure 5.9) trace at 1 J cm^{-2} is typical of a metal film, although the maximum reflectivity reached after a few tens of nm appears to be significantly lower than that expected for a smooth, thick Ga film (i.e. when the film thickness well exceeds the optical absorption depth (~ 10 nm), the reflectivity should be close to that of the bulk as in figure 2.5). The fitted (solid) line included with this trace was generated using a final surface roughness value of 50 nm. However, the growth rate using this fit is only 0.008 nm per shot which corresponds to a total film thickness of ~ 50

nm. Although this may seem surprising since the ablation rate and total ion flux per shot for Ga targets are comparable to the GaN target case (where the deposition rate was typically 0.1 nm per shot in vacuum), it is likely that sputtering is considerably reducing the film growth rate, as seems evident from the sputtering yield calculations of section 5.3.1. The trace for ablation at 2.5 J cm^{-2} in high vacuum (fig. 5.10, top panel) indicates an extremely rough film, and no conclusive information could be extracted with regard to the film thickness or growth rate. The overall fit to the data is quite poor, even with surface roughness values of the order of 100 nm as indicated in the plot, though the fit is reasonable for the first 1000 or so shots using a value of σ_{final}=75 nm (section 2.3.2.3 details the surface roughness model). Sputtering by high energy ions may be contributing to film roughness considering the total sputtering yield calculation in the previous section (section 5.3.1).

E (J cm^{-2})	p (mbar)	n_{eff}	k_{eff}	f_{Ga}	δ_{Film} (nm/shot)
1	10^{-5}	1.4±0.1	6.9±0.05	~1	0.008±0.001
1	0.05	-	-	-	-
1	0.1	2.7±0.2	0.3±0.1	0.12	0.016±0.003
2.5	10^{-5}	1.4	6.9	~1	See text
2.5	0.05	2.7±0.1	0.3±0.05	0.12±0.02	0.08±0.01*
2.5	0.1	1.9±0.1	< 0.01	< 0.01	0.07±0.01

Table 5.1 Data extracted from the fit to some of the reflectivity signals for growth using the gallium target. The table includes the effective optical constants (n_{eff}, k_{eff}), the gallium fraction (f_{Ga}) and the growth rate (δ) given by the fit (see section 4.5.3 for details of the deposition rate calculation). For the films grown in high vacuum, the optical constants of liquid Ga at 635 nm were used (table 1.1). * It was possible to measure the thickness of this film using the profilometer, which yielded a value of (0.07±0.015) nm per shot.

5.4.2 Growth in 0.05 and 0.1 mbar N_2.

It is interesting to note that with the introduction of N_2, the behaviour of the reflectivity trace at both 1 J cm^{-2} and 2.5 J cm^{-2} is qualitatively similar to the variation observed in the corresponding traces when using the GaN target. The damped oscillation associated with these traces is typical of a poorly conducting metal or absorbing dielectric,

indicating that the films are likely to consist of a mixture of GaN and free gallium. Since it was not possible to confirm the deposition rate in high vacuum (e.g. using profilometry), one can only speculate as to the effect of the increase in background gas pressure, though the pressure increase from 0.05 mbar to 0.1 mbar appears to have little effect on the rate at 2.5 J cm^{-2} (this was similarly observed in the case of the GaN target, see table 4.1). Although it seems that the higher pressures and fluence lead to a reduction in the Ga fraction, and it may be necessary to further increase both the fluence and gas pressure in order to obtain full stoichiometry. An important consideration for high temperature growth is the fact that the deposition rate using the Ga target in (0.05-0.1) mbar N_2, at ~ 0.07 nm per shot, which is low in comparison with growth using the GaN target at the same fluence, and was shown to be insufficient to maintain a reasonable growth rate with a GaN target once the substrate temperature was increased to ~ 700 °C (section 4.6.1).

As a final note regarding films grown by PLD on unheated substrates using a Ga target, X-ray diffraction analysis revealed that these films were amorphous. Thus high temperatures are required for crystalline GaN growth, as was observed when using the GaN target.

5.5 Deposition on heated substrates

5.5.1 Reflectivity for high temperature growth

A number of general comments can be made with regard to the deposition requirements for growth at high temperature using the gallium target, in particular, the following fluence and pressure were required to obtain oscillations in the reflectivity trace:

- A fluence of at least 2.5 J cm^{-2}
- A background gas pressure of at least 0.2 mbar N_2

Furthermore, it was noted that the growth rate strongly depended on the target substrate distance. Because of the fluence requirement, much of the deposition was carried out at 3 J cm^{-2} and above. At a substrate temperature of 700 °C, it was noted that the growth rate was insignificant unless the background gas pressure was increased above 0.2 mbar N_2,

as indicated in figure 5.11. Also included in this figure (bottom) is the variation of reflectivity signal for growth at two different substrate temperatures.

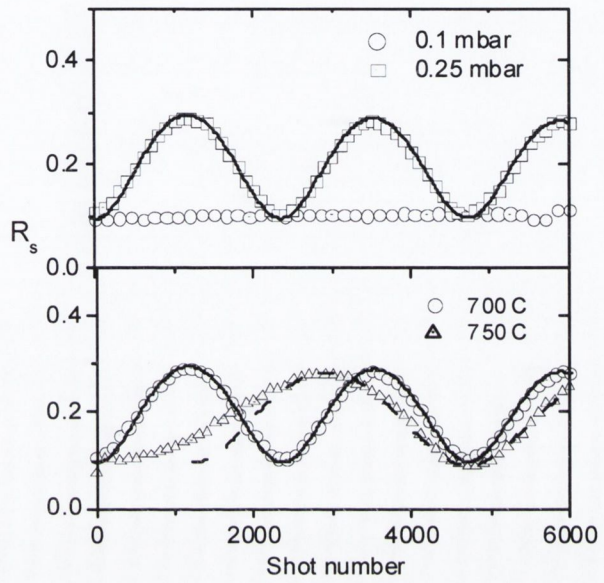

Fig. 5.11 Reflectivity traces for films grown using a gallium target in a N_2 background at 3 J cm^{-2}, indicating the effect of gas pressure (top) and substrate temperature (bottom) on the growth rate and surface roughness. The dashed line in the lower plot is the fit to the higher temperature data, after a thousand or so shots where the rate appears to stabilise.

Although an increase of ~ 50 °C results in a reduction of the growth rate from 0.07 nm per shot to (0.03-0.04) nm per shot, these growth rates are still quite high, and comparable to the rates observed when using GaN targets in 0.1 mbar N_2. The traces also indicate that the films are quite smooth, though the film grown at 750 °C showed a higher value of roughness (25 nm) than the other films grown at 700 °C (10 nm). For both sets of data, the fit to the data yielded a refractive index of $\hat{n}$=2.35-i 0.01.

In some trial experiments, films were deposited at pressures of up to 5 mbar N_2; at this pressure, a fluence of about 8 J cm^{-2} was required to obtain a variation in the reflectivity signal. From the reflectivity data for these films, the growth rate is comparatively high (~0.1 nm per shot), but the traces also suggested that the films were quite rough. Nevertheless, it seems that a high fluence and high pressure may be the only route to

obtaining highly oriented crystalline thin films in a molecular nitrogen background, as revealed by XRD measurements on the films.

5.5.2 XRD results

X-ray diffraction measurements on films grown using the gallium target have revealed that while sufficiently high growth rates were observed at 700 °C -750 °C, the microstructure was in many cases amorphous, and only by further increasing the substrate temperature was crystalline growth achieved.

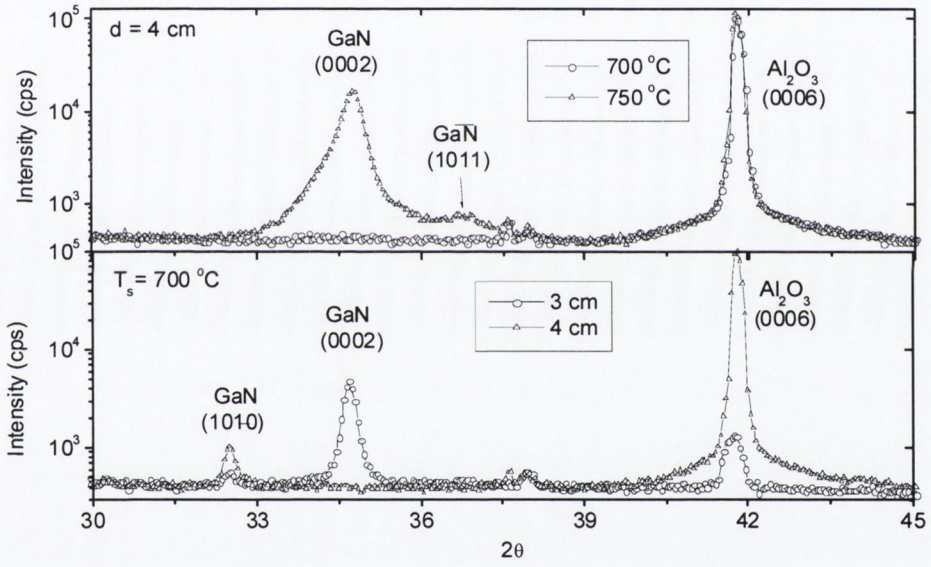

Fig. 5.12 XRD scans of films grown using a gallium target illustrating the effect of substrate temperature (top) and target-substrate distance (bottom) on the film structure. All of the films were deposited in a N_2 background gas pressure of 0.25 mbar, while the laser fluence was maintained at ~ 3 J cm^{-2}.

Figure 5.12 illustrates the rather dramatic effect of an increase in substrate temperature from 700 °C to 750 °C (top panel) at a target substrate distance of 4 cm, indicating that the structure goes from being amorphous to polycrystalline (the XRD spectra in this panel correspond to the reflectivity curves in the bottom panel of figure 5.11). The figure also includes the X-ray diffraction spectra for two films grown at 700 °C, but at different

target –substrate distances (3 cm and 4 cm). In all cases, the background gas pressure and laser fluence was 0.25 mbar and 3 J cm^{-2}, respectively. It seems that an increase in substrate temperature has the same effect as a reduction in the target substrate distance; that of a change from polycrystalline or amorphous growth to predominantly c-axis growth. Despite the improvement in crystal structure observed under the conditions described above, the FWHM of the (0002) peak is comparatively wide, indicating a small grain size. Interestingly, a reduction of the target-substrate distance rather than an increase in substrate temperature led to a narrower FWHM and correspondingly greater grain size (55 nm *vs* 25 nm). As mentioned briefly above, growth was also carried out at comparatively high pressure (5 mbar) and fluence (8 J cm^{-2}), to achieve reasonable higher growth rates at higher temperatures.

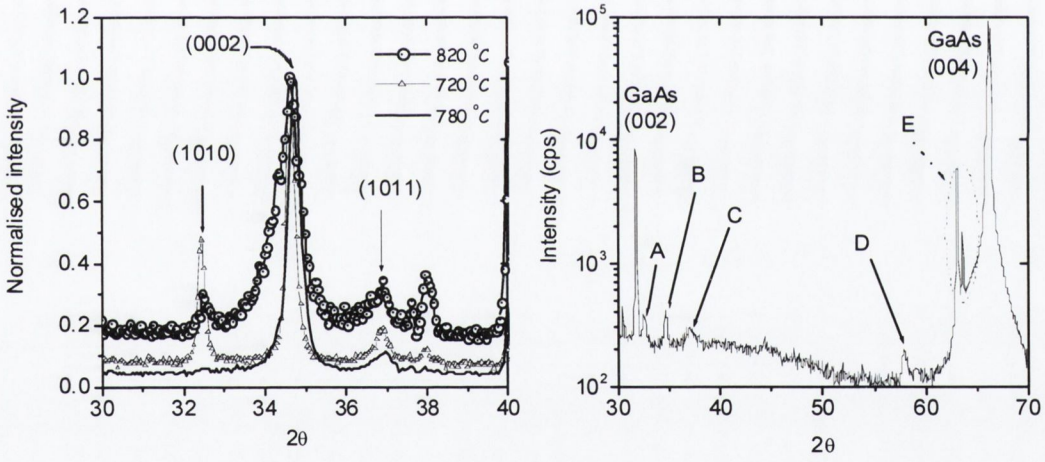

Fig. 5.13 XRD spectra for films grown at ~ 8 J cm^{-2} in a 5 mbar N_2 background using a liquid Ga target. (a) Patterns for films grown at various substrate temperature on (0001) sapphire. The plots have been normalised against the (0002) c-axis peak of the film grown at 780 °C (left). (b) XRD of a film deposited on a GaAs substrate using a Ga target in 5 mbar N_2. The GaN peaks are given by: A$(10\bar{1}0)$, B(0002), C$(10\bar{1}1)$ and D(1100). The narrow peaks denoted by "E" are impurity (tungsten) lines.

Figure 5.13 shows the effect of substrate temperature on the crystalline orientation of these films. Again, the GaN (0002) peak becomes more prominent as the temperature is increased above 700 °C, however, the other growth orientations were found to reappear

as the temperature was increased above 800 °C. In an attempt to promote cubic GaN growth, a film was deposited on an *a*-cut (100) epi-ready[39] GaAs substrate. A low temperature buffer layer was also included in this particular growth, with deposition being carried out at 500 °C for approximately 2000 shots, in a procedure similar to that used in MOCVD growth of GaN [Nakamura and Fasol, 1997]. The main growth stage was carried out at 700 °C, for 6000 shots, and the background gas pressure was maintained at 5 mbar. However, XRD of the film revealed only a number of low intensity GaN peaks indicating a polycrystalline structure (see figure 5.13b).

Note: Some of these films grown using a liquid Ga target were characterised using the low temperature photoluminescence apparatus outlined in section 3.4.4. The details of the measurements are discussed in detail in the PhD thesis of Kelvin Mah [Mah, 2002] and elsewhere [Mah et al., 2002].

5.6 Concluding remarks

While the focus of this exploratory study of PLD of GaN using a Ga target was in line with the previous chapter in trying to establish the requirements for stoichiometric film growth, a number of difficulties have been identified with regard to the metal target's suitability as a PLD target. These include constraints on target preparation, particularly the surface flatness, which leads to large variations in the shot to shot ablation rate and angular distribution. Furthermore, the surface reflectivity of liquid Ga is quite high, thus high fluence may be required to achieve adequate ablation (and deposition) rates, which it seems leads to droplet expulsion and splashing. On the other hand, the ionisation fraction in the plume appears to be quite high (~0.5), as do the ion energies, which should aid activation of the background gas. While comparatively high gas pressures (≥0.2 mbar) seem to facilitate stoichiometric film growth and increase growth rates, this may in part be due to reduced sputtering as it is due to an increased activated N_2 density in the target-substrate region. Once again, a spectroscopic study of the plume, to confirm if ablated gallium is nitrided before reaching the substrate, would be most informative in this regard. In any case, these higher background gas pressures seem to require higher fluence

[39] These particular substrates have been etched and individually sealed under vacuum to ensure that the surface is free of an oxide layer before deposition.

(≥ 3 J cm^{-2}), to maintain reasonable growth rates at high temperature which again leads back to the problem of splashing when using a liquid target.

It may be possible to overcome a number of the difficulties outlined above, for example, a cooling mechanism can be incorporated in the target holder [Merel et al., 2001] to maintain a solid target (though simultaneous target cooling and target rotation under high vacuum conditions is not easily achieved). With regard to the pressure requirements of the N_2 background, Willmott et al. [Willmott et al., 2000] have shown that a pulsed N_2 gas jet could be successfully employed to grow GaN films which exhibited strong band-edge luminescence at room temperature. The gas pulse was synchronised with the expansion of the ablation plume so that it created a highly collisional environment, rich in excited nitrogen species[40], for the duration of the plume expansion. Otherwise, such a dense environment could only be obtained by using a high static background gas pressure, as seen in this work.

In light of the difficulties identified with using the liquid target, and the demands placed on the plume to supply the energy necessary for excitation of the background gas, it seems that N_2 is not a suitable background gas for high quality GaN thin film growth using liquid gallium. Preferably an external means of exciting the background gas should be employed to remove the high fluence requirements and reinstate the benefits of using a liquid target.

[40] This pulsed gas delivery system delivers ~ 10^{17} N_2 molecules to a region just over the ablated target. The valve on the jet is opened for ~ 400 μs.

6. Plasma-assisted PLD of GaN

6.1 Introduction

The suitability of nitrogen plasma discharge sources for the growth of nitrides becomes apparent considering the observation by Newman [Newman, 1997] that atomic nitrogen, or the excited states of neutral or ionised molecular nitrogen, provide sufficient energy to overcome the kinetic barrier to the reaction of gallium and nitrogen at typical PLD growth temperatures and pressures (recall the energy diagram in figure 1.4). Many discharge sources also offer a reasonable degree of control over the flux and type (i.e. molecular or atomic) of activated species in film growth. The ideal source should provide excited species with low kinetic energies to limit sputtering of the substrate and growing film [van de Riet et al., 1993]. Anders and co-workers have shown that in the small-anode DC discharge developed by Miljevic [Miljevic, 1984], the ion energies are less than 20 eV, and are suitable for MBE growth of GaN [Anders et al., 1996]. Since a low pressure deposition environment (< 0.1 mbar) is required to operate this source, it should also be suitable for discharge-assisted PLD of nitrides. To date, a number of other types of plasma source (e.g. radio frequency [Fernandez et al., 2000; Basillais et al., 2002], electron-cyclotron resonance [Merel et al., 2001] and microwave [Deiss et al., 2001]) have been used in PLD with metal targets and yielded good control of the III:V ratio in films.

Considering the obvious potential offered by a plasma-assisted deposition environment in PLD of GaN, an attempt was made to identify a simple means of creating a nitrogen plasma which would promote nitride formation either during the plume expansion stage or at the film growth stage on the substrate (or both). Two types of source were constructed; a "small-anode" discharge and a pulsed discharge which was ignited by the ablation plasma. A commercially available source was also acquired, and while all three sources provide active nitrogen in the deposition environment, the operation principle of each differed considerably. The basic power and gas delivery requirements have been outlined in chapter 3 (section 3.3), and before discussing the operational features of the

individual sources, it is worth summarising some of the basic features of electrical discharges to understand the behaviour of these devices.

6.2 Glow discharges

Excitation and ionisation of a low pressure gas is simply realised by setting up a d.c. discharge between two electrodes (see figure 6.1). At a potential difference of a few volts, any free electrons in the gas will be attracted towards the anode and correspondingly ions towards the cathode, thus establishing a small current. Once all of the free charges have migrated to the electrodes and the saturation voltage is reached (V_1), further increasing the voltage difference has little effect on the discharge current until the voltage is increased above the ionisation potential of the gas (V_2), in which case electrons accelerated through the electric field can acquire sufficient kinetic energy to ionise the gas. This initiates an accumulative process whereby the number of electron-ion pairs generated grows quickly (avalanche effect).

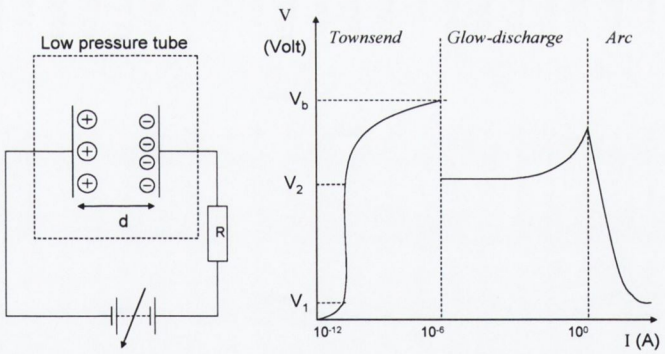

Fig. 6.1 (a) Schematic of a typical d.c. plasma source for low pressure (1-100 mbar) discharges (left). The ballast resistor, *R*, is essential for normal glow-discharge operation. (b) Voltage-current characteristics of the d.c. plasma (right).

This effect alone will not sustain a glow discharge; however, secondary electrons released from the cathode (due to bombardment by positive ions) provide enough charge

to replenish the discharge region[41]. The number of electrons released per incident particle at the cathode is given by the secondary electron emission coefficient, γ_{se}, which depends on the ion type and cathode material[42] [Penning, 1957; Chapman, 1976]. When enough electrons are released from the cathode such that the current can grow exponentially, coronal discharges take place before the discharge sparks or breaks down at a voltage which depends on the product of the pressure and the electrode separation (*pd*), given by the Paschen law:

$$V_b = \frac{C_1 pd}{\ln(C_2 pd) - \ln\left(\ln\left[1 + 1/\gamma_{se}\right]\right)} \qquad \text{(eq. 6.1)}$$

Here C_1 and C_2 are experimentally determined constants know as the Townsend coefficients. For a fixed plate separation, *d*, there will be a minimum in the Paschen curve corresponding to a minimum pressure at which breakdown can occur. This feature of d.c. discharges should be taken into account when designing a plasma source, if either the source pressure or electrode separation must be fixed. The Paschen curve for N_2 has been reported by a number of groups and is given in appendix F (see [Dakin et al., 1974] for a summary of previously reported data). From this curve, the minimum break down voltage corresponds to a pressure-distance product value of ~ 10 mbar mm. The electrode separation in our d.c. discharges is typically 5-10 cm; thus the pressure between the electrodes should be maintained at ~ 0.1 mbar so as to minimise the breakdown voltage requirements of the device. In a basic d.c. glow discharge, where the parallel electrodes are of the same dimension, most of the potential drop is at the cathode, over a region where electrons acquire enough energy to ionise the gas.

---

[41] Even ions with zero velocity at the cathode can liberate electrons, since for relatively inert gases, the potential energy of the ions is often ≥ 10 eV, while the energy required to release a secondary electron is no more than a few eV.

[42] The value of γ_{se} also depends on the ratio of the electric field strength to the discharge gas pressure (*E*/*p*). Excited neutrals or photons bombarding the cathode can lead to secondary electron emission, but the photoelectric yield for pure metals at visible and near UV frequencies is only ~ 10^{-4} [Chapman, 1976].

6.3 Operational features of the small-anode discharge

6.3.1 Importance of the anode size in a small anode discharge

The constricted or small anode ion-electron source is based on the basic d.c. glow discharge outlined above but with one important change; the anode area is considerably less than that of the cathode. The effect of this change is to produce an intense region of excitation and ionisation at the anode (a bright ball of plasma is observed at the orifice as illustrated in figure 6.3b). The reduced anode area leads to an increase in the electric field intensity within the anode sheath. In fact, the sheath thickness increases in order to maintain the current balance between the plasma and the anode[Anders and Anders, 1995][43].

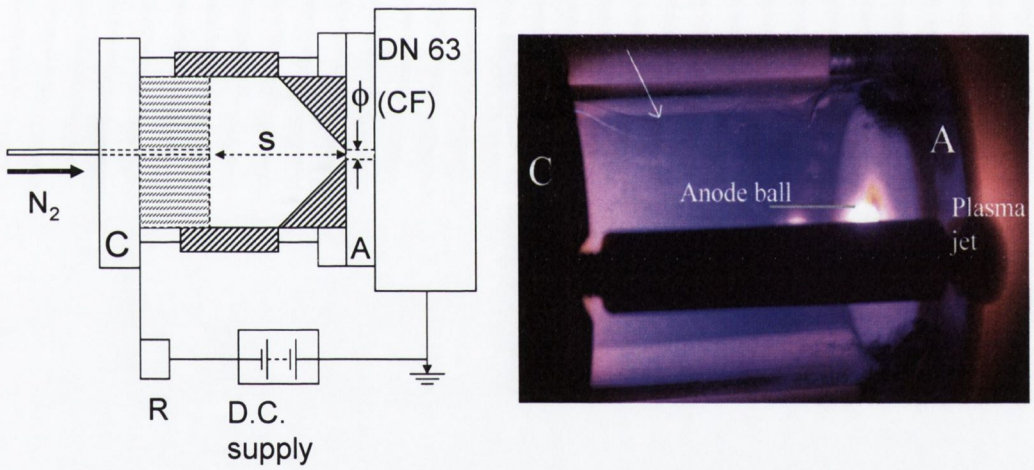

Fig. 6.3 (a) Cross-sectional schematic of the small anode discharge (left). The darkly shaded region represents the ceramic used to separate the cathode (C) and anode (A), and to cover most of the anode except for the orifice of diameter (ϕ). The aluminium tube used to reduce the cathode-anode separation (s) is represented by the lightly shaded region. A double-sided DN40 CF adapter (304 stainless steel, 2mm thickness) was used as the anode. (b) A photograph of the small anode discharge constructed using aluminium

[43] Anders and Anders compared the electron temperature and density in glow discharges with and without a small anode, noting a significant increase in both parameters when the anode diameter was reduced to below 3 mm, while the cathode was maintained at a few cm diameter.

electrodes (C=cathode, A=anode) and a quartz tubing (note crack appearing in tubing as indicated by the arrow).

Normally, the anode potential drop is only about 10 V, which is insufficient to cause significant ionisation in this region. However, the ionisation rate is dramatically increased by the larger potential drop established by the reduced anode size, since the ionisation scattering cross-section for electrons with nitrogen molecules is maximised at ~ 100 eV (recall figure 1.8 [Tian and Vidal, 1998]). Along with the simplicity of its construction, there are a number of other reasons which make the small-anode discharge an attractive option for film growth:

- Low input power requirements. Once breakdown is achieved, a normal glow discharge will run at less than 100 Watt of electrical power (RF and microwave sources typically consume several hundred Watts of power).
- No high voltage electrodes in the deposition environment (grounded anode).
- High flux of excited neutrals and ions with low kinetic energies.
- No hot filaments; can be used to activate corrosive gases e.g. oxygen.

6.3.2 Source construction

The basic design and materials used in the construction of the small anode discharge cells were introduced in section 3.3; here we discuss some of the operational features and plasma characteristics of the sources.

Device #1: Aluminium electrodes/quartz separator[44]

The first device assembled consisted of aluminium electrodes (35 mm diameter), 50 mm apart, separated by a quartz insulating tube. The anode was covered with a Macor© (AlN) ceramic disc, through which was drilled the small anode hole (ϕ = 2 mm). Although the device produced a strong jet of luminous plasma which was projected into the deposition chamber (see figure 6.3b), it failed after a number of trial runs because of heating induced damage. Considering that the power dissipated at the cathode is (10-50) W, for a

[44] This device was designed and constructed by Juan Castro at the Physics department, TCD. The initial operation and characterisation of the source was carried out by Eduardo de Posada (Physics department, TCD).

discharge current of a few hundred mA (~10 W will be dropped across the ballast resistor), the temperature can rise as quickly as a few tenths of a degree per second in the absence of an efficient heat removal system:

$$\frac{\Delta T}{\Delta t} = \frac{\Delta E}{m_c c_c \Delta t} = \frac{P}{m_A c_A} = \frac{\sim 30W}{100g \times 0.9Jg^{-1}K^{-1}} \cong 0.3Ks^{-1} \qquad \text{(eq. 6.2)}$$

In this estimation, m_c and c_c are the mass and specific heat capacity of the cathode, respectively. The nitrogen line to the cathode consisted of a UHV grade nylon piping with low thermal conductivity (≤ 0.01 W $cm^{-1}K^{-1}$). Quartz is also a poor thermal conductor (~0.001 W $cm^{-1}K^{-1}$); thus heat conduction away from the cathode is low in comparison with heat generation. Radiative losses at a few hundred °C are low in comparison with the rate of heat generation (maximum power emission by radiation is ~7 W for T=500 K, 5 cm diameter electrode, emissivity = 1).

Device #2: Stainless steel electrodes / AlN separator

A second device was constructed using a commercially available AlN separated DN 40 CF adapter, the dimensions of which are given below (figure 6.5). To reduce the risk of heating induced damage, the cathode was convectively cooled by a fan heater positioned directly underneath it (recall figure 3.3).

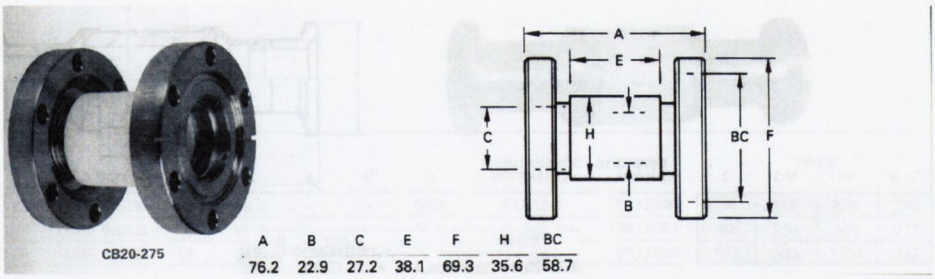

Fig. 6.4 Schematic of the commercially available CF connector flange which was modified for use in construction of the small anode plasma source. The separator in the photo is AlN ceramic.

Although this configuration proved to be quite robust, the plasma jet was noticeably less intense than observed with device #1. This is most likely due to the source dimensions,

which in comparison with the first device show a greater electrode separation and, most importantly, a smaller cathode area (see table 6.1 below). While it was possible to reduce the electrode separation by fixing an aluminium tube to the cathode, this in effect only reduces the breakdown voltage (see appendix V), whereas the cathode area determines the total secondary electron current which can be extracted from the cathode in a normal glow discharge [Chapman, 1980a].

Parameter	Device #1	Device # 2
s (cm)	5	7.6
A (cm^2)	9.6	5.7

Table 6.1 Comparison of electrode separation (s) and cathode area (A) in the small anode discharge sources built using the aluminium/quartz tube (device #1) and adapter (device #3) designs.

Although the pressure in the source could not be measured directly, a gauge was connected to the input N_2 line, approximately 10 cm from the cathode (see figure 3.2), and the readout compared with the pressure in the deposition chamber. Typically, the pressure required to establish a steady discharge was ~ (3-10) mbar, and the breakdown voltage was in the range (600- 800) V. By comparing with the Paschen curve in appendix V, it is clear that the discharge was not operating near the pressure-distance minimum (i.e. the minimum breakdown voltage in the N_2 Paschen curve is at ~ 400 V, when the $p \times d$ product is 10 mbar mm).

6.3.3 Plasma characteristics of small anode discharge

The plasma generated by the small anode discharge was characterised using a cylindrical ion probe (ϕ=0.13mm, l=5 mm) with the *SmartProbe* system (see section 3.4.1.2).

Figure 6.6 shows the variation in ion current collected by the probe and the corresponding ion and electron densities calculated by the Smartprobe system. The values are over an order of magnitude lower than those reported for a similar device used in plasma assisted MBE of GaN [Anders and Anders, 1995]. The reduction in the measured

ion current falls off faster than $1/d_A^2$, where d_A is the distance from the anode (the actual power dependence lies between 2.5 and 3) suggesting that recombination processes may be significant.

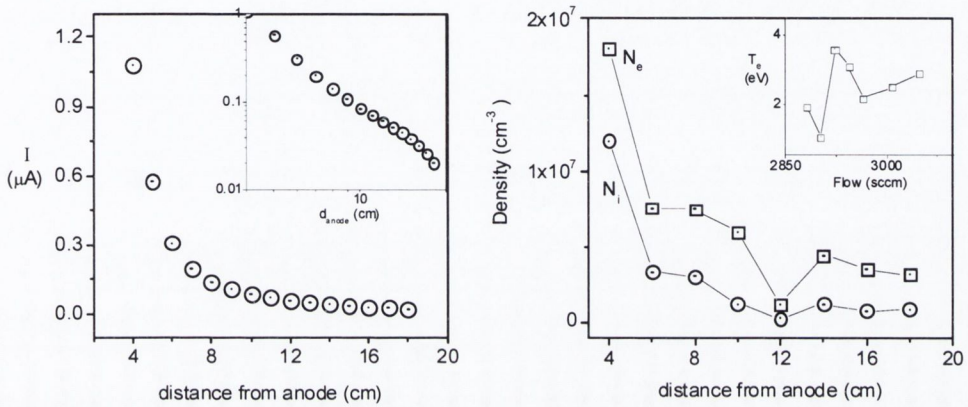

Fig. 6.5 (a) Variation of ion current (left) and (b) particle density (right) with distance from the small anode measured using the Smartprobe system. The inset (left plot) shows the ion current plotted on a log-log scale. The variation of electron temperature with gas flow to the source is also included (inset, right).

The considerable fall-off in ion density over the first 7 cm makes the source somewhat inefficient in this position, considering that the target-substrate region is about 14 cm from the anode. A number of alterations were made to the setup to try to reduce the source-target separation, but in each case, the cathode cooling requirements limited the positioning options. The ion and electron densities in figure 6.8(b) differ by almost half an order of magnitude, which is unexpected considering that the measurements were taken well away from the anode sheath, in the absence of any large electric field gradients. The reason for this discrepancy is not clear, but may be due to the fitting procedure in the Smartprobe software, since no correction was made for the flow velocity of the plasma.

6.4 Hollow Cathode Plasma Electron Emitter (HCPEE)

6.4.1 Operational features

As outlined briefly in section 3.2.3.2, the operational principle of the HCPEE is somewhat different to the small anode discharge. The source of electrons is a tubular device (see figure 6.7) heated to temperatures in excess of 1000 °C, and the electron emission process is thermionic rather than via electrode bombardment (secondary electron processes).

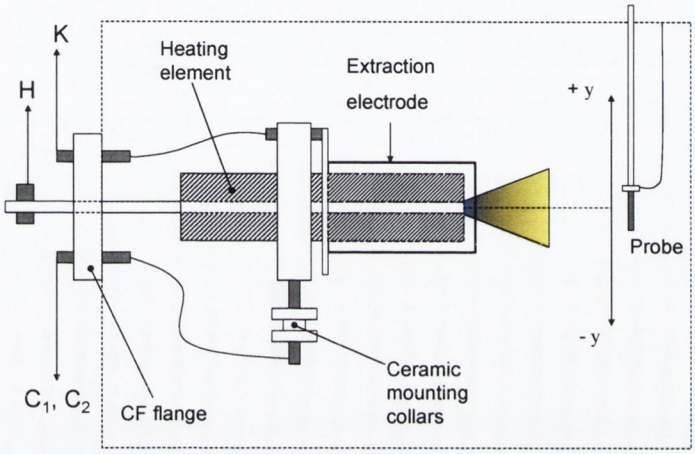

Fig. 6.6 Schematic of HCPEE indicating the power supply connections (H, C_1 and C2) and the extraction ("keeper") electrode connection (K). The ion probe used in plasma characterisation measurements was free to move in the vertical (y) plane, along the target-substrate axis.

As a result, heating induced effects play a huge part in the device performance. After several successful runs during which the plasma was characterised using the Smartprobe setup, the source failed to strike a discharge[45], and plasma-assisted deposition with the HCPEE was limited to just a few film growth runs.

[45] A common fault with this type of heating device is corrosion due to a low purity feed gas. For the HCPEE, the impurity level must be less than 1 ppm. In this case, the fault was due to contact being established between the extraction electrode and the tube which occurred over time as heating caused the electrode to droop downwards onto the element.

6.4.2 Plasma characteristics of the HCPEE

Plasma characteristics of the HCPEE were mapped along an axis perpendicular to the plasma flow, as illustrated in figure 6.6 above. This axis was 4 cm from the exit orifice of the source, and passed through the substrate position (y = 0).

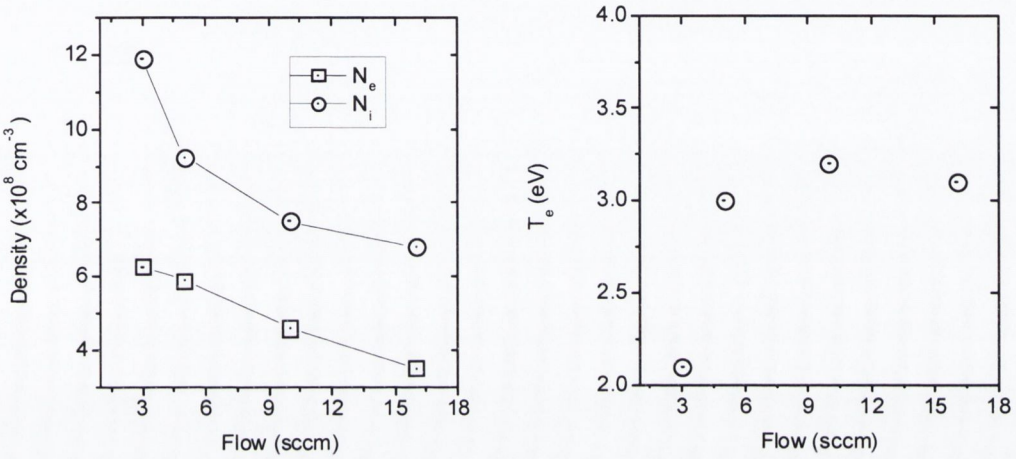

Fig. 6.7 Electron and ion density (left) and electron temperature measured using the Smartprobe system along the target-substrate axis, 4 cm from the HCPEE. The gas flow rate for all measurements was 8 sccm.

Figure 6.7 shows the variation along this axis of the electron and ion density as well as the electron temperature at an N_2 flow rate of 8 sccm. The data indicates a strongly forward peaked distribution in all cases, but most importantly, the ion density is at least an order of magnitude greater than that measured with the small anode source. The variation of density and temperature with N_2 flow to the HCPEE is illustrated in figure 6.8. The unit is designed to operate with a user external anode to provide dense plasma- which can be maintained by the unit's electron emission current-downstream from the HCPEE. The device manufacturers suggested using a water-cooled ring as an anode and to bias the common on the HCPEE power supply to about – 30 V with respect to this ring (which was grounded). Unfortunately, the device failed before it was possible to establish whether this configuration leads to a higher ion density at the centre of the ring and to test

its suitability for film growth. However, a film growth was carried out using the original configuration (section 6.6).

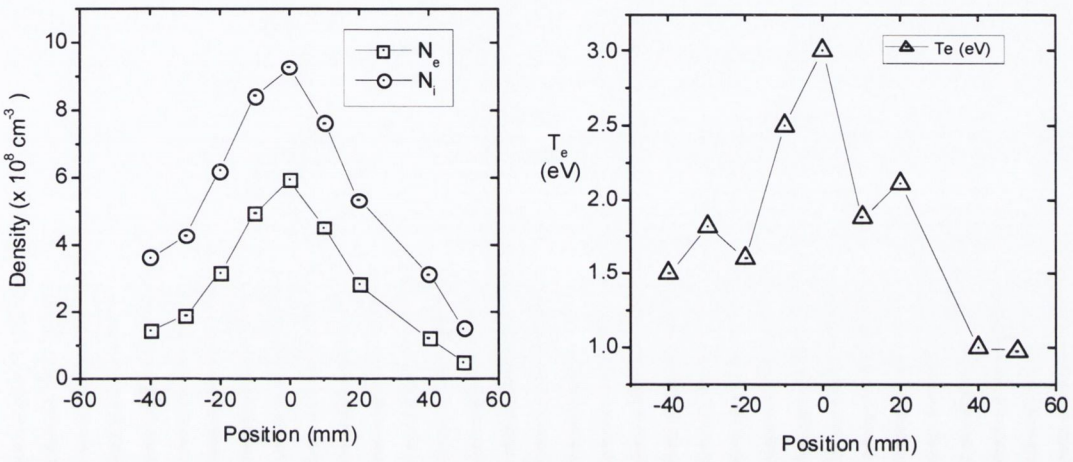

Fig. 6.8 Characteristics of the HCPEE plasma as a function of N_2 gas flow. The measurements were taken directly in front of and approximately 4 cm downstream from the source opening.

6.5 Pulsed discharge

6.5.1 Overview

The pulsed discharge configuration is simplest arrangement (both in terms of the electrical configuration and construction materials) of the three discharge sources tested in this work, as indicated by the experimental setup illustrated in figure 3.5. Its time-averaged input power is also much less in comparison with the steady state discharges, thus the problems associated with heating induced damage are effectively avoided. Despite these advantages, the use of a high voltage electrode within the deposition chamber invariably leads to arcing and possibly to sputtering of the film. It was found that at (0.05-0.1) mbar and a ring voltage of at least 100 V, plasma emission was clearly visible around the ring once the laser produced plasma was generated (discharge was also evident by a jump in the current and voltage gauges on the source).

6.5.2 Discharge profiles for the ring electrode

The current discharged by the capacitor in the charging circuit (chapter 3, figure 3.5) was determined by noting the voltage drop across a small resistor (0.3 Ω) in series with the capacitor. The discharge profiles for the ring at positive and negative charging voltages are presented in figure 6.9. In all cases, an increase in charging voltage leads to an increase in discharge current.

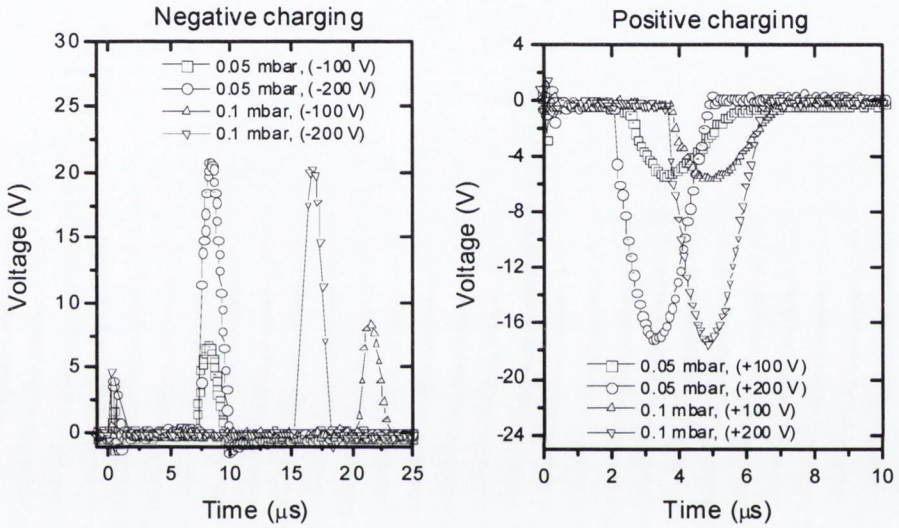

Fig. 6.9 Discharge profiles for the ring electrode measured using a small resistor in series with the charging capacitor.

The effect of background gas pressure on the temporal behaviour of the discharge is interesting; for both positive and negative charging, the increase in pressure delays the discharge onset (see table 6.2). However, for negative charging at 0.1 mbar, it seems that the time at which the discharge takes place is also dependent on the charging voltage. Furthermore, discharge takes place at earlier times when the ring is positively charged, presumably because electrons reach the electrode at earlier times when biased positive in comparison with positive ions when biased negative. Such variation in temporal behaviour will have important consequences for film growth, and synchronisation of the discharge duration with the plume arrival period to the substrate is likely to promote nitridation of any free gallium.

p (mbar)	V (Volt)	Q_e (μC)	C×V (μC)	τ_{max} (μs)	FWHM (μs)
0.05	-100	30.2	47	8.0	1.4
0.05	-200	101.4	94	8.2	1.7
0.05	100	40.7	47	3.6	2.1
0.05	200	102.3	94	3.2	1.8
0.1	-100	41.0	47	21.6	1.4
0.1	-200	114.3	94	16.8	1.4
0.1	100	41.3	47	4.7	2.2
0.1	200	104.0	94	4.9	1.8

Table 6.2 Comparison of the integrated charge (Q_e) determined from the discharge current profiles in figure 6.14 and the charge stored on the capacitor ($Q=CV$). Also included is the time (τ_{max}) corresponding to the peak voltage and the FWHM of the discharge profile.

Considering that the time of flight for the ionic component of the plume to a substrate, typically at 4 cm, in 0.1 mbar is about 5 μs when using a fluence of a few J cm^{-2} (e.g. see figures 4.8 and 5.9), it seems that positive charging is more suited to synchronisation of the discharge with the arrival of the ions. In any case, the timing of the discharge appears to vary greatly with background gas pressure when the ring is negatively biased. The total charge stored by the capacitor (Q), which is given in terms of the capacitance, C, by $Q=CV$, is compared with the time integral of discharge current in table 6.2.

6.5.3 Ion probe characterisation of the pulsed deposition environment

Since this type of discharge takes place over a relatively short duration (≤ 100 μs), the Koopman circuit rather than the Smartprobe system (section 3.4.1) was used in conjunction with an ion probe to monitor the plasma behaviour. The probe was shielded using a grounded metallic mesh or cup (i.e. a Faraday cup) to prevent a discharge from being setup between the ring and probe (see fig. 6.10 below).

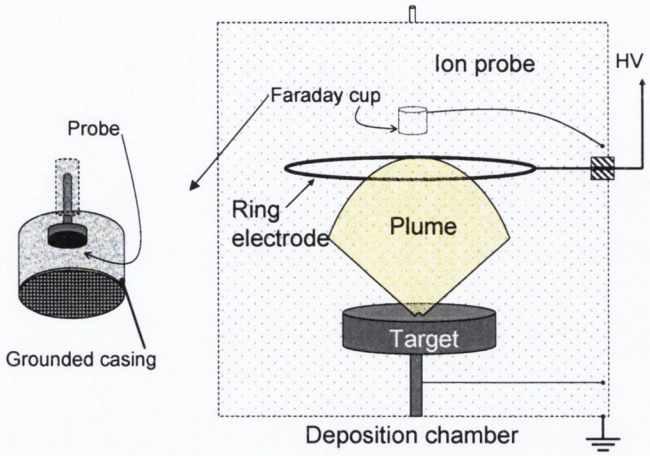

Fig. 6.10 Schematic of ring electrode and ion probe configuration used for characterising the pulsed discharge environment. The probe was encased in an electrically grounded stainless steel cage (Faraday cup) and was biased at -30 V for all measurements (the complete details of the electrical circuit are outlined in figure 3.5).

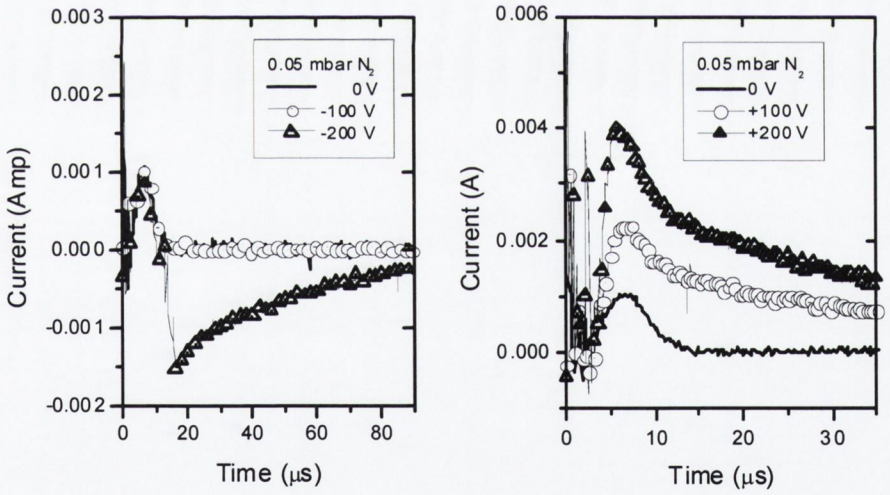

Fig. 6.11 Ion probe TOF signals for Ga target ablation in 0.05 mbar N_2 at negative (left) and positive (right) charging voltages. The probe was negatively biased with respect to ground (-30 V) in all cases (d=7 cm).

Figure 6.11 shows the ion probe TOF signals for ablation in 0.05 mbar N_2 at positive and negative charging voltages. In all cases the probe was biased at -30 V to repel electrons and to detect the positive ion contribution in the plasma (target – probe distance = 7 cm). The profiles indicate a dependence on charging voltage for both the TOF and type of

charge collected, similar to the behaviour observed in discharge profiles (fig 6.9). Unlike the probe signals for a positively charged ring (right), a negative current is detected when the charging voltage was increased to -200 V in 0.05 mbar. This is somewhat surprising since the probe is negatively biased with respect to the grounded casing, though it is positively biased with respect to the ring ($V_{probe\text{-}ring}$= +170 V). Therefore, the negative swing in the probe signal is most likely due to a discharge being established between the probe and the ring. This potential difference is too low to breakdown molecular nitrogen in its ground state (recall the minimum of the Paschen curve is at ~ 350 V, appendix V), indicating that the gas is already been ionised to a significant extent (most likely due to fast electrons) before the main ring discharge takes place.

At 0.1 mbar (figure 6.12), the signals show a similar trend, with the TOF at negative charging depending on the charging voltage, while for positive charging, the variation is in the magnitude of the signals alone.

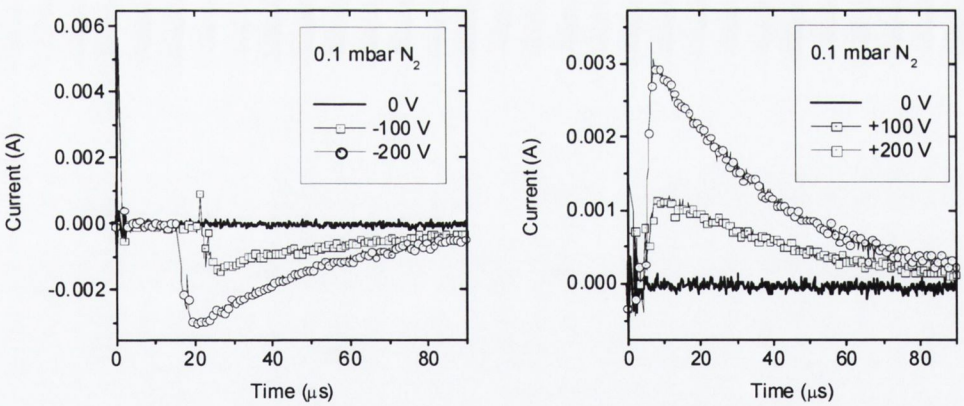

Fig. 6.12 ion probe signals for Ga target ablation in 0.1 mbar N_2 at negative (left) and positive (right) charging voltages. The ion probe signal in the absence of a charged ring was too small to detect at this distance (7 cm) and fluence (1.5 J cm^{-2}).

At negative charging, only a negative current is detected by the probe. Therefore, it is not possible to draw any conclusions regarding the dynamics of the positive ionic component of the plume since the probe signal seems to be dominated by the probe-ring discharge.

An interesting feature of the TOF signals for positive ring charging is the duration over which an ion current is detected. While an ion current is detected for ~ 10 μs without the ring discharge, this duration is extended several times once the ring is charged to a few hundred Volts. This feature is illustrated most effectively in the case of ablation at 0.1 mbar, where a significant ion current is detected with the discharge while there is negligible signal without (the grounded cage and increased distance leads to very little charge reaching the probe at 0.1 mbar). It still remains unclear as to whether the plume or background gas (or both) are being ionised, but in any case, the technique provides an efficient means of supplying energy to a deposition environment where medium to high background gas pressures would otherwise reduce the kinetic energy of the plume.

6.6 Plasma-assisted PLD of GaN

A number of film growth experiments were carried out to test the suitability of the three plasma sources, in PLD of GaN. Using optical reflectivity, the growth rates of films grown with the various plasma sources were compared with those of films grown under similar conditions using molecular nitrogen. The following sections summarise the primary film growth results, with emphasis again placed on the growth rate and crystalline quality of the material.

6.6.1 Film growth with the small anode discharge

The small anode discharge source was used in conjunction with a gallium target, and operated at a flow which resulted in a chamber pressure of (0.1-0.3) mbar (deposition was carried out using a fluence of 1.5 – 4 J cm^{-2}). As was observed when using N_2, a limiting gas pressure of ~ 0.2 mbar and fluence of ~ 3 J cm^{-2} determined whether growth took place or not, but no significant difference in the actual growth rate was noted when compared to growth in N_2. Likewise, the crystalline properties of the films grown using the small anode source showed little difference compared with those grown in N_2. In fact, the substrate temperature was again the critical factor which determined whether the films were highly oriented along the c-axis or poorly polycrystalline. Thus it would seem that in its present state of operation, the small anode source presents no significant advantage over N_2 in PLD of GaN.

6.6.2 Film growth with the HCPEE

While the temperamental nature of the HCPEE limited its use in film growth to just a few deposition runs, both the reflectivity and XRD results for these films showed that the source may be quite suitable for plasma assisted-PLD of GaN. The HCPEE was used in conjunction with a GaN target, and at a gas flow of 20 sccm which corresponded to a background gas pressure of 0.05 mbar N_2. At a fluence of 2.5 J cm^{-2}, reflectivity measurements showed an increase in the growth rate from 0.06 to 0.08 nm per shot. Perhaps more importantly, XRD (figure 6.13) revealed that the grain size for the film grown using the HCPEE was nearly 50 % greater (41 nm compared to 27 nm) than that of the film grown in N_2.

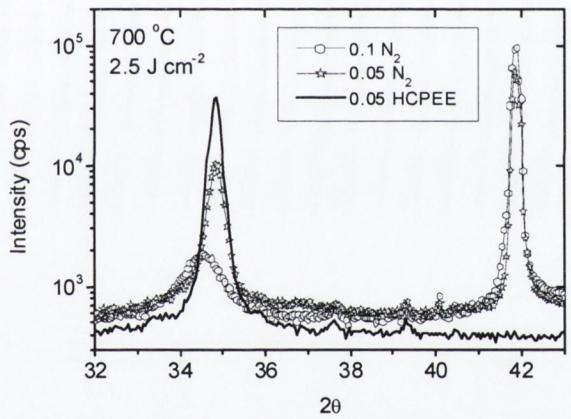

Figure 6.13 XRD scans of the GaN (0002) peak for films grown on sapphire at 700 °C using a GaN target with the HCPEE (solid line) and N_2 (line & symbol). The target-substrate distance was 4 cm.

6.6.3 Film growth with the pulsed discharge

While the pulsed discharge was used in conjunction with both Ga and GaN targets, it proved most effective with the Ga target where it was shown to promote strong c-axis growth at a pressure as low as 0.1 mbar (recall that the crystalline quality of films grown in 0.1 mbar N_2 was quite poor, while the growth rate was extremely slow). Figure 6.14a shows the XRD scan of a film grown at 700 °C (3 J cm^{-2}) using the ring electrode which was charged at +200 V. The film appears to be highly oriented and the $(10\bar{1}0)$ or $(10\bar{1}1)$

peaks observed in scans of films grown in molecular nitrogen are absent. Despite this noticeable improvement in crystalline quality, the grain size (26 nm) corresponding to the (0002) peak width is significantly less than the largest values obtained using the GaN target (> 40 nm). Interestingly, the reflectivity for this film growth suggests considerable surface roughness, as indicated in figure 6.14b.

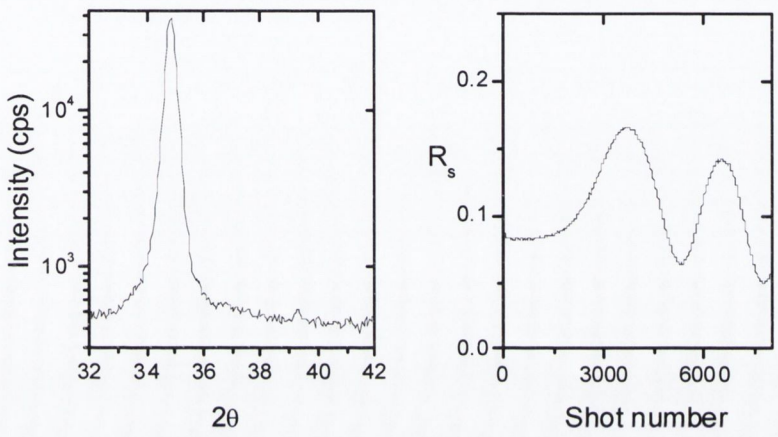

Fig 6.14 Structural and optical characteristics of a film grown using the pulsed ring discharge and a Ga target in 0.1 mbar N_2 (T_s=700 °C, fluence = 3 J cm^{-2}). (a) XRD scan showing a strong c-axis orientation and (b) reflectivity[46] for the growth period indicating considerable surface roughness. For a comparison with GaN growth from a Ga target (which required at least 0.2 mbar N_2) see figures 5.14 and 5.15 in chapter 5.

6.7 Conclusions: device suitability for GaN growth

This chapter has attempted to identify a suitable means of providing excited and ionised nitrogen species for PLD of GaN. Though the range of conditions investigated were somewhat limited, both the plasma characteristics and film properties highlight the advantages as well as the drawbacks associated with each source:

- With the small anode discharge, the flux is greatly affected by the cathode-anode ratio which must be maximised to obtain a considerable increase in the anode sheath. In its present configuration, the ion flux measured at the substrate position

[46] This film was grown on double side polished sapphire; thus the amplitude of oscillation differs from previous results.

appears to be too low to considerably improve either the growth rate or crystalline quality of films grown from a Ga target.

- The HCPEE source provides a considerable flux of ions to the substrate region as evidenced by the Smartprobe measurements. Since the discharge runs at only a few volts, it is also suitable for providing ions and excited neutrals with low kinetic energy. However, high purity gas requirements and heating induced damage limit its effectiveness in its present configuration.
- The pulsed discharge appears to provide a sufficient degree of background gas activation to promote GaN growth from the Ga target at significantly lower pressures than those required for growth in molecular nitrogen. The average power consumption of the pulsed discharge is considerably less than that of the other sources, thus avoiding problems associated with heating induced damage, while at the same time being long enough to extend well beyond the arrival duration of the ionic component of the plume to the substrate. The discharge is better synchronised with the arrival of the plume when the ring is positively charged, and therefore better suited to plasma-assisted film growth when this charging polarity is used.

The use of a pulsed discharge offers a distinct advantage over continuous operation in that heating induced damage is considerably limited. It is also an efficient means of synchronising the nitrogen and gallium fluxes. Despite the effort invested in construction and characterisation of the small-anode source, it seems clear that in its present configuration it is not operating efficiently. If the flux output from the small anode source can be optimised, then it may be worth investigating the possibility of running the discharge in pulsed mode to reduce heat generation at the cathode.

7. PLD of GaMnN

Introduction

Diluted magnetic semiconductor (DMS) growth has recently become an area of intense research with the aim of developing room temperature semiconductor-based spin-transport electronic (spintronic) devices for regulating the flow of spin-polarised current [Ball, 2000]. The growth of DMS materials involves doping a semiconductor like GaAs or GaN with small concentrations of a transition metal such as Mn or Fe, however the thermal equilibrium solubility of Mn in III-V semiconductors is less than 1 % [Tanaka, 1998], whereas higher concentrations[47] are predicted to be necessary for room temperature ferromagnetic behaviour in GaMnN [Dietl et al., 2000] and AlMnN [Litvinov and Dugaev, 2001]. Reed et al. [Reed et al., 2001] have succeeded in obtaining room temperature ferromagnetic GaMnN films; they used PLD to deposit a Mn layer on MOCVD-grown GaN and annealed the sample at 250 -800 °C and obtained ~ 1% Mn films which showed hysteresis at 300 K. Recently, Hori et al. [Hori et al., 2002] have grown single phase GaMnN films with up to 5% Mn, using low-temperature MBE and have observed ferromagnetic behaviour at temperatures as high as 700 K. It may also be possible to incorporate such comparatively high Mn concentrations in PLD-grown DMS films using magnetically doped targets, as the PLD film growth process is often far from equilibrium [Fukumura et al., 1999]. Much interest has been generated by recent reports of high temperature ferromagnetism in various doped wide bandgap oxides grown by PLD, in particular, the observation of a giant Co moment in Co-doped tin oxide [Ogale et al., 2003]. Although, similar high temperature ferromagnetic behaviour has yet to be reported in PLD-grown magnetically doped nitrides, it seems that PLD is a promising technique for the growth of these materials.

This work serves to establish whether PLD can be used to achieve the 5% Mn concentration required for room-temperature ferromagnetism without separation into any

[47] Concentrations are generally quoted in atomic rather than mass per cent; the same convention is adopted for this chapter.

number of manganese nitride or manganese gallium phases identified in GaMnN samples prepared by some of the more conventional film growth techniques (as discussed in section 7.1.2). Before discussing the characteristics of both the Mn-doped targets and films, some properties of Mn and its nitrides are firstly considered.

7.1 Properties of manganese and its nitrides

7.1.1 Properties of Mn

Mn is a transition metal which is widely used to strengthen steel and to create highly ferromagnetic alloys, though pure Mn metal is brittle and is antiferromagnetic[48] [Ching et al., 1995]. Mn has a cubic structure (a_0=8.91 Å) and while it has a much higher melting temperature (1245 °C) than gallium (29.8 °C), its boiling point is lower at 2100 °C (vs 2227 °C for Ga). The heat of vaporisation (280±10 kJ mol^{-1})[49] for Mn is slightly greater than that of Ga (264 kJ mol^{-1} [Geiger et al., 1987]) as is the vapour pressure over Mn (figure 7.1).

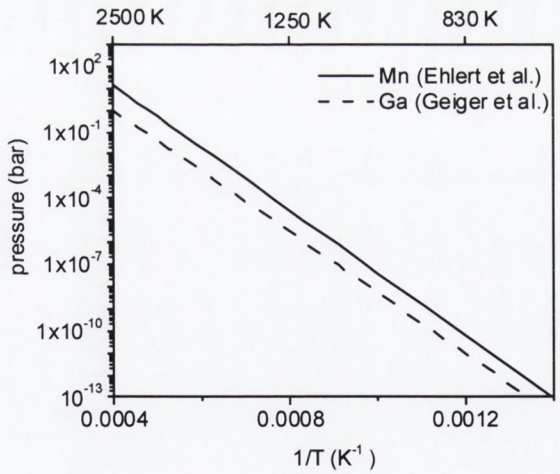

Fig. 7.1 Vapour pressure over Mn calculated using heat of vaporisation measured by Ehlert [Ehlert, 1969]. Also included (dashed line) is the vapour pressure over Ga [Geiger et al., 1987], as presented in figure 1.5.

[48] At room temperature, Mn behaves paramagnetically, since its Néel temperature is ~100 K [Ching, 1995].
[49] There is some variation in the reported values of the heat of vaporisation for Mn, ranging form (270-290) kJ mol^{-1}; this is discussed in greater detail in [Ehlert, 1969].

Manganese is known to take a number of valence states in crystals, but most often is +1 or +2 in nitride compounds (see table 7.1 below for ionic radii). Its first ionisation potential is 7.4 eV which is higher than that of Ga (6 eV).

Valency	R_{Mn}(Å)	R_{Ga}(Å)
+2	0.67	
+3	0.58	0.47 {0.62}
+4	0.39 {0.53}	

Table 7.1 Ionic radii in crystals for some of the valence states of Mn and Ga [Lide, 1998] of coordination number (CN) = 6 {the values in curled parentheses are for CN=4}.

7.1.2 Manganese nitride

Manganese is known to form a number of bulk nitride phases which vary in Mn:N ratio from the stoichiometric MnN (θ) phase to the Mn-rich Mn_4N (ε) phase [Takei et al., 1962; Suzuki et al., 2000]. Intermediary crystalline compounds which have also been identified include Mn_3N_2 (η phase) and Mn_5N_2 or Mn_2N (both of the latter belong to the ξ phase). The θ and η phases form face-centred tetragonal structures [Yang et al., 2002], while the ε phase is face-centred cubic [Takei et al., 1962]. The stability of the various phases was shown by Suzuki et al. [Suzuki et al., 2000] to be strongly temperature dependent. They annealed MnN at temperatures ranging from 670 – 1180 K and noted that as the temperature was increased, so was the Mn:N ratio, eventually resulting in Mn_4N, once a temperature of 1068 K was reached. This trend of using higher preparation temperatures in order to obtain a higher Mn:N ratio is reported elsewhere [Mah, 1958]. While it is difficult to compare the reactivity of gallium and manganese with nitrogen it is interesting to note that Mn_4N can be prepared from heated (1200 K) Mn powder under a flow[50] of N_2 [Mah, 1958]. Nitridation of Ga using N_2 under similar conditions has not been reported, and GaN crystal growth (~0.1 mm per hour) requires temperatures in excess of 1600 K and N_2 pressures of 15-20 kbar [Grzegory et al., 1993].

[50] Although not specifically stated in the report by Mah, this was presumably near atmospheric pressure. The preparation time was 31 hours.

There are a number of further points concerning Mn and its nitride which are likely to have particular relevance to GaMnN thin film growth:

- The unit cell of the Mn_4N phase consists of six strongly bonded divalent Mn (II) face-centred atoms and the corner sites are occupied by eight univalent Mn (I) atoms [Takei et al., 1962], which can be relatively easily substituted by Ga to form compounds of the form $Mn_{4-x}Ga_xN$ [Garcia et al., 1983a].
- Mn_4N is ferromagnetic with quite a high Curie temperature (756 K) [Garcia et al., 1983b]. The θ and η phases are considered to be antiferromagnetic, with Neel temperatures of 650 K [Suzuki et al., 2000] and 925 K [Tabuchi et al., 1994] respectively.
- The solubility of nitrogen in liquid Ga can be increased by adding small amounts of Mn to the molten metal [Kelly et al., 2003].

7.1.3 Mn doping of GaN

Efforts to dope GaN with relatively small (1-10 at. %) concentrations of Mn using thermal annealing processes have been hampered by the comparatively low solubility of Mn in III-V structures. For example, Szyszko and co-workers [Szyszko et al., 2001] have shown that the Mn solubility in GaN was limited to 0.9 % when Mn and GaN powders were thermally annealed in an NH_3 flow (they identified MnGa alloys when high Mn concentrations were used). MnGa alloys (particularly Mn_3GaN) have also been identified in samples where the solubility limit has been exceeded [Reed et al., 2001; Thaler et al., 2002]. Using MBE, it was eventually demonstrated that single phase GaMnN growth, with up to 9 % Mn, was possible at a substrate temperature of 750 °C [Overberg et al., 2001; Pearton et al., 2002]. This is a relatively high substrate temperature for MBE growth[51] of GaN [Powell et al., 1993], which is surprising in light of the reports by Ohno et al. [Ohno, 1998], who found that the solubility limit in Mn-doping of GaAs could be increased by depositing at a comparatively low substrate temperature for GaAs epitaxy (~ 250 °C). An important point to note for magnetic applications is the fact that Mn ions

[51] GaN growth by MBE is typically carried out at (400 -700) °C

occupying Ga sites in the GaN lattice act as acceptors (+2 valence state) [Soo et al., 2001] with spin = 5/2 [Zajac et al., 2001].

7.2 Target preparation and characterisation

7.2.1 Powder mixing

The targets used to grow GaMnN thin films were powdered pellets, pressed and sintered according to the procedure outlined in section 3.2.1.1 (12 hours at 700 °C). Manganese nitride powders are not widely available (i.e. commercially); therefore, Mn (99.999%) powder was mixed with the nitride powder (99.99%). The reaction stoichiometry during the sintering process is somewhat unclear, since we are unaware[52] of any thermodynamic data regarding the preparation of GaMnN in N_2. However, from the discussion above, it seems clear that Mn will only be incorporated into the GaN target lattice up to about 1%, and above this value Mn or any of the manganese nitrides (or at high Mn concentrations, a MnGa alloy) are likely to make up the remaining species in the target. In order to maintain a consistent mixing procedure, it was assumed that the reaction proceeded, in terms of the Mn concentration, x, according to the following equation:

$$xMn + (1-x)GaN + \frac{x}{2}N_2 \rightarrow Ga_{(1-x)}Mn_xN \qquad \text{(eq. 7.1)}$$

Three targets were prepared, using Mn atomic fractions (x) of 0.02, 0.05 and 0.1 in the initial powder mix. Although a ceramic target was used for all of the GaMnN film growth experiments to date, a MnGa metallic mix has also been recently prepared[53] which consists in 5% Mn in Ga. Mn is relatively insoluble in Ga (at room temperature, Mn solubility in Ga is ~ 1-2% [Massalski, 1990]), and an ultra-sonic bath was required to bring the Mn into solution with liquid Ga at about 100 °C.

---

[52] Mn_3GaN has been prepared in N_2, but using manganese nitride ($Mn_{2+x}N$), Mn and Ga powders [Garcia et al., 1983a].

[53] This alloy was prepared by David Doyle at the chemistry department, Trinity College Dublin.

7.2.2 EDAX measurements on targets

After the pressed pellets were sintered, the Mn:Ga ratio at different regions of the target surface was measured using energy dispersive X-ray analysis (EDAX, see 3.4.3 for equipment details). From figure 7.2, it seems clear that while at 2% Mn the measured values agree reasonably well with the initial mix, there is considerable variation in the Mn:Ga ratio at the largest concentration of 10% indicating that homogeneous mixing is not occurring at the higher mixing concentrations. It is unlikely that sintering at 700 °C has the desired effect of providing Mn atoms with sufficient energy to diffuse through the target (recall the decomposition temperature limits discussed in section 3.2.1.1). The limited nature of the sintering process is further evidenced by the density of these targets, which was again well below the single crystal value (~60 %). Therefore, unless a high pressure sintering facility is available, sintering under these conditions is likely to achieve little more than a slight improvement of the mechanical strength of the pellet.

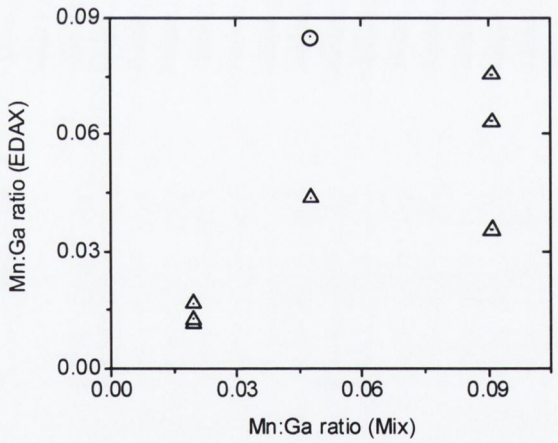

Fig. 7.2 Comparison of Mn:Ga ratio in sintered targets to the Mn:Ga ratio in the initial target mix for targets prepared with 2, 5 and 10 at.% Mn powder. The measurements (triangles) were carried out on freshly sintered targets, except for one analysis (circle) of the laser track, i.e. ablated, region.

7.2.3 XRD analysis of targets

The target powders, both before and after sintering, were analysed using X-ray diffraction (XRD) in the θ-2θ configuration. Figure 7.3 compares the XRD scans for Mn doped targets with the patterns of the pure GaN and Mn powders used in preparing the mix.

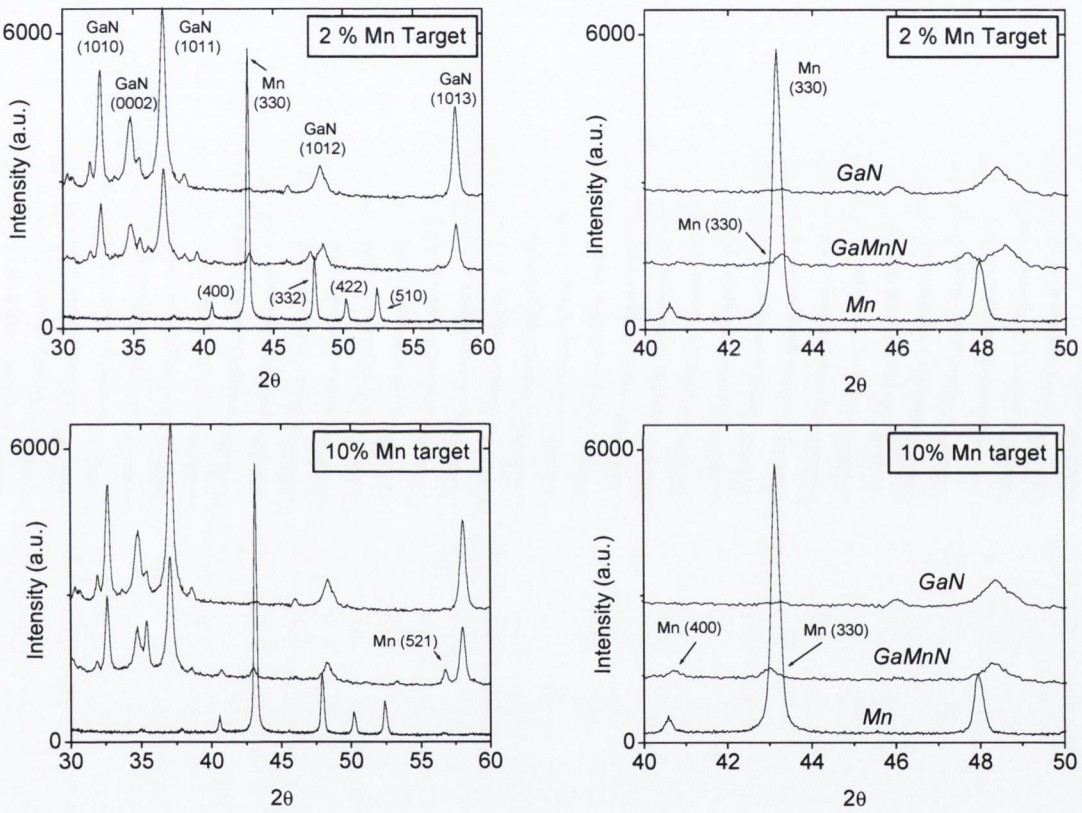

Fig.7.3 X-ray diffraction patterns for the various powders used in GaMnN target preparation. In each plot the top, middle and bottom scans are for GaN, GaMnN and Mn powders, respectively. The plots on the right hand side show the emergence of Mn peaks in the range 2θ = (40-50) degree.

In both cases, the Mn doped targets show traces of Mn, i.e. the (330) peak, indicating that Mn has not been completely incorporated into the lattice (these scans were taken using powders which were scraped from the target surface). While a change in lattice parameter

would be expected for the doped powders compared with pure GaN, at least up to the solubility limit (~1% Mn), no significant shift was measured in the corresponding peak positions.

7.3 Characterisation of the deposition environment

7.3.1 Ion probe measurements

The plasma characteristics of the deposition environment for ablation of pure and doped (10 % Mn) targets in high vacuum were monitored using the Langmuir ion probe setup outlined in 3.4.1.1. The integrated ion flux per shot and the velocity associated with the maximum ion flux in high vacuum (as a function of fluence) extracted from the ion TOF signals are plotted in figure 7.4.

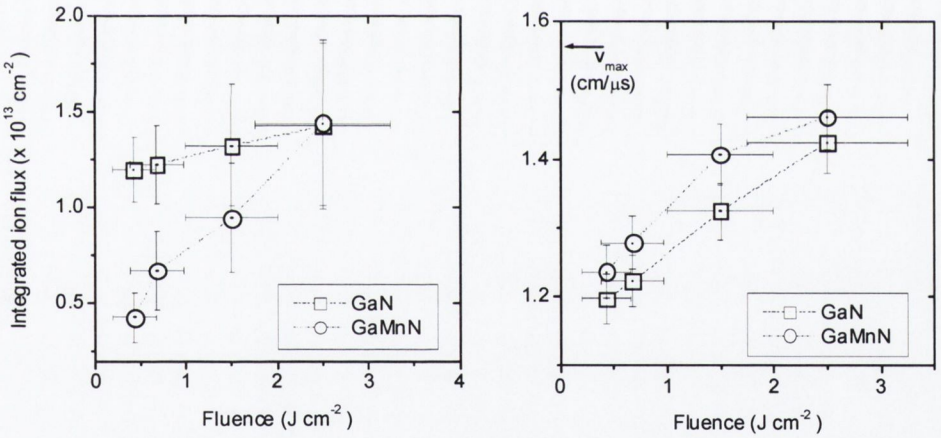

Fig. 7.4 (a) Total integrated charge collected by the probe per shot at various fluences (left) and (b) velocity (corresponding to the maximum ion flux) increase with laser fluence for GaN (squares) and Mn doped (10%) GaMnN (circles) targets. The velocity (rather than the ion energy) has been plotted, since the identity (and thus the mass) of the ions is not known.

There appears to be a significant difference in the integrated flux near the ablation threshold, which might be related to the higher ionisation potential of Mn (section 7.1.1). While the ion velocity (associated with the maximum ion flux) for GaMnN target ablation was marginally higher than the GaN target case (figure 7.4b), the uncertainty in

the target-probe distance (± 1 mm) could account for this discrepancy. Nevertheless, the ionic mass difference may be a significant factor in determining the ion velocity $\left(m_{Ga}/m_{Mn} = 1.2\right)$ as has been observed in laser ablation of multi-component compounds [Geohegan, 1994].

7.3.2 Reflectivity analysis of GaMnN growth on sapphire

Optical reflectometry was used to monitor the optical properties and growth rate of films grown from Mn doped targets (see section 3.3.2 for details of the reflectivity setup). The target substrate distance, fluence and background gas pressure were maintained at the same values used in growth of pure GaN. Thus, these measurements allow us to make some direct comparisons on the effect of introducing Mn to the films.

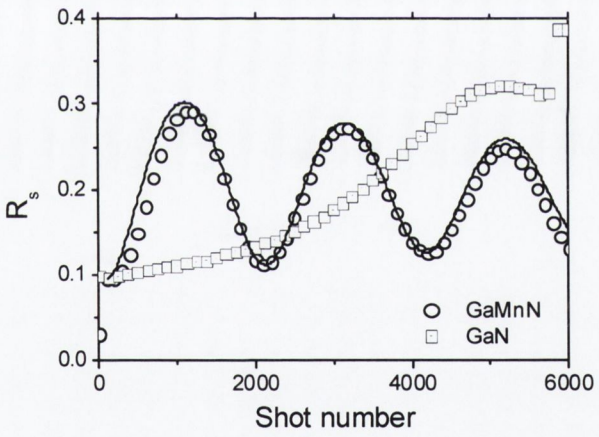

Fig. 7.5 Reflectivity for a film grown at 800 °C from a 10% Mn target (circles) in 0.1 mbar N_2 at 2.5 J cm^{-2}, and the fit (solid line) which yields a growth rate of 0.07 nm per shot. Also included is the reflectivity for a GaN film (squares) grown at 750 °C using the same fluence and gas pressure. The fit to this data yielded a refractive index of $\hat{n}$ =2.38-*i*0.08.

In general, the reflectivity signals showed little change in comparison with the undoped GaN growth, particularly when using the targets with lower Mn concentration (<5%). However, some of the Mn doped films showed stronger absorption at the reflectivity wavelength; this was most noticeable in a film grown from the 10 % Mn target in 0.1

mbar N_2, as illustrated in figure 7.5. This film was grown at a comparatively high temperature of ~ 800 °C[54] and, in addition to the increase in optical absorption noted already, the growth rate seemed exceptionally high for these deposition conditions (0.1 mbar N_2, 2.5 J cm^{-2}) and substrate temperature. The increase in both the optical absorption and growth rate is most likely due to the high concentration of Mn in the film which, using EDAX, was measured as 25% (see next section for details). Mn incorporation in InMnAs was shown to reduce the bandgap and resulted in a red-shift (by ~ 50 meV) of the absorption spectrum [Munekata et al., 1989]. The luminescence of novel "Spin-LEDs[55]" fabricated with a GaMnN layer was also considerably reduced in comparison with non-magnetic devices [Polyakov et al., 2003].

7.4 Post growth characterisation of GaMnN thin films

7.4.1 EDAX

Films grown using the Mn doped targets were characterised using SEM and EDAX in the variable pressure mode (see section 3.4.3 for details). Although Al and O from the substrate are likely to be detected (figure 7.6) because the sampling depth is greater than the film thickness, the technique is sufficiently accurate to establish the ratio of the heavier metallic elements, i.e. Ga and Mn, in the film. In general, the films showed higher Mn:Ga ratios than in the target (table 7.3), though the Mn concentration also appeared to increase with substrate temperature.

Target	Film (700 °C)	Film (800 °C)
0.02	0.035	0.05
0.1	0.2	0.25

Table 7.3 Mn:Ga ratio in the target and in films grown at 700 °C and 800 °C.

[54] The reason for using such high temperatures was because of the apparently higher crystallisation temperatures required for Mn doped samples (see section on XRD results).
[55] The phrase "Spin-LED" has been generally associated with LED structures which incorporate a ferromagnetic layer in the multilayer structure. Some degree of control over the output polarisation of the emitted light can be achieved by placing the LED in an externally controlled magnetic field.

The reason for the higher Mn concentration at elevated temperatures is most likely due to the greater tendency for Mn to form a nitride at these temperatures. Otherwise, Mn might be expected to evaporate at a greater rate from the film surface, since it has a higher vapour pressure than Ga at these temperatures (see figure 1.1). The high Mn concentration measured in films grown using the 10 % Mn target may also be responsible for the strong optical absorption observed in the reflectivity traces for these films (figure 7.5).

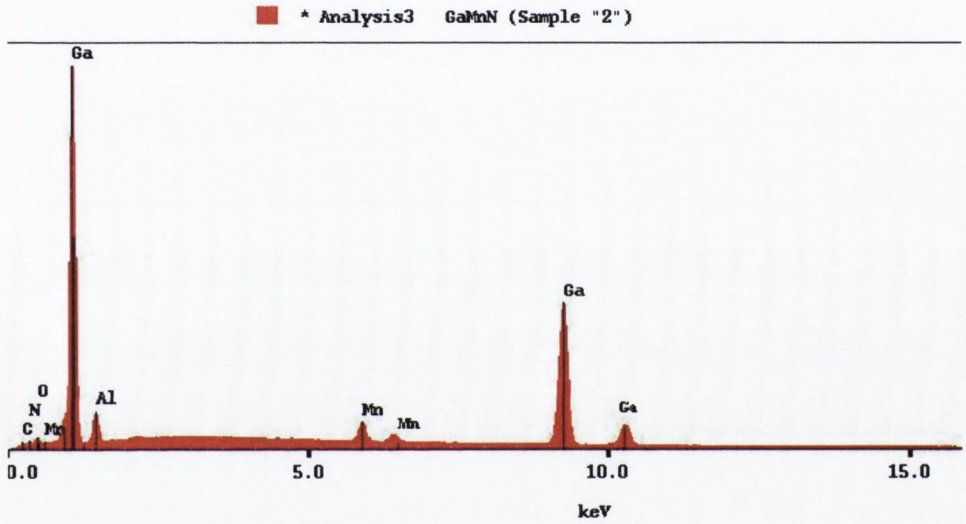

Fig. 7.6 Typical EDAX spectrum for a Mn doped film (this particular film had 5% Mn). Low-*Z* elements are detected at the low end of the energy scale. The Al contribution is from the sapphire substrate, as is most of the oxygen.

In order to establish whether any free Mn was present in the films, as was identified by XRD in the sintered targets, EDAX mapping was carried out on a number of regions of the film. Figure 7.7 shows a map of the three constituent elements (i.e. Ga, Mn and N) of a sample which showed 20% Mn by EDAX analysis. The images are approximately 80×60 microns in area and show no large clusters of Mn, at least on a micron scale. The SEM image also included in this figure (bottom right) indicates that the films have a considerable fraction of micron-sized droplets.

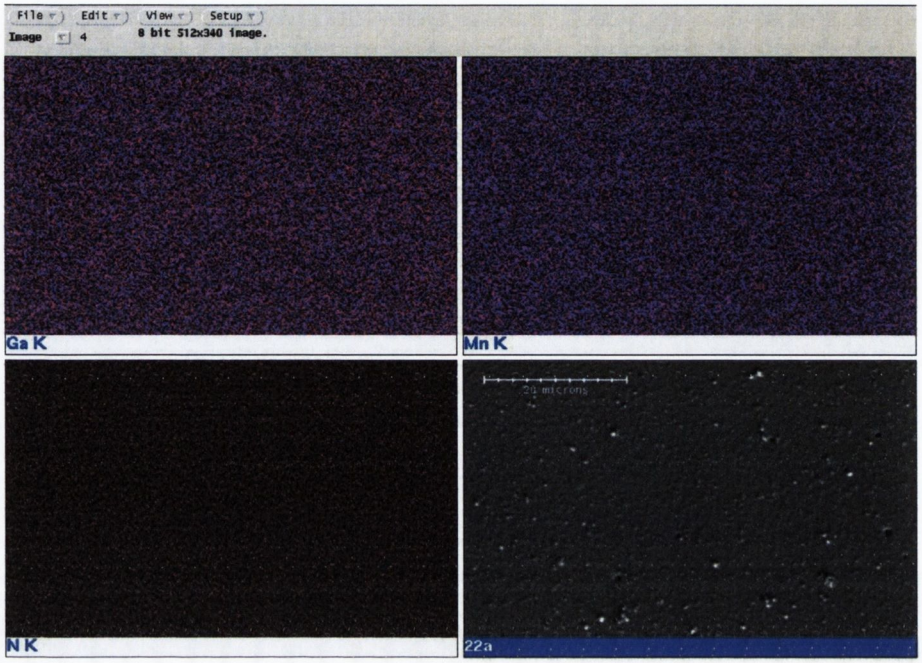

Fig. 7.7 EDAX map of Ga (top left), Mn (top right) and N (bottom left) elements in a film which contained 20% Mn, as measured by EDAX (frame size~ 80 μm × 60 μm). The artificial colour coding allows easy identification of elements (higher concentrations are denoted by brighter colouring). Also included is an SEM image (bottom right) of the mapped region.

7.4.2 XRD

X-ray diffraction measurements of the films grown using the Mn doped targets revealed a strong dependence of the crystalline quality on both the Mn concentration in the films and the substrate temperature used. Figure 7.8 compares the XRD scans of two films grown at 700 °C and 800 °C using the 10 % Mn target with that of a film grown at 700 °C using an undoped GaN target. From these spectra, it seems that a number of unidentified phases are present in the films (labelled A, B and C), although at 800 °C, the (0002) peak associated with c axis GaN growth dominates. The peak is shifted to lower angles by ~ 0.2° from its expected position, indicating an expansion in the lattice perpendicular to the substrate (Δc~0.01 Å), most likely due to the incorporation of the larger Mn^{2+} ion into the lattice structure.

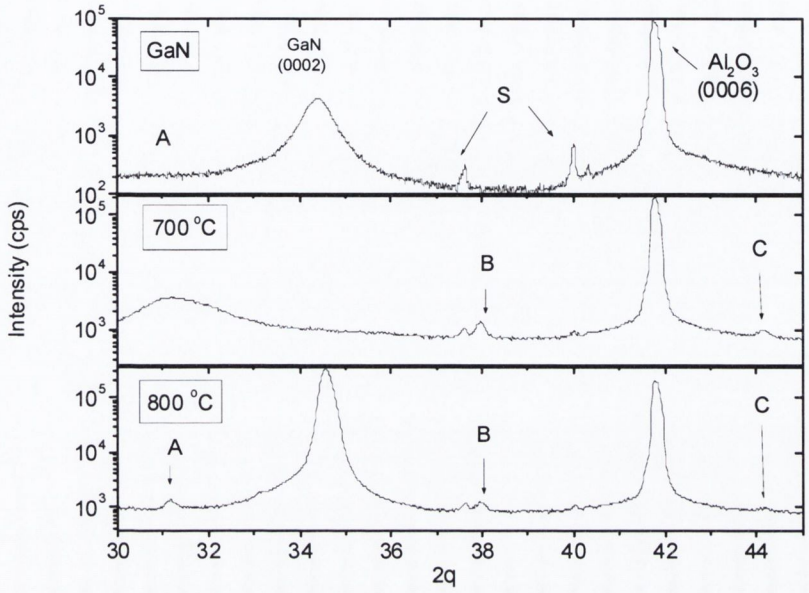

Fig. 7.8 Diffraction patterns for films grown using the 10% Mn target at a substrate temperature of 700 °C (middle) and 800 °C (bottom) in 0.05 mbar N_2 at 2.5 J cm^{-2}. The top panel shows the XRD pattern of a film grown under the same conditions but using an undoped GaN target. The peaks labelled "S" were also observed XRD scans of the substrate. Peaks A, B and C are discussed in the text.

Interestingly, while the films grown at 700 °C using a 2% Mn target show a similar variety of phases and unidentified peaks (figure 7.9), the film grown at 800 °C using the 2% Mn target (5 % Mn in film) only showed a single diffraction near the expected position of the GaN (0002) peak. Presumably, this is single phase GaMnN. The origin of the peaks labelled A to E in figures 7.8 and 7.9 is unclear at this point though "E" may be due the $(10\bar{1}1)$ reflection associated with the wurtzite phase of the nitride. One might expect that these comparatively high temperatures would favour the formation of η-phase Mn_3N_2 or ε-phase Mn_4N nitrides, as observed in MnN annealing experiments (section 7.1.2). However, we were unable to match these unidentified peaks with any of the reported manganese nitride phases, although the data on Mn_4N is in any case somewhat limited. Furthermore, there seems to be some disagreement in the measured value for Mn_4N, with values of 3.865 Å [Takei et al., 1962] and 3.846 (PDF # 01-1202) being

reported for thermally annealed samples. Similarly, Mn_4N films grown on glass substrates using a sputtering technique showed a significant variation in lattice parameter (within the range of values given above) with substrate temperature [Ching et al., 1995]. A search of the listed manganese gallium alloys also showed no definite matches with the unidentified peaks, though the shoulder on the (0002) peak at ~33.1° (figure 7.8, bottom) could be due to the hexagonal Mn_3Ga (1100) phase for which a peak is expected at 31.155°. It may be possible that the ferrimagnetic[56] Mn_3GaN phase, which has been observed previously [Reed et al., 2001] in thermally annealed GaMnN samples, is present in the film, but we were unable to obtain any crystallographic data on this phase.

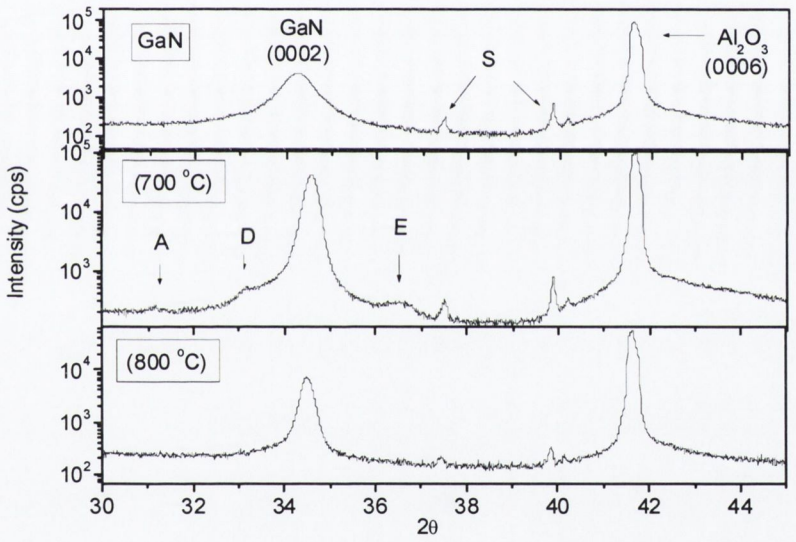

Fig. 7.9 XRD patterns for films grown using the 2% Mn target at a substrate temperature of 700 °C (middle) and 800 °C (bottom). The peaks labelled "s" were identified as originating from either the sample holder or silver paint. The top panel is an XRD spectrum of pure GaN on sapphire.

It should be noted that in these XRD scans, a number of peaks were identified as originating from the substrate; these peaks are labelled "S" in figures 7.8 and 7.9. The peak at ~ 40° is most likely a W impurity line, since the Ni filter was not used for these

[56] A property exhibited by materials whose atoms or ions tend to assume an ordered but nonparallel arrangement in zero applied field below a certain characteristic temperature (Néel temperature).

measurements, whereas the peak at 37.4° seems to be due to the silver paint used to affix the substrates to the heater.

7.5 Magnetic measurements

The magnetic moment per manganese atom in Mn doped GaN was measured using a Superconducting Quantum Interference Device (SQUID) from liquid helium temperatures (4.2 K) up to room temperature[57]. In this device, the field applied by the superconducting coils can be incremented in steps of ~ 10^{-5} T up to 5 T, and the SQUID sensing coils have a sensitivity of ~ 10^{-11} J/T. Before determining the magnetic component of the film, the sapphire substrate was first scanned and its contribution subtracted from subsequent thin film-on-sapphire measurements. The film and substrate plane was perpendicular to the applied magnetic field for all measurements (see figure 7.10).

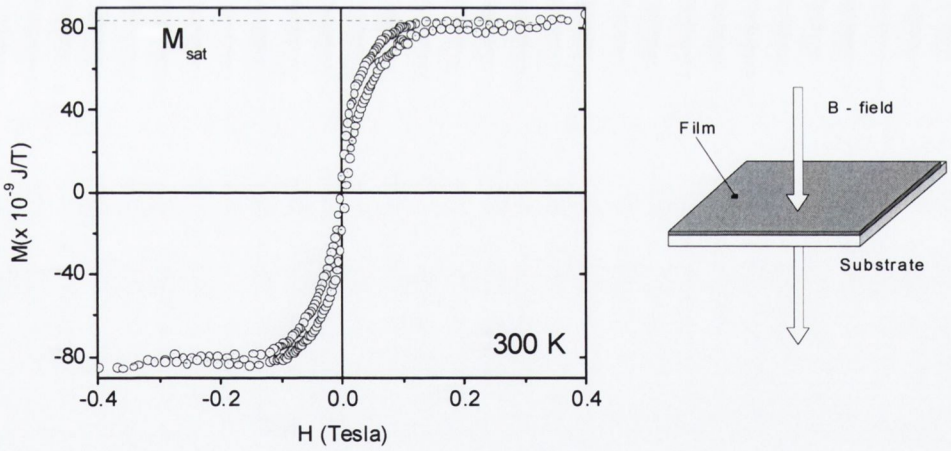

Fig.7.10 Room temperature magnetisation of GaMnN film grown at 800 °C from a 10 % Mn target (Mn concentration in the film = 25%). The magnetic (B) field orientation with respect to the substrate is illustrated in the schematic on the right.

Magnetization measurements were carried out on a number of films but to date only one has shown the hysteresis characteristic of a ferromagnetic material. The Mn concentration

[57] These measurements were carried out by the Magnetism and Spin Electronics group at TCD.

in this film was found to be 25% by EDAX, and the film showed room temperature magnetic hysteresis, with a saturation moment of approximately 80×10^{-9} J/T, as illustrated in figure 7.10. The magnetic moment per Mn atom in the film can be estimated using the saturation magnetisation, if the film mass, m_f, is known. From reflectivity measurements (fig. 7.7), the film thickness was calculated to be 400 nm, and assuming the density of the film is close to that of GaN ($\rho_f \sim 6$ g cm^{-3}), the mass of the film can be simply approximated in terms of the volume of the film thickness, h, and area (A_f) as:

$$m_f = \rho_f \times h \times A_f = 6\times10^{-5} g$$

The molar mass of the film, assuming a stoichiometry of $Mn_{0.2}Ga_{0.8}N$ (from EDAX measurements), can be written in terms of the molar masses of Mn, Ga and N as:

$$M_{GaMnN} = 0.2M_{Mn} + 0.8M_{Ga} + 1M_N = 0.2\times54.9 g/mol + 0.8\times69.7 g/mol + 14 g/mol$$

This yields a value of 80.7 g mol^{-1} for the molar mass of the film, which corresponds to a total number of Mn atoms, N_{Mn}, given by:

$$N_{Mn} = 0.1\times\frac{6\times10^{-5} g}{80.7 g/mol}\times6.022\times10^{23} atoms/mol = 4.5\times10^{16}$$

Here the factor of 0.1 accounts for the Mn fraction with respect to the total number of Mn+Ga+N atoms in the film. Since the total saturation magnetisation is $\sim 80\times10^{-9}$ J/T, the moment per Mn atom is given in terms of the Bohr magneton ($\mu_B = 9.27\times10^{-24}$ J T^{-1}) as:

$$\mu_{Mn} = \frac{80\times10^{-9} J/T}{5.6\times10^{16}} = 1.2\times10^{-24} J/T \cong 0.1\mu_B$$

This is quite a low magnetic moment per atom; in comparison, the magnetisation measured for a GaAs film doped with 7% Mn corresponded to a moment of 2.3 μ_B per Mn atom [Tanaka, 1998]. Alternatively, the moment per Mn atom can be predicted using the expression for the saturation magnetisation (p.421, [Kittel, 1996]):

$$M_{sat} = N_{Mn} g \mu_B J \qquad \text{(eq. 7.2)}$$

Here J is the spin associated with the Mn^{2+} ion which can be taken as 5/2 (section 7.1.2) and the g factor for Mn^{2+} with spin 5/2 has been calculated[58] as1.26 [Craik, 1995] and this expression yields a value of ~ 3 μ_B per Mn atom. The discrepancy between the measured (~ 0.1 μ_B) and expected (2-3 μ_B) magnetization is unclear at this point. A common source of error in these magnetic moment calculations is often the mass measurement, which relies primarily on accurate measurement of the film thickness (assuming the density is reasonably well known). However, the thickness determined from reflectivity data was checked against profilometric measurements of the height of a step created by masking a portion of the film during deposition (section 3.4.2), and both values agreed to within 15% error. On the other hand, the low moment per Mn atom is perhaps not that surprising in light of the XRD measurements (figure 7.8, bottom). Clearly, all of the Mn is not being incorporated into the GaN lattice to give single phase GaMnN. However, even if a large fraction of the Mn is taken up in the most stable high temperature phase, Mn_4N, a higher moment might be expected since Mn_4N is ferromagnetic at room temperature, though it does have a comparatively low moment per Mn atom (1-1.2 μ_B [Takei et al., 1962])[59]. Alternatively, it may be the case that a large fraction of the Mn carriers introduced to the film is not ordering ferrormagnetically. Previous efforts to electrically p-dope InAs with Mn showed that the ratio of active Mn acceptors to doped Mn atoms was at best 50%. Such behaviour is similarly to be expected with GaN considering the history of problems associated with p-doping of GaN [Amano et al., 1989] (recall the introduction to the thesis). For the films grown in this work, the activation fraction appears to be less than 0.1. This reason that hysteresis was not observed in the 5% Mn doped films may simply be due to the fact that the activation fraction and thus the number of ordered spins is comparatively low at this doping concentration. Since the use of higher doping concentrations must be avoided to prevent

[58] The g factor is calculated from the effective Bohr magneton number $p=g[J(J+1)]^{1/2}$, which has been measured as 5.9. See, for example, table 2.1 in [Craik, 1995].

[59] A number of models have been proposed to explain the comparatively low moment per Mn atom in Mn_4N. It is now believed to be due to an anti parallel spin competition between the Mn spins at the face centred and corner sites. See Takei et al. [1962] for a detailed discussion.

phase-separation, the activation fraction must be increased before any realistic progress with DMS film growth using PLD can be achieved.

7.6 Conclusions

Although quantitative analysis of the manganese nitride fraction is required to fully establish the amount of Mn substituted for Ga in the GaN lattice, XRD measurements indicate that single phase GaMnN growth can only be achieved with up to 5% Mn using PLD. It seems that a comparatively high substrate temperature is required to achieve single phase growth ($T_s \geq 800$ °C), similar to observations in MBE growth of GaMnN. For the sintered GaMnN targets, the maximum solubility appears to be less than 2% as previously reported for thermally annealed GaMnN. Since the Mn fraction in the films is greater than that of the targets, there is little need to use targets with an Mn doping concentration greater than 5 at.%. The reason for the high Mn concentrations in the films is most likely due to the greater ability of Mn to form a nitride at the film surface in comparison with Ga, rather than any difference in the latent heat of vaporisation (though, conversely, preferential evaporation of Mn from the target must not be ruled out). While magnetic hysteresis was observed at room temperature in one of the films, it is unclear as to the origin of the ferromagnetic interaction, with the high temperature ferromagnetic Mn_4N, possibly contributing. An electrical transport study is perhaps the best approach to quantifying the activation fraction, though to date we have not been able to carry out Hall measurements on these films as the resistivity was too high.

8. Conclusions and suggestions for future work

This thesis has attempted to identify the requirements for stoichiometric thin film growth of GaN by PLD. However, the conclusions from this study need not be limited to film growth alone, as the ablated target results in chapters four and five may have relevance to laser writing (metallisation) techniques involving metal nitrides (or metal-oxides) or thin film-substrate separation using laser lift-off, which appears to be a promising technique for obtaining stand-alone substrates that cannot otherwise be grown in bulk form. Though the final chapter (magnetic doping of GaN) deviates somewhat from the main objective of the thesis, it is quite relevant to the long term direction which nitride PLD may take. At this point, it is worth summarising the main conclusions from the individual experimental results chapters and considering some aspects which may be worth investigating further.

Chapter 4: PLD of GaN using a GaN target

Decomposition of the GaN target surface due to laser heating seems to lead to the preferential evaporation of the group V element as well as non-stoichiometric material transfer from target to film, which affects the suitability of nanosecond PLD as a GaN film growth technique. Reflectivity analysis revealed that the Ga excess in the films seem to be of the order of 10% when the films are deposited in high vacuum. A compositional analysis technique such as Rutherford back-scattering may be required to establish the Ga excess at the target surface (clearly, the surface appears to have a metal excess). On the point of target properties, an improved sintering procedure, i.e. high pressure (~ 10 bar N_2) and high temperature (~1300 °C), is required to improve target densification and to limit the likelihood of particulate expulsion and exfoliational. This approach will also increase the probability of oxide removal from the target powders. The introduction of a N_2 background gas to a pressure of ~ 0.05-0.1 mbar appears to be sufficient to redress the Ga excess in the films if the ablation rate is sufficient (which seems to be the case at 2.5 J cm^{-2}), though it has not been established where the free Ga is nitrided. As suggested earlier, a spectroscopic study of the plume at different distances from the target (and

perhaps at different background gas pressures, particularly at the shockfront) should prove useful in identifying this region. Otherwise, a reflectivity study at shorter target-substrate distances may prove informative in this regard. The ionisation fraction in the plume was determined to be of the order of 10%, which would indicate that a large fraction of ablated Ga is ionised, assuming the ionic component of the plume is dominated by single Ga anions. One aspect of the plume –gas interaction which has not been considered is that of the electron-gas collisional cross-section. It is likely that the electron component of the plume contributes significantly to background gas activation, and a Langmuir probe study of this interaction (particularly the dependence with fluence) would be most informative.

Chapter 5: PLD of GaN using a Ga target

While gallium metal offers a considerable advantage over the nitride powder as a high purity target material, a number of drawbacks have been identified, all of which are related to the inconsistent nature of the target surface. Although one might expect that the target surface should be liquid for most of the laser pulse duration (considering the ablation model of chapter 2), mass loss results indicate that the reflectivity is well below that previously reported for the melt. A time-resolved reflectivity study of the ablated target surface would confirm whether this is indeed the case. Both the ionisation fraction (at ~ 30 %) and the ion energies for Ga target ablation appear to be higher than the corresponding values for GaN target. Sputtering of the film by high energy ions (> 25 eV) seems to be contributing to the low growth rate measured when using this target, though the reflectivity results are not as convincing as in the GaN target case (the films are also easily scratched, which ruled out confirmation of the thickness using profilometry). An ellipsometry study of these films may prove quite useful in this regard, and may also confirm the optical properties measured using reflectivity. Once again, a spectroscopic study of the plume-gas interaction would be most useful to establish the nitride formation region. Though stoichiometric growth is possible, once a relatively high N_2 pressure (> 0.2 mbar) and correspondingly high fluence (> 3 J cm^{-2}) are used, the crystalline quality of the films is poor in comparison with films grown using the GaN

target in N_2. Therefore, it seems that liquid target PLD of Ga in an N_2 background is not suitable for high quality thin film growth of GaN.

Chapter 5: Plasma-assisted PLD of GaN

The suitability of three nitrogen plasma sources-two of which operated in continuous mode with the other pulsed-for PLD of GaN was studied. The simplicity of the pulsed ring discharge both in its construction and maintenance (i.e. no cooling requirements) makes it the most attractive option at present, despite reservations one might have regarding the inclusion of a high voltage electrode in the deposition environment. Measurements of the discharge current show that the electrode is most suitable for PLD when a positive charging voltage is used (~ 100 V), in a background gas of 0.05-0.1 mbar N_2, since at this polarity, the discharge duration covers the time of arrival of the plume to the substrate. In addition the breakdown time is fixed, whereas for negative charging the time at which the discharge was initiated tended to vary considerably. It was possible to grow oriented films at 0.1 mbar using the pulsed source and a Ga target; this is not possible when using a molecular nitrogen background. Even so, the grain-size of these films is considerably less than those grown using the GaN target, indicating that the metal-target/discharge source combination requires a great deal of further investigation.

On the other hand, the "small-anode" and HCPEE sources offer better control of the various plasma parameters (e.g. flux, temperature). Therefore, it maybe worth considering the possibility of running either of these sources in pulsed mode.

Chapter 7: Magnetic doping of GaN

A Mn doped nitride ceramic target was used to deposit thin films of a novel diluted magnetic semiconductor (GaMnN). The solubility issue seems to have limited progress with III-V spintronics materials for sometime now, and in this work, similar obstacles have been identified. Single phase growth appears to be possible only for Mn concentrations up to 5 at.%. Since EDAX measurements revealed that the Mn fraction in the films is higher than that of the target mix, lower target preparations should be used in future, preferably from concentrations of less than one per cent up to 5 % maximum. A

Vegard's law study (lattice parameter vs Mn concentration) of the films over this range would confirm the solubility limit (the Mn concentrations used for this work were probably too high and well exceeded the limit for most films). The crystalline structure of the films shows strong substrate temperature dependence, with temperatures in excess of 800 °C required for single phase growth. Ferromagnetism was only observed in heavily doped (20 at.% Mn) phase-separated films. The origin of the magnetisation is unclear at this point, though magnetization measurements indicate that the number of ferromagnetically activated Mn atoms is quite low (perhaps less than 10%). This may be due to the purity of the starting powders, as p-doping of GaN has always proved a major difficulty and the likelihood of a significant fraction of oxygen impurities in the nitride powders will not improve this situation. Again, an improved target calcination procedure may counteract this problem, but alternatively switching to a Mn:Ga alloy target is likely to prove the most reliable method of eliminating impurities.

Concluding remarks

Keeping in mind the recent success of MOCVD and MBE techniques for the fabrication of GaN-based multi-layer structures for optoelectronic applications, PLD does not appear to be a commercially competitive film growth process in this technology area. Nevertheless, it is likely that PLD will continue to have a role for the deposition of nitride materials for research, where exploration of a wide range of target compositions and doping combinations is often required. Discharge sources of excited nitrogen have accommodated the use of the high purity metal targets, and it seems likely that this combination will be the preferred choice for the PLD of electronic grade material, if sufficient growth rates and film stoichiometry can be obtained at low laser fluence to avoid splashing (alternatively a target cooling mechanism would relax these fluence constraints somewhat). On the other hand, it is the facility for stoichiometry control of complex film structures and the extended solubility limits for bandgap tuning or magnetic doping that, perhaps, offer the best opportunity for establishing PLD as a niche area in nitride film growth. In this regard, growth of magnetically doped nitrides should be pursued, with particular emphasis placed on combining a nitrogen plasma discharge with film growth using a metal alloy target.

Appendix A. Crystal structure of GaN

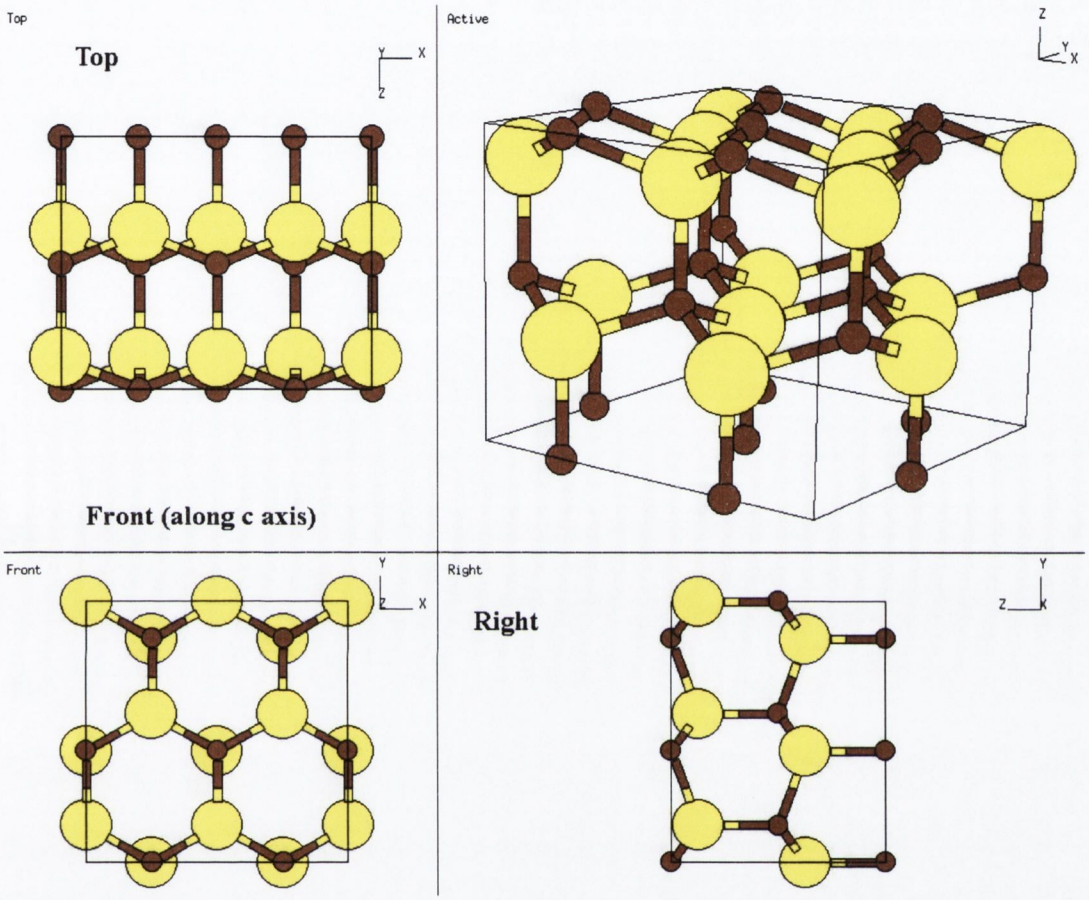

Fig. A1 Wurtzite structure ($P6_3mc$) for hexagonal GaN.

The stacking sequence is: $Ga_AN_AGa_BN_BGa_CN_CGa_AN_AGa_BN_BGa_CN_C$.....

For the ideal hexagonal structure, the ration of the *a* and *c* lattice parameters, *u*, is equal to 3/8, whereas the experimentally measured value for GaN is slightly less.

For a Ga atom at (0, 0, 0) the next nearest Ga atom is at (2a/3, a/3, a/2), while N atoms are at (0, 0, c) and (2a/3, 1a/3, a(½+u)).

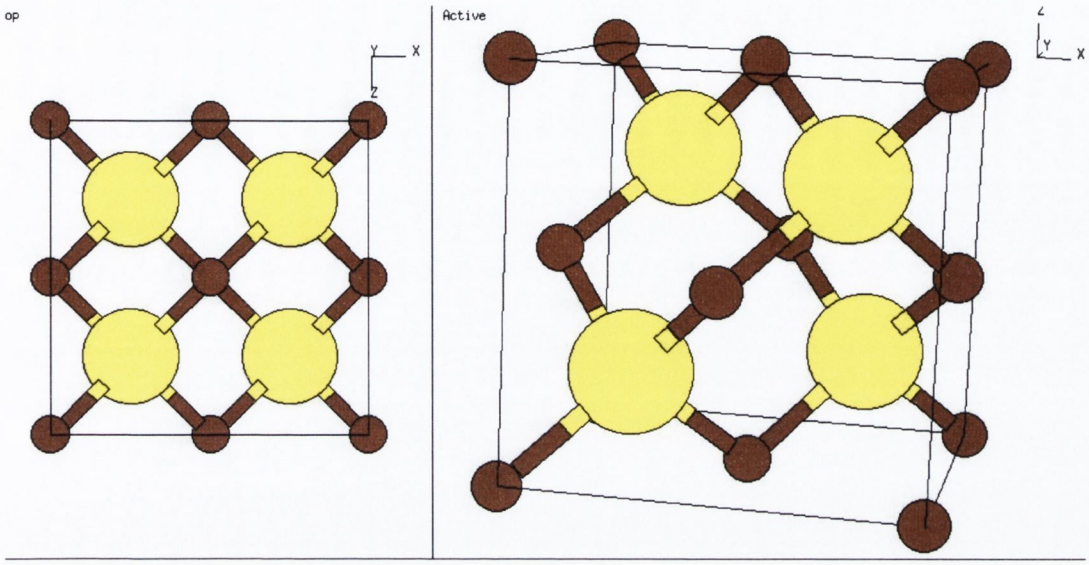

Fig. A2 Zincblende structure for cubic GaN.

The stacking sequence is:

$Ga_AN_AGa_BN_BGa_AN_AGa_BN_BGa_CN_CGa_CN_C$.....

For ideal u (=3/8) the nearest neighbour positions are the same as in the wurtzite structure. However, the next nearest neighbour positions differ.

a_0=4.52 Å.

Crystallographic diagrams taken from Centre for Computational Material Science database, NRL, Washington d.c., U.S.A. (http://cst-www.nrl.navy.mil/lattice/)

Appendix B. Thermodynamic quantities

1. Thermodynamic quantities

Gibb's free energy:

$$G = H - TS = U - \tau\sigma + pdV = N\mu$$

H = Enthalpy	$\tau = k_B T = \dfrac{\partial U}{\partial \sigma}$ = Temperature
S = $k_B\sigma$ = Entropy	N = Particle number
U = Internal energy	$\mu = \dfrac{\partial G}{\partial N}$ = Chemical potential

If there are more than one species, the free energy is written as:

$$G = \sum_i N_i \mu_i \rightarrow \left(\mu_i = \frac{\partial G}{\partial n_i} \right)_{T,p,V}$$

The change in the total Gibbs free energy for a system (which is zero when the reaction reaches its equilibrium state) is defined as:

$$\Delta G = \Sigma G_{products} - \Sigma G_{reactants}$$

If □G is negative, the reaction will proceed spontaneously as the system seeks to attain minimum energy.

2. Kinetics of reaction and vapour pressure

The reaction quotient relates the Gibb's free energy of a system to quantities which describe the concentration of a component at a given time in a reaction. Such quantities include the molar concentration or the partial pressure, but more generally, the activity of a substance is used in the expression.

$$Q = \frac{\prod_i a^{p_i}}{\prod_j a^{r_j}}$$

The superscripts p_i and r_j are the stoichiometric coefficients in the reaction equation. The activity is a dimensionless quantity which accounts for the non-ideal behaviour of substances, particularly for gases at high pressure. When the reaction reaches equilibrium, the quotient is termed the equilibrium rate constant (K_a). For an ideal gas, the activities can be replaced by the partial pressures with reference to the standard state. By convention, pure solids and liquids take a value of 1 if the gas pressures are in bar. This rate constant is exponentially dependent on temperature, having an Arrhenius form: $K_a = e^{-\Delta G^0/RT}$. This is the exponential form of the standard rate equation:

$$\Delta G^0 = -RT \ln K_a$$

Appendix C. Properties of the refractive index

The following overview of the definition of the dielectric constant and the refractive index is dealt with thoroughly in Principles of Optics (M. Born and E. Wolf), Cambridge University Press (7th edition), Cambridge, 1999, and much of the notation and terminology is taken from chapters I and XIV of that text.

The collective macroscopic response of the electric dipoles in a material to an externally applied electromagnetic field is suitably described by the electric susceptibility, χ_e, associated with the dipoles. χ_e is a second-order tensor which can take into account any anisotropy in the dipole response and the resulting electric displacement, D, is related to the electric field strength, E, by:

$$\vec{D} = \hat{\varepsilon}\vec{E}$$

Here, $\hat{\varepsilon}$ is the complex dielectric constant or electrical permittivity of the material, and is related to the electrical susceptibility by the relation:

$$\hat{\varepsilon} = \varepsilon_0(1 + \chi_e)$$

The dielectric response of the material depends on the frequency, ω, which describes the temporal behaviour of the electromagnetic wave. For a monochromatic wave with a temporal component of the form $E(t) \sim E_0 e^{i\omega t}$, Maxwell's equations can be rearranged to obtain the wave equation as follows (MKS units):

$$\nabla \times \nabla \times \vec{E} = \nabla(\nabla . \vec{E}) - \nabla^2 \vec{E} = -\mu \frac{\partial}{\partial t}(\nabla \times \vec{H})$$

$$\nabla \times H = \sigma \vec{E} + \hat{\varepsilon} \frac{\partial \vec{E}}{dt}$$

$$\Rightarrow \nabla^2 \vec{E} - \mu\hat{\varepsilon} \frac{\partial^2 \vec{E}}{\partial t^2} - \mu\sigma_e \frac{\partial \vec{E}}{\partial t} = \nabla^2 \vec{E} + \hat{k}^2 \vec{E} = 0$$

In these equations σ_e and μ are the electrical conductivity and magnetic permeability of the material, respectively, while $c = 1/\sqrt{\mu_0 \varepsilon_0}$ is the speed of light in vacuum. The complex wave number, $\hat{k}$, is related to the complex dielectric constant by:

$$\hat{k}^2 = \frac{\omega^2}{c^2}\hat{n}^2 = \omega^2 \mu \varepsilon_0 + i\omega\mu\sigma = \frac{\omega^2}{c^2}\left(\varepsilon_0 + i\frac{\sigma}{\omega\varepsilon_0}\right) = \frac{\omega^2}{c^2}\hat{\varepsilon}$$

From the above expression, it is clear that, for materials with non-zero conductivity, the dielectric constant is comprised of a real and an imaginary component. The optical properties of a material are more conveniently expressed in terms of the refractive index, which relates the complex wave velocity in the medium, $\hat{v}$, and the speed of light in vacuum:

$$\frac{c^2}{\hat{v}^2} = \hat{n}^2 = (n - i\kappa)^2 = \hat{\varepsilon} = \varepsilon_1 + i\varepsilon_2$$

κ is the attenuation index or "extinction coefficient". Equating the real and imaginary parts of the indices yields:

$$\varepsilon_1 = n^2 - \kappa^2$$

$$\varepsilon_2 = 2n\kappa = \frac{\sigma}{\omega\varepsilon_0}$$

In non-absorbing media, e.g. for visible light incident on a wide bandgap semiconductor, the refractive index, *n*, is simply the square-root of the dielectric constant ε_1. When absorption is significant, the extinction coefficient can be used to determine the optical absorption depth at the surface of a material i.e. the penetration distance at which the energy density falls to *1/e* of its initial value at the surface:

$$d_{opt} = \frac{\lambda}{4\pi\kappa}$$

The optical absorption coefficient is then defined as $1/d_{opt}$.

Note: since the wave number $\hat{k}$ is not used in the main text of the thesis, for convenience, the extinction coefficient is given by the most commonly used Times New Roman script *k*, rather than the Greek symbol κ used above.

Appendix D. Laser pulse profile

The intensity profile of the excimer laser pulse was measured using a BPX65 photodiode (rise-time = 3.5 ns) with the glass hermetical seal removed to allow transmission at 248 nm (see left figure below).

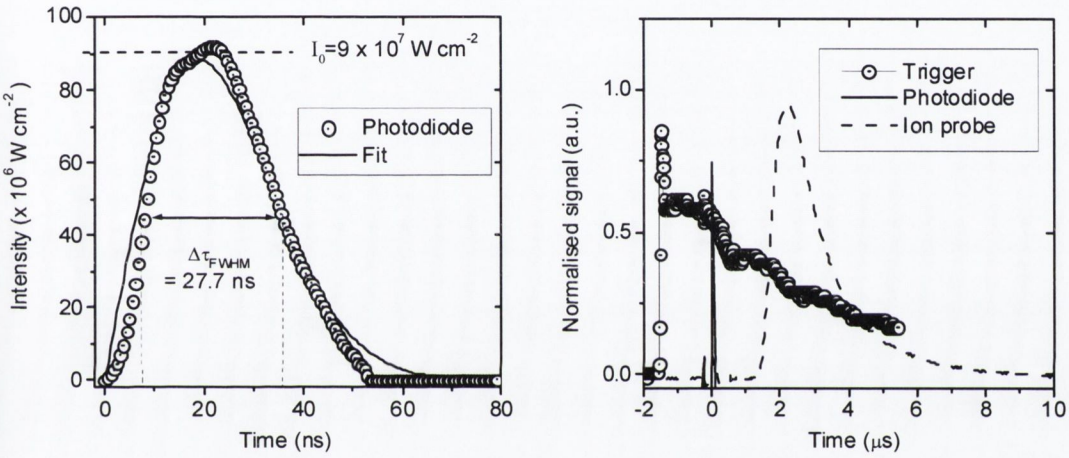

Fig. C1 (a) Laser profile detected by the photodiode (circles) and the fit (solid line) to the profile (left panel). The plots are normalised to an intensity corresponding to average laser fluence per pulse of 2.5 J cm^{-2}. (b) Temporal profiles of the laser pre-trigger (line and circles), the photodiode signal (solid line) and a probe signal taken 4 cm from the target (2.5 J cm^{-2}).

Noting the FWHM of the profile, $\Delta\tau_{FWHM}$, and the average laser fluence per shot, F_0, the intensity profile was fitted (using Microcal Origin) with the expression [Carpene and Schaaf, 2002]:

$$I_l(t) = \frac{F_0}{\Delta\tau_{FWHM}} \frac{t}{b^2} \exp\left[-\left(\frac{t}{w_0}\right)^2\right]$$

The fitting parameters, b and w_0, were found to be 3.35 and 26.5, respectively (the time increment, t, is in ns). A pre-trigger from the laser (V_{peak}=16V), the rising edge (0.1 V_{peak}) of which was detected 1.5 μs before lasing, was used to trigger all probe measurements, as illustrated above (right).

Appendix E : *Mathematica* model for surface temperature and evaporation rate calculation

Properties of the laser pulse

```
f[n_] := F0 * n/(3.35×10^-7) * Exp[-(n/26.5)^2];   (* Analytical expression for temporal profile of laser irradiance *)
F0 = 2.5;                                  (* Average laser energy fluence [J cm^-2] *)
x = 0.5;                                   (* Timestep [ns] *)
Δτ = x×10^-9;                              (* Timestep [s] *)
max = 100;                                 (* Calculation limit in time (timesteps after start of laser pulse) *)
spot = 0.04;                               (* Laser spot area [cm^2] *)
δTpulse = 27.7×10^-9;                      (* FWHM of laser pulse *)
```

Null

Properties of Gallium

(* Properties are in SI - mass, length and volume are in g and cm, cm^3 for convenience *)

```
κ = 0.3;                                   (* Thermal conductivity of target material [W cm^-1 K^-1] *)
ρ = 6;                                     (* Mass density of target [g cm^-3] *)
SpecHeat = 26;                             (* Molar heat capacity [J K^-1 mol^-1] *)
c = SpecHeat/Mmolar;                       (* Specific (mass) heat capacity [J K^-1 g^-1] *)
Mmolar = 139.8;                            (* Molar mass of evaporating species [a.m.u.] *)

kB = 1.38×10^-23;                          (* Boltzmann constant [J K^-1] *)
HeatVap = 264;                             (* Heat of vaporisation [kJ mol^-1] *)
Lv = HeatVap×10^3/NAv;                     (* Latent heat of vapourisation per particle [eV] *)
T0 = 300;                                  (* Initial target surface temperature [K] *)
Tboil = 2500;                              (* Boiling temperature at standard pressure (10^5 Pa) [K] *)
k = 2.73;                                  (* Extinction coefficient at 248 nm *)
λ = 248×10^-9;                             (* Laser wavelength *)
ref = 0.9;                                 (* Surface reflectivity of target to laser radiation *)
NAv = 6.022×10^23;                         (* Avogadro's constant *)
am = 1.67×10^-27;                          (* Atomic mass unit [kg] *)
σ = 10^-17;                                (* Absorption cross-section in plume for 248 nm radiation *)
Null
```

```
(* Routine for calculating Surface temperature,
 Vapour pressure and evaporation rate *)
```

$$\text{For}\left[t = 2x,\ t < \max,\ t \mathrel{+}= x,\ \text{Tsurf} = \text{Sum}\left[\left(\left(A * \text{Irradiance}\left[\left[\frac{n}{x}\right]\right]\right) * r * \text{Exp}\left[-\frac{\sigma \times \text{TotalVapour}\left[\left[\frac{n-x}{x}\right]\right]}{0.707}\right]\right),\ \{n,\ 2x,\ t,\ x\}\right];\right.$$

$$\text{TempList} = \text{Append}[\text{TempList},\ \text{Tsurf}];\ \text{TotalVapour} = \text{Append}\left[\text{TotalVapour},\ \left(\text{TotalVapour}\left[\left[\frac{t-x}{x}\right]\right] + \text{InstFlux}\right)\right]\Big];$$

$$\text{Massloss} = \text{TotalVapour} \times \frac{M_{molar}}{N_{Av}} \times \text{spot};$$

TotMass = Last[Massloss]; (= Total mass Ga evaporated per laser shot [grams]);

$$\text{AblDepth} = \frac{\text{TotMass}}{\rho * \text{spot}} \times 10^7;\ (* \text{ Ablation depth per pulse in nm } *)$$

(Note: time scale in units of timestep (x=0.5 ns) e.g. 200 on scale = 100 ns);

Appendix F. Paschen curve for N_2 [Dakin et al., *Electra,* (32), 61-82, (1974)]

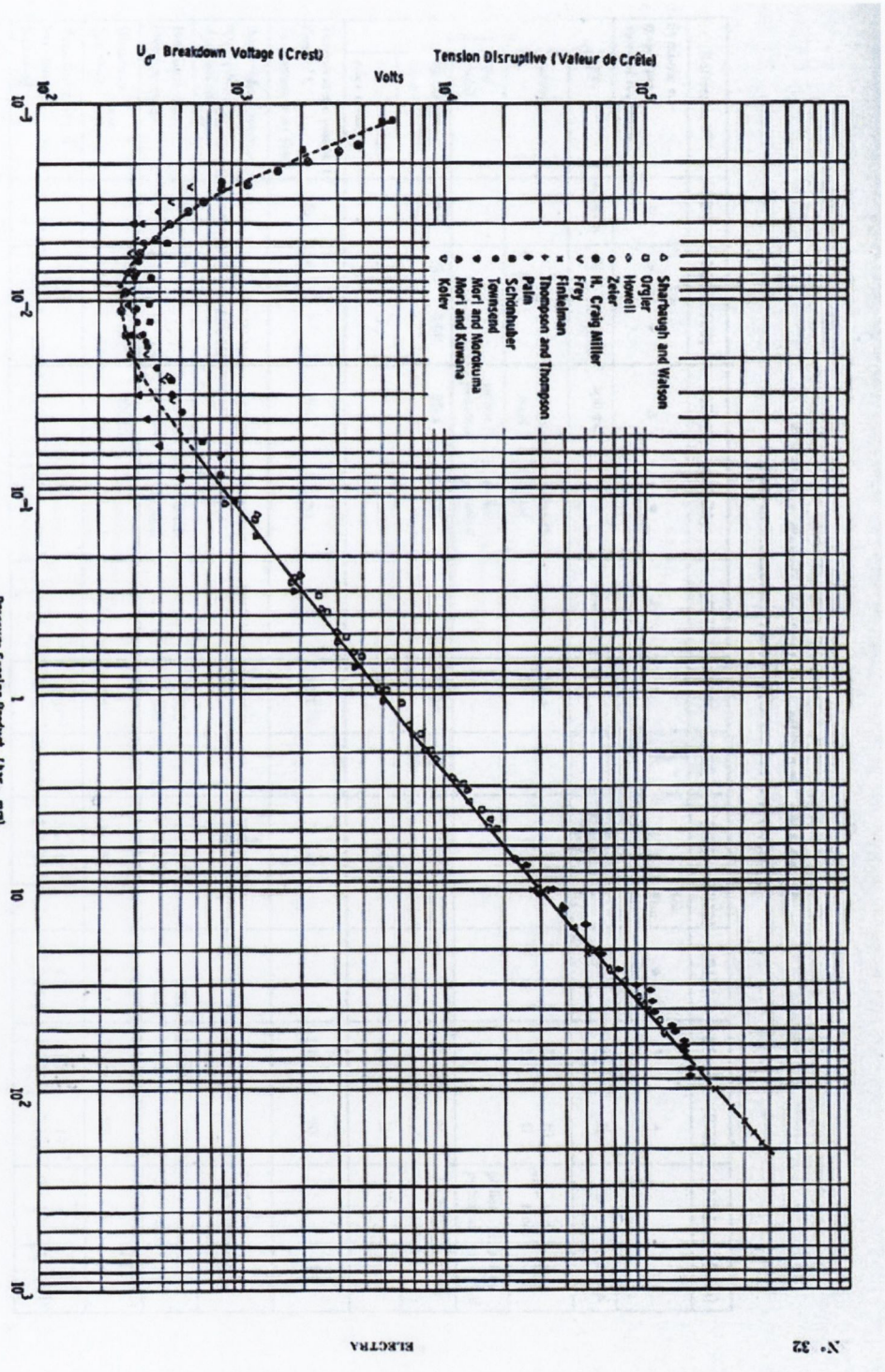

Figure 151

Courbe de Paschen pour l'azote en échelles logarithmiques. Température 25 °C.

Paschen Curve for Nitrogen in log-log scale. Temperature 25 °C.

Appendix G. Definitions and associated errors

G 1 Definitions and nomenclature

Quantity	Symbol	units	Error
Distance to target	d	cm	0.2 cm
Laser spot dimensions	x, y	mm	0.1 mm
Temperature	T	°C	± 20 °C (substrate)
Laser powermeter voltage	V_{Joule}	mV	5 mV
Energy per laser pulse	E	mJ	$E \times(\Delta V_{Joule} / V_{Joule})$
Area (probe or laser spot)	A	mm^2	0.2 mm
Fluence	F	J cm^{-2}	Section G2
Background gas pressure	p	mbar	$0.25p$
Gas density	n_g	cm^{-3}	$0.25n_g$
Particle number	N	-	Section G2
Time of flight	t_{TOF}	µs	0.05 µs
Time-of-flight velocity	v_{TOF}	m s^{-1}	Section G2
Incident angle	θ_i	degree	3 degree (fig G3.1)
Real refractive index	n	-	Section G3.2
Imaginary refractive index	k	-	Section G3.2
Electron charge	e	C	-
Electrical resistance	R	Ω	$0.1R$
Ion / deposition flux	j_{ion} / j_{dep}	cm^{-2} s^{-1}	Section G2
Time-integrated flux	J	cm^{-2}	Section G2
Film growth rate	δ_{Film}	nm/shot	$0.15\ \delta_{Film}$
Absorption depth	d_{opt}	nm	-

G 2 Error analysis of frequently used quantities

Quantity	Definition	Explicit error	Approx. error
Fluence	$F = \frac{E}{A}$	$F \times \left(\frac{\Delta E}{E} + \frac{\Delta A}{A} = \frac{\Delta V_{joule}}{V_{joule}} + \frac{\Delta x}{x} + \frac{\Delta y}{y} \right)$	$0.3F$
Time-of-flight	$v_{TOF} = \frac{d}{t_{\mathrm{TOF}}}$	$v_{TOF} \times \left(\frac{\Delta d}{d} + \frac{\Delta t_{TOF}}{t_{TOF}} \right)$	$0.1 v_{TOF}$
Ion energy	$E_{ion} = \frac{1}{2} m_{ion} v_{TOF}^2$	$E_{ion} \times \frac{2\Delta v_{TOF}}{v_{TOF}}$	$0.2E_{ion}$
Integrated ion flux	$J_{ion} = \frac{1}{RA_n e} \int^{t} V(t)dt$	$J_{ion} \times \left(\frac{\Delta R}{R} + \frac{\Delta A_n}{A_n} \right)$	$0.2J_{ion}$
Total ion number	$N_{total} = \frac{N_0 d^2 2\pi}{\kappa_A \kappa_B}$	$N_{total} \times \left(\frac{\Delta N_0}{N_0} + \frac{2\Delta d}{d} + \frac{\Delta \kappa_A}{\kappa_A} + \frac{\Delta \kappa_B}{\kappa_B} \right)$	$0.4N_{total}$
Deposition flux	$j_{dep} \cong \frac{\delta_{film} \rho_{Film} N_{Av}}{M_{Film}}$	$j_{dep} \times \left(\frac{\Delta \delta_{Film}}{\delta_{Film}} + \frac{\Delta \rho_{Film}}{\rho_{Film}} + \frac{\Delta M_{Film}}{M_{Film}} \right)$	$0.3j_{dep}$

G 3 Error analysis for reflectivity

G 3.1 Bulk reflectivity (Fresnel equations)

The uncertainty in bulk reflectivity calculations associated with uncertainty in the incident angle (θ_i) can be determined by differentiating equation 2.14 with respect to $\theta_i \left(i.e.\_ \Delta R_s = 2 \frac{\partial r_s}{\partial \theta_i} \Delta \theta_i \right)$. The uncertainty in s-polarised reflectivity associated with a 3 degree uncertainty in the incident angle is plotted below (evaluated using Mathematica).

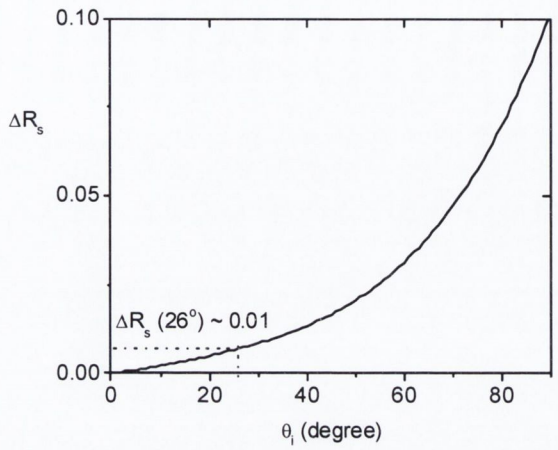

Fig. G1 Variation with incident angle, θi, of the uncertainty in the s-polarised reflectivity of a bulk material for an uncertainty of ± 3 degrees. The uncertainty in reflectivity at an incident angle of 26 degree corresponding to an uncertainty of 3 degrees is ~ 0.01.

G.3.2 Single layer errors

The fit do the data in chapters 4 and 5 was obtained using *Mathematica*, but the software does not give an associated error in the n and k parameters for the fit. In order to gain some idea of the fit accuracy, the maximum error in n and k associated with the maximum deviation of the fits from the measured data was determined. Figure G2 shows the effect of a variation in n (=2.3) on the s-polarised reflectivity of a thin film with increasing thickness (for Δn = 0.05, 0.1). The maximum observed difference in reflectivity for the data plotted in chapter 5 (growth with Ga target) over 500 nm is $\leq$ 0.02 which corresponds to an uncertainty of about $\Delta n = \leq 0.1$, whereas the variation of R_s in the data of chapter 4 is less than 0.01, which corresponds to $\Delta n \leq 0.05$.

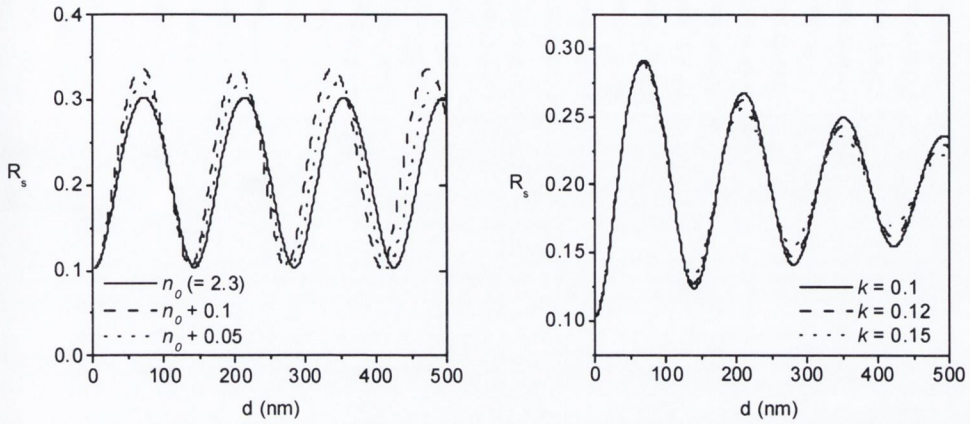

Fig. G2 s-polarised reflectivity for GaN (n =2.3+Δn, Δn = 0, 0.05, 0.1) on sapphire (left). At Δn = 0.1, the variation in R_s is at most ~ 0.01. Also included (right) are the reflectivity traces for various k values.

When absorption, and thus the extinction coefficient (k) is significant, calculation of the associated error in the extracted k value is somewhat complicated by the interdependence of the two optical constants. However, a similar comparison of the experimental and fitted reflectivity data of chapters 4 and 5 with the plot for various k values above (right) suggests that the uncertainty is at most 0.05.

Finally, the error in the gallium fraction (f_{Ga}) can be estimated using the uncertainties calculated above and the data in figure 2.7 (chapter 2). For example, an uncertainty in the refractive index of Δn = 0.1 corresponds to an uncertainty in f_{Ga} of about 0.01, while an uncertainty in k of Δk = 0.05 corresponds to a variation of 0.005 in f_{Ga} when k is near 0.1 (while the n-f_{Ga} dependence is almost linear, the k-f_{Ga} dependence is not, and thus needs to be accounted for depending on the value of f_{Ga}).

Appendix H: Publications

Pulsed laser deposition of wide-bandgap semiconductor thin films,
O'Mahony, Donagh; de Posada, Eduardo; Lunney, James G.; Mosnier, Jean-Paul; McGlynn, Enda
Opto-Ireland 2002: Optics and Photonics Technologies and Applications, Proceedings of SPIE, **4876** (2003), p.4876

Pulsed laser deposition of manganese doped GaN,
O'Mahony, D.; Lunney, J.G.; Tobin, G.; McGlynn, E., Solid-State Electronics, **47**, (2003), p.533

Defect luminescence of GaN grown by pulsed laser deposition
Mah KW, McGlynn E, Castro J, Lunney JG, Mosnier J-P, O'Mahony D, Henry MO.
Journal of Crystal Growth, **222** (2001), p.497

Study of photoluminescence at 3.310 and 3.368 eV in GaN/sapphire(0001) and GaN/GaAs(001) grown by liquid-target pulsed-laser deposition,
Mah KW, Mosnier J-P, McGlynn E, Henry MO, O'Mahony D, Lunney JG, Applied Physics Letters, 80 (2002), pp.3301-3303.

Defect luminescence of GaN grown by pulsed laser deposition,
Mah KW, McGlynn E, Castro J, Lunney JG, Mosnier J-P, O'Mahony D, Henry MO.,
Journal of Crystal Growth, 222 (2001), pp.497-502.

Reference list

Amano, H., M. Kito, K. Hiramatsu and I. Akasaki (1989), *Jpn. J. Appl. Phys. Part 2,,* 28 (12), 2112-2114

Ambacher, O., W. Rieger, P. Ansmann, H. Angerer, T. D. Moustakas and M. Stutzmann (1996), *Solid State Commun.,* 97 (5), 365-370

Anders, A. and S. Anders (1995), *Plasma Sources Sci. Technol.,* 4 (4), 571-575

Anders, A., N. Newman, M. Rubin, M. Dickinson, E. Jones, P. Phatak and A. Gassmann (1996), *Rev. Sci. Inst.,* 67 (3 pt 2), 905

Anisimov, S. I., D. Bauerle and B. S. Luk'yanchuk (1993), *Phys. Rev. B,* 48 (16), 12076-12081

Aspnes, D. E. (1982), *Thin Solid Films,* 89, 249-262

Averyanova, M. V., I. N. Przhevalskii, S. Y. Karpov, Y. N. Makarov, M. S. Ramm and R. A. Talalaev (1997), *Mater. Sci. Eng. B,* B43 (1-3), 167-171

Ball, P. (2000), *Nature,* 404, 918 - 920

Basillais, A., C. Boulmer-Leborgne, J. Mathias and J. Perriere (2002), *App. Surf. Sci.,* 186 (1-4), 416-422

Battino, R. in *Nitrogen and air,* Battino, R., ed. Pergamon Press, Oxford, 1982,

Bhadeshia, H. K. D. H. (2003), *Proc. International Conference on Aluminium (INCAL'03)*, Bangalore, India

Born, M. and E. Wolf, *Principles of Optics,* Cambridge University Press, Cambridge, 1999.

Bruggemann, D. A. G. (1935), *Ann. Phys. Chem.,* 24, 636

Carpene, E. and P. Schaaf (2002), *Phys. Rev. B,* 65 (22), 224111-224111

Carslaw, H. S. and J. C. Jaeger in *Heat Conduction in Solids,* Clarendon Press, Oxford, 2nd Edition, 1986, p. 30.

Cazzanelli, M., D. Cole, J. F. Donegan, J. G. Lunney, P. G. Middleton, K. P. O'Donnell, C. Vinegoni and L. Pavesi (1998), *Appl. Phys. Lett.,* 73 (23), 3390-3392

Chapman, B. in *Glow Discharge Processes: Sputtering and Plasma Etching,* John Wiley & Sons, New York, 1976, p. 93.

References

Chapman, B. in *Glow Discharge Processes,* John Wiley & Sons, New York, 1980a, p. 95.

Chapman, B. in *Glow Discharge Processes,* John Wiley and Sons, New York, 1980b, p. 22.

Chapman, B. in *Glow Discharge Processes,* John Wiley & Sons, New York, 1980c, pp. 21-16.

Chin, V. W. L., T. L. Tansley and T. Osotchan (1994), *J. App. Phys.,* 75 (11), 7365

Ching, K.-M., W.-D. Chang and T.-S. Chin (1995), *J. Alloys Compd.,* 222, 184-187

Chrisey, D. B. and G. K. Hubler, eds., *Pulsed Laser Deposition of Thin Films,* Wiley, New York,1994.

Chu, C.-F., C. K. Lee, C. C. Yu, Y. K. Wang, J. Y. Tasi, C. R. Yang and S. C. Wang (2001), *Mater. Sci. Eng. B,* B82 (1-3), 42-44

Cole, D. (1998), *Ph.D thesis,* Physics Department, Trinity College Dublin, Ireland, Dublin.

Cole, D. and J. G. Lunney (1997), *Mater. Sci. Eng. B.,* 50 (1-3), 20-24

Craik, D. in *Magnetism; Principles and Applications,* John Wiley and Sons, Chichester, 1995, p. 57.

Cullity, B. D. and S. R. Stock, *Elements of X-ray Diffraction,* Prentice Hall, Upper Saddle River (NJ, USA), 2001.

Culprin, M. F. (1957), *Proc. phys. soc.,* 70, 1079

Dakin, T. W., G. Luxa, G. Oppermann, J. Vigreux, G. Wind and H. Winkelnkemper (1974), *Electra,*(32), 61-82

Deiss, J. L., C. Hirlimann, J. L. Loison, M. Robino and G. Versini (2001), *Mater. Sci. Eng. B.,* B82 (1-3), 68-70

DeMaria in *Chemical and Mechanical Behaviour of Inorganic Materials,* Searcy, A. W., D. V. Ragone and U. Colombo, eds., Wiley, New York, 1970, pp. 85-89.

di Palma, T. M., S. Orlando, A. Giardini-Guidoni, A. J. Paul, J. W. Hastie and A. Mele (1995), 86, 68-73

Dietl, T., H. Ohno, F. Matsukura, J. Cibert and D. Ferrand (2000), *Science,* 287 (5455), 1019-1022

Dingle, R., D. D. Sell, S. E. Stokowski, P. J. Dean and R. B. Zetterstrom (1971), *Phys. Rev. B,* 3 (2), 497-500

References

Dodd, P. M., J. G. Lunney and J. V. Armstrong (1994), *Opt. Eng.,* 33 (12), 3969-3973

Dyer, P. E., S. R. Farrar, A. Issa and P. H. Key in *Laser Ablation of Electronic Materials,* Fogarassy, E. and S. Lazare, eds., North-Holland, Amsterdam, 1992, p. 104.

Edgar, J. H., ed., *Properties of Group III Nitrides,* INSPEC, London,1994.

Ehlert, T. C. (1969), *J. Inorg. Nucl. Chem.,* 31 (9), 2705-2710

Ejder, E. (1971), *Phys. Status Solidi A,* 6 (2), 445-448

Feiler, D., R. S. Williams, A. A. Talin, H. Yoon and M. S. Goorsky (1997), *J. Cryst. Growth,* 171 (1-2), 12-20

Fernandez, F. E., E. Rodrigez, M. Pumarol, T. Guzman, W. Jia and A. Martinez (2000), *Thin Solid Films,* 377-378, 781-787

Fucke, W. and U. Seydel (1980), *High Temp. - High Press.,* 12 (4), 419-432

Fukumura, T., Z. Jin, A. Ohtomo, H. Koinuma and M. Kawasaki (1999), *Appl. Phys. Lett.,* 75 (21), 3366-3368

Garcia, J., J. Bartolome, D. Ganzalez, R. Navarro and D. Fruchart (1983a), *J. Chem. Thermodyn.,* 15 (11), 1041-1057

Garcia, J., J. Bartolome, D. Gonzalez, R. Navarro and D. Fruchart (1983b), *J. Chem. Thermodyn.,* 15 (5), 465-473

Geiger, F., C. A. Busse and R. I. Loehrke (1987), *Int. J. Thermophys.,* 8 (4), 425-436

Geohegan, D. B. in *Pulsed Laser Deposition of Thin Films,* Chrisey, D. B. and G. K. Hubler, eds., Wiley, New York, 1994, p. 131.

German, R. M. in *Sintering Theory and Practice,* John Wiley & Sons, New York, 1996, p. 1.

Greene, S. M., A. Piqué, K. S. Harshavardhan and J. Bernstein in *Pulsed Laser Deposition of Thin Films,* Chrisey, D. B. and G. K. Hubler, eds., Wiley, New York, 1994, pp. 23-32.

Groh, R., G. Gerey, L. Bartha and J. I. Pankove (1974), *Phys. Status Solidi A,* 26 (1), 353-357

Grzegory, I., J. Jun, S. Krukowski, M. Bockowski and S. Porowski (1993), *Physica B,* 185 (1-4), 99-102

Gunster, J., R. Gorke, J. G. Heinrich and R. Souda (2001), *Appl. Surf. Sci.,* 173 (1-2), 76-83

References

Gyorgy, E., C. Ristoscu, I. N. Mihailescu, A. Klini, N. Vainos, C. Fotakis, C. Ghica, G. Schmerber and J. Faerber (2001), 90 (1), 456-461

Haglund, R. F. in *Laser Ablation and Desorption,* Miller, J. C. and R. F. Haglund, eds., Academic Press, San Diego, 1998a, p. 86.

Haglund, R. F. (1998b), in [Miller, J. C. and R. F. Haglund, 1998b], p. 81

Haglund, R. F. and J. C. Miller, *Laser Ablation and Desorption,* Academic Press, San Diego, 1998.

Hampshire, S. in *Sintering of Nitrogen Ceramics,* The Parthenon Press, Carnforth (UK), 1986, pp. 47-52.

Hansen, T. N., J. Schou and J. G. Lunney (1999), *Appl. Phys. A,* A69, 601-604

Harrison, W. A. in *Electronic Structure and the Properties of Solids,* Dover, New York, 2nd, 1989, p. 176.

Heavens, O. S. in *Optical Properties of Thin Solid Films,* Dover, New York, 1965, pp. 46-95.

Hensler, D. H. (1972), *Appl. Opt.,* 11 (11), 2522-2528

Hirayama, Y., H. Yabe and M. Obara (2001), *J. App. Phys.,* 89 (5), 2943-2949

Hori, H., S. Sonoda, T. Sasaki, Y. Yamamoto, S. Shimizu, K. Suga and K. Kindo (2002), *Physica B,* 324 (1-4), 142-150

Horwitz, J. S. and J. A. Sprague in *Pulsed Laser Deposition of Thin Films,* Chrisey, D. B. and J. R. Huber, eds., Wiley, New York, 1994, pp. 229-254.

Huang, T. F., A. Marshall, S. Spruytte and J. S. Harris, Jr. (1999), *J. Cryst. Growth,* 200 (3-4), 362-367

ICCD www.ICCD.com

ICDD www.ICDD.com (International Centre for Diffraction Data)

Ichige, K., Y. Matsumoto and A. Namiki (1988), *Nucl. Instrum. Methods Phys. Res. B.,* B33 (1-4), 820-823

Iida, T. and R. I. L. Gutherie, *The Physical Properties of Liquid Metals,* Clarendon Press, Oxford, 1988a.

Iida, T. and R. I. L. Gutherie in *The Physical Properties of Liquid Metals,* Clarendon Press, Oxford, 1988b, p. 134.

References

Jain, S. C., M. Willander, J. Narayan and R. Van Overstraeten (2000), *J. Appl. Phys.,* 87 (3), 965-1006

Jiemin, Z. and M. Lamvik (1998), *High Temp. - High Press.,* 30 (3), 307-314

Jordan, R. (1998), *Ph.D thesis,* Physics Department, Trinity College, Dublin.

Kantor, Z., Z. Geretovszky and T. Szorenyi (2000), *Appl. Surf. Sci.,* 154-155, 78-82

Karpinski, J. and S. Porowski (1984), *J. Cryst. Growth,* 66 (1), 11-20

Kelly, F., D. R. Gilbert, R. Chodelka, R. K. Singh and S. Pearton (2003), *Solid-State Electron.,* 47 (6), 1027-1030

Kelly, M. K., A. O. Ambacher, B. Dahlheimer, G. Groos, R. Dimitrov, H. Angerer and M. Stutzmann (1996), *Appl. Phys. Lett.,* 69 (12), 1749-1751

Kelly, R. and R. W. Dreyfus (1988), *Nucl. Instrum. Methods Phys. Res. B,* B32 (1-4), 341-348

Kelly, R. and A. Miotello in *Pulsed Laser Deposition of Thin Films,* Chrisey, D. B. and J. R. Huber, eds., Wiley, New York, 1994, pp. 70-71.

Kelly, R., A. Miotello, A. Mele and A. Giardini Guidoni in *Laser Ablation and Desorption,* Haglund, R. F. and J. C. Miller, eds., Academic Press, 1998, pp. 225-245.

Kittel, C., *Introduction to Solid State Physics,* John Wiley & Sons, New York, 1996.

Kofman, R., P. Cheyssac and J. Richard (1977), *Phys. Rev. B.,* 16 (12), 5216-5224

Koopman, D. W. (1971), *Phys. Fluids,* 14 (18), 1707-1716

Koopman, D. W. (1972), *Phys. Fluids,* 15 (11), 1959-1969

Krukowski, S., A. Witek, J. Adamczyk, J. Jun, M. Bockowski, I. Grzegory, B. Lucznik, G. Nowak, M. Wroblewski, A. Presz, S. Gierlotka, S. Stelmach, B. Palosz, S. Porowski and P. Zinn (1998), *J. Phys. Chem. Solids,* 59 (3), 289-295

Lide, D. R., ed., *Handbook of Chemistry and Physics,* CRC Press, Florida,1998.

Litvinov, V. I. and N. K. Dugaev (2001), *Phys. Rev. Lett.,* 86 (24), 5593-5596

Lorenz, M. R. and B. B. Binkowski (1962), *J. Electrochem. Soc.,* 109, 24-26

Lunney, J. G. and R. Jordan (1998), *Appl. Surf. Sci.,* 127-129, 941-946

Mah, A. D. (1958), *J. Amer. Chem. Soc.,* 80, 2954

References

Mah, K. W. (2002), *Ph.D thesis,* School of Physical Sciences, Dublin City University, Dublin.*PL of GaN grown using a liquid target*

Mah, K. W., E. McGlynn, J. Castro, J. G. Lunney, J.-P. Mosnier, D. O'Mahony and M. O. Henry (2001), *J. Cryst. Growth,* 222 (3), 497-502

Mah, K. W., J.-P. Mosnier, E. McGlynn, M. O. Henry, D. O'Mahony and J. G. Lunney (2002), *Appl. Phys. Lett.,* 80 (18), 3301-3303

Manzello, S. and J. Yang (2003), *Physics of Fluids,* 15 (1), 257-260

Massalski, T. B. in *Binary Alloy Phase Diagrams,* ASM International, Vol.2, 2, 1990,

McKiernan, A. P. and J.-P. Mosnier (2002), *Appl. Surf. Sci.,* 197-198, 325-330

Merel, P., M. Chaker, M. Tabbal and H. Pepin (2001), *Appl. Surf. Sci.,* 177 (3), 165-171

Miljevic, V. (1984), *Rev. Sci. Instrum.,* 55 (6), 931-933

Mott-Smith, H. M. and I. Langmuir (1926), *Phys. Rev.,* 28, 727-763

Munekata, H., H. Ohno, S. von Molnar, A. Segmuller, L. L. Chang and L. Esaki (1989), *Phys. Rev. Lett.,* 63 (17), 1849-1852

Munir, Z. and A. Searcy (1965), *J. Chem. Phys.,* 42, 4223-4228

Muth, J. F., A. J. H. Lee, I. K. Shmagin, R. M. Kolbas, H. C. Casey, Jr., B. P. Keller, U. K. Mishra and S. P. DenBaars (1997), *Appl. Phys. Lett.,* 71 (18), 2572-2574

Nakamura, S. and G. Fasol, *The Blue Laser Diode,* Springer Verlag, Berlin, 1997.

Newman, N. (1997), *J. Cryst. Growth,* 178 (1-2), 102-112

Newman, N. in *Gallium Nitride (GaN) I,* Pankove, J. I. and T. D. Moustakas, eds., Academic Press, San Diego, Vol.50, 1998a, p. 85.

Newman, N. (1998b), in [Pankove and Moustakas, 1998b], pp. 55-98

Nikishin, S. A., G. A. Seryogin, H. Temkin, V. G. Antipov, S. S. Ruvimov and A. V. Merkulov (1997), *J. Cryst. Growth,* 175-176 (pt.1), 139-144

Nonomura, S., S. Kobayashi, T. Gotoh, S. Hirata, T. Ohmori, T. Itoh, S. Nitta and K. Morigaki (1996), *J. Non-Cryst. Solids,* 198-200 (pt.1), 174-177

Ogale, S. B., R. J. Choudhary, J. P. Buban, S. E. Lofland, S. R. Shinde, S. N. Kale, V. N. Kulkarni, J. Higgins, C. Lanci, J. R. Simpson, N. D. Browning, S. Das Sarma, H. D. Drew, R. L. Greene and T. Venkatesan (2003), *Phys. Rev. Lett.,* 91 (7), 077205-077201

Ohno, H. (1998), *Science,* 281, 951-956

References

Overberg, M. E., C. R. Abernathy, S. J. Pearton, N. A. Theodoropoulou, K. T. McCarthy and A. F. Hebard (2001), *Appl. Phys. Lett.,* 79 (9), 1312-1314

Pearton, S. J., C. R. Abernathy, M. E. Overberg, G. T. Thaler, A. H. Onstine, B. P. Gila, F. Ren, B. Luo and J. Kim (2002), *Materials Today,* June, 24-31

Penning, F. M. in *Electrical Discharges in Gases,* Cleaver-Hume Press Ltd, London, 1957, p. 31.

Phillips, J. C. (1970), *Rev. Mod. Phys.,* 42 (3), 317-354

Polyakov, A. Y., N. B. Smirnov, A. V. Govorkov, J. Kim, F. Ren, G. T. Thaler, M. E. Overberg, R. Frazier, C. R. Abernathy, S. J. Pearton, C.-M. Lee, J.-I. Chyi, R. G. Wilson and J. M. Zavada (2003), *Solid-State Electron.,* 47 (6), 981-987

Porowski, S. and I. Grzegory (1997), *J. Cryst. Growth,* 178 (1-2), 174-188

Powell, R. C., N.-E. Lee, Y.-W. Kim and J. E. Greene (1993), *J. Appl. Phys.,* 73 (1), 189-204

Pronko, P. P., P. A. VanRompay, Z. Zhang and J. A. Nees (1999), *Phys. Rev. Lett.,* 83 (13), 2596-2599

Ready, J. F., *Effects of High Power Laser Radiation,* Academic Press, London, 1971.

Reed, M. L., N. A. El-Masry, H. H. Stadelmaier, M. K. Ritums, M. J. Reed, C. A. Parker, J. C. Roberts and S. M. Bedair (2001), *Appl. Phys. Lett.,* 79 (21), 3473-3475

Regan, M. J., H. Tostmann, P. S. Pershan, O. M. Magnussen, E. DiMasi, B. M. Ocko and M. Deutsch (1997), *Phys. Rev. B,* 55 (16), 10786-10790

Ristoscu, C., I. N. Mihailescu, M. Velegrakis, M. Massaouti, A. Klini and C. Fotakis (2003), *J. Appl. Phys.,* 93 (4), 2244-2250

Rossow, U. in *Epioptics,* McGilp, J., D. Weaire and C. Patterson, eds., Springer, Berlin, 1995, p. 51.

Santagata, A., V. Marotta, S. Orlando, R. Teghil, M. Zaccagnino and A. Giardini (2003), *Appl. Surf. Sci.,* 208-209, 101-106

Schoonmaker, R. C., A. Buhl and J. Lemley (1965), *J. Phys. Chem.,* 69 (10), 3455-3460

Schulz, L. G. (1955), *J. Opt. Soc. America,* 47 (1), 64-69

Searcy, A. in *Chemical and Mechanical Behaviour of materials,* Searcy, A., D. V. Ragone and U. Colombo, eds., Wiley-Interscience, New York, 1970, pp. 33-55.

Singh, R. K. and J. Narayan (1990), *Phys. Rev. B,* 41 (13, pt.A), 8843-8859

References

Slack, G. A. (1973), *J. Phys. Chem. Solids,* 34 (2), 321-335

Slack, G. A. and T. F. McNelly (1976), *J. Cryst. Growth,* 34 (2), 263-279

Soo, Y. L., G. Kioseoglou, S. Kim, S. Huang, Y. H. Kao, S. Kuwabara, S. Owa, T. Kondo and H. Munekata (2001), *Appl. Phys. Lett.,* 79 (24), 3926-3928

Strite, S. and H. Morkoc (1992), *J. Vac. Sci. Technol. B.,* 10 (4), 1237-1266

Suzuki, K., T. Kaneko, H. Yoshida, Y. Obi, H. Fujimori and H. Morita (2000), *J. Alloys Compd.,* 306 (1-2), 66-71

Szyszko, T., G. Kamler, B. Strojek, G. Weisbrod, S. Podsiadlo, L. Adamowicz, W. Gebicki, J. Szczytko, A. Twardowski and K. Sikorski (2001), *J. Cryst. Growth,* 233 (4), 631-638

Tabuchi, M., M. Takahashi and F. Kanamaru (1994), *J. Alloys Compd.,* 210 (1-2), 143-148

Takei, W. J., R. R. Heikes and G. Shirane (1962), *Phys. Rev.,* 125 (6), 1893-1897

Tanaka, M. (1998), *J. Vac. Sci. Technol. B,* 16 (4), 2267-2274

Tavernier, P. R. and D. R. Clarke (2001), *J. Appl. Phys.,* 89 (3), 1527-1536

Thaler, G. T., M. E. Overberg, B. Gila, R. Frazier, C. R. Abernathy, S. J. Pearton, J. S. Lee, S. Y. Lee, Y. D. Park, Z. G. Khim, J. Kim and F. Ren (2002), *Appl. Phys. Lett.,* 80 (21), 3964-3966

Thorne, A., U. Litzen and S. Johansson in *Spectrophysics: Principles and Applications,* Springer Verlag, Berlin, 1999, pp. 207-208.

Tian, C. and C. R. Vidal (1998), *J. Phys. B,* 31 (24), 5369-5381

Toftmann, B., J. Schou, T. N. Hansen and J. G. Lunney (2000), *Phys. Rev. Lett.,* 84 (17), 3998-4001

Toth, Z., B. Hopp, T. Smausz, Z. Kantor, F. Ignacz, T. Szorenyi and Z. Bor (1999), *Appl. Surf. Sci.,* 138-139, 130-134

van de Riet, E., J. C. S. Kools and J. Dieleman (1993), *J. App. Phys.,* 73 (12), 8290

Vispute, R. D., S. Choopun, R. Enck, A. Patel, V. Talyansky, R. P. Sharma, T. Venkatesan, W. L. Sarney, L. Salamanca-Riba, S. N. Andronescu, A. A. Iliadis and K. A. Jones (1999), *J. Electron. Mater.,* 28 (3), 275-286

Von Allmen, M. in *Laser-Beam Interactions with Materials,* Springer-Verlag, Heidelberg, 1980, p. 149.

References

Von Allmen, M., *Laser-Beam Interactions with Materials,* Springer-Verlag, Heidelberg, 1987a.

Von Allmen, M. in *Laser Interactions with Materials,* Springer-Verlag, Berlin, 1987b, pp. 25-30.

Wang, X. Y., D. M. Riffe, Y.-S. Lee and M. C. Downer (1994), *Phys. Rev. B,* 50 (11), 8016-8019

Warn, J. R. W., *Concise Chemical Thermodynamics,* Van Nostrand Reinhold (UK), Wokingham, England, 1985.

Watanabe, H., S. Fujita, S. Maruno, K. Fujita and M. Ichikawa (1997), *Appl. Phys. Lett.,* 71 (8), 1038-1040

Watanabe, H., H. Sugiyama, T. Ichikawa and M. Hasegawa (1996), *Surf. Sci.,* 357-358, 115-118

Willmott, P. R., F. Antoni and M. Dobeli (2000), *J. Appl. Phys.,* 88 (1), 188-195

Wittenberg, L. J. and R. DeWitt (1972), *J. Chem. Phys.,* 56 (9), 4526-4533

Wood, R. F., J. N. Leboeuf, D. B. Geohegan, A. A. Puretzky and K. R. Chen (1998), *Phys. Rev. B,* 58 (3), 1533-1543

Wu, J. D., J. Sun, Z. F. Ying, W. Shi, H. Ling, F. M. Li, Z. Y. Zhou, K. L. Wang and X. M. Ding (2001), *J. Vac. Sci. Technol. A.,* 19 (1), 299-305

Yang, H., H. Al-Brithen, E. Trifan, D. C. Ingram and A. R. Smith (2002), *J. Appl. Phys.,* 91 (3), 1053-1059

Yu, G., G. Wang, H. Ishikawa, M. Umeno, T. Soga, T. Egawa, J. Watanabe and T. Jimbo (1997), *Appl. Phys. Lett.,* 70 (24), 3209-3211

Zajac, M., R. Doradzinski, J. Gosk, J. Szczytko, M. Lefeld-Sosnowska, M. Kaminska, A. Twardowski, M. Palczewska, E. Grzanka and W. Gebicki (2001), *Appl. Phys. Lett.,* 78 (9), 1276-1278

Zalm, P. C. (1984), *J. Vac. Sci. Tech. B,* 2 (2), 151-152

Zel'dovich, Y. B. and Y. P. Raizer in *Physics of Shock Waves and High Temperature Hydrodynamic Phenomena,* Academic Press, New York, Vol.1, 1966,